

**INNOVATIVE TiO₂ BASED NANOMATERIALS FOR PHOTOCATALYTIC CO₂
REDUCTION TO FUELS AND ANTI-FOULING MEMBRANE IN WATER
TREATMENT**

by

Qianyi Zhang

A Dissertation Submitted in
Partial Fulfillment of the
Requirements for the Degree of

Doctor of Philosophy
in Engineering

at

The University of Wisconsin-Milwaukee

May 2015

ABSTRACT

INNOVATIVE TiO₂ BASED NANOMATERIALS FOR PHOTOCATALYTIC CO₂ REDUCTION TO FUELS AND ANTI-FOULING MEMBRANE IN WATER TREATMENT

by

Qianyi Zhang

The University of Wisconsin-Milwaukee, 2015
Under the Supervision of Professor Ying Li

Due to fossil fuel usage, booming industry and other human activities, greenhouse gases associated with global warming and drinking water shortage severely threaten sustainable development of human society. It is emergent and critical to address and solve both of them.

Greenhouse gases will trap heat and cause global warming, carbon dioxide (CO₂) from fossil fuel combustion is the major contribution to greenhouse gas emission. In order to control CO₂ emission, different technologies have been invented. Recently, photoreduce CO₂ using solar energy with photocatalyst catches a lot of attention. Because on the one hand this technology can reduce CO₂ in atmosphere, on the other hand alternative fuel can be produced with solar energy such as CO, methane, methanol, etc.

For the drinking water shortage problem, membrane filtration technology has been proved as one of the most efficient and reliable methods to provide clean drinking water. However, membrane fouling caused by deposition of contaminants on membrane surface

has been recognized as one of the major obstacles inhibiting the application of membrane technologies. Membrane fouling may dramatically shorten the lifetime of membrane module, deteriorate the quality of water produced and increase the operation cost. With the help of the photocatalyst, contaminants in water and on membrane can be degraded under light irradiation. Membrane fouling caused by contaminants can be significantly mitigated.

Among all photocatalysts that have been investigated, TiO_2 is a promising high efficient photocatalyst for both environmental and energy application, due to the low cost, high redox potential and nontoxicity. However, because of the large bandgap, fast hole/electron recombination process and limited visible light absorption, those characters significantly limit the application of TiO_2 . In this study, different TiO_2 modification strategies were carried out to improve the efficiency of TiO_2 photoactivity.

One objective of this study is to demonstrate visible light functional iodine doped titanium oxide (I-TiO_2) for CO_2 photoreduction. I-TiO_2 nanoparticles have been synthesized by hydrothermal method. I-TiO_2 shows photocatalitically responsive to visible light illumination. The structure and properties of I-TiO_2 nanocrystals prepared with different iodine doping levels and/or calcination temperatures were characterized by X-ray diffraction, transmission electron microscopy and diffraction, X-ray photoelectron spectroscopy, and UV–vis diffuse reflectance spectra. The three nominal iodine dopant levels (5, 10, 15 wt.%) and the two lower calcination temperatures (375, 450°C) produced mixture of anatase and brookite nanocrystals, with small fractions of rutile found at 550°C. The anatase phase of TiO_2 increased in volume fraction with increased calcination temperature and iodine levels. A high CO_2 reduction activity was observed for I-TiO_2

catalysts (highest CO yield equivalent to $2.4 \mu\text{mol g}^{-1} \text{h}^{-1}$) under visible light, and they also had much higher CO₂ photoreduction efficiency than undoped TiO₂ under UV–vis irradiation. I–TiO₂ calcined at 375°C has superior activity to those calcined at higher temperatures. Optimal doping levels of iodine were identified under visible and UV–vis irradiations, respectively.

Along with promising nonmetal-doped TiO₂ results, our study also entails a new metal-nonmetal ion co-modified TiO₂ nanoparticles fabricated through a combined hydrothermal and wet-impregnation process. Under UV–vis irradiation, the activity of the co-modified catalyst (Cu–I–TiO₂) was higher than that of the single ion-modified catalysts (Cu–TiO₂ or I–TiO₂). Under visible light irradiation, the addition of Cu to I–TiO₂ did not lead to significant improvements in CO₂ reduction. Methyl chloride (CH₃Cl) was detected as a reaction product when CuCl₂ was used as the precursor in the synthesis, thus suggesting that methyl radicals are reaction intermediates. When CuCl₂ was used as the Cu precursor, a three-fold increase in CO₂ photoreduction activity was observed, as compared to when Cu(NO₃)₂ was used as the Cu precursor. These differences in activities were probably due to enhanced Cu dispersion and the hole-scavenging effects of the Cl ions.

The water treatment with membrane filtration technology will always face membrane fouling. It is one of the major obstacles inhibiting the wide application of membrane technologies for water treatment. Membranes with surface modification of titanium dioxide (TiO₂) nanoparticles or TiO₂ nanowire membranes (Ti–NWM) have demonstrated reduced membrane fouling due to the photocatalytic capability of TiO₂ in degrading foulants on the membrane surface. However, the wide band gap of TiO₂ makes

it only absorb ultraviolet light, which limits its applications under solar irradiation. In this study, our work entailed a novel membrane made of interwoven iron oxide (Fe_2O_3) nanowires and TiO_2 nanowires (FeTi-NWM) has demonstrated superior anti-fouling capability in removing humic acid (HA) from water. Results showed that under simulated solar irradiation the FeTi-NWM achieved nearly complete HA removal during a 2 h short-term test at an initial HA concentration of 200 mg/L, compared with 89% HA removal by Ti-NWM. During a 12 h long-term test, the FeTi-NWM maintained 98% HA removal, while the Ti-NWM showed only 55% removal at the end. Without solar irradiation, the FeTi-NWM was severely contaminated and by contrast, a clean surface was maintained under solar irradiation after the 12 h test and the transmembrane pressure change was minimal. The improved HA removal by FeTi-NWM compared with Ti-NWM and its excellent anti-fouling capability under solar irradiation can be attributed to (1) the enhanced HA absorption by Fe_2O_3 nanowires and (2) the formed $\text{Fe}_2\text{O}_3/\text{TiO}_2$ heterojunctions that increase photo-induced charge transfer and improve visible light activity.

Future work includes further improvement of FeTi-NWM membrane with other materials such as graphene etc. Also design and test multi-stage FeTi-NWM membranes system for real industry application.

© Copyright by Qianyi Zhang, 2015

All Rights Reserved

TABLE OF CONTENTS

ABSTRACT	ii
TABLE OF CONTENTS.....	vii
LIST OF FIGURES	ix
LIST OF TABLES.....	xii
LIST OF ABBREVIATIONS	xiii
ACKNOWLEDGEMENTS.....	xv
Chapter 1 Introduction And Research Objectives.....	1
1.1 Research background.....	1
1.1.1 Impact of greenhouse gas and CO ₂ emission control.....	1
1.1.2 Water treatment with membrane separation technology	3
1.2 Literature review about TiO ₂ properties and its environmental application	5
1.3 TiO ₂ based nanomaterials.....	9
1.4 Comparison between TiO ₂ and other semiconductor materials as photocatalyst	11
1.5 Research of Objectives of Outline of the Dissertation.....	13
Chapter 2 Visible Light Responsive Iodine-Doped TiO ₂ For Photocatalytic Reduction Of CO ₂ To Fuels.....	17
2.1 Research Background	17
2.2 Experimental	20
2.3 Results and Discussion	23
2.3.1 Average nanocrystal structure from XRD analysis.....	23
2.3.2 Individual nanocrystal structure and morphology from TEM analysis	25
2.3.4 Photocatalytic activity for CO ₂ reduction	28
2.4 Summary and Conclusion.....	35
Chapter 3 Copper And Iodine Co-Modified TiO ₂ Nanoparticles For Improved Activity Of CO ₂ Photoreduction With Water Vapor	36
3.1 Research Background	36
3.2 Experimental	39
3.3 Results and Discussion	40
3.3.1 Characteristics of Cu-I-TiO ₂ catalysts.....	40
3.3.2 Photocatalytic ability of Cu-I-TiO ₂ catalysts.....	44
3.3.3 Product selectivity and reaction mechanism	48
3.4 Conclusion.....	52
Chapter 4 Novel Anti-Fouling Fe ₂ O ₃ /TiO ₂ Nanowire Membranes For Humic Acid Removal From Water	54
4.1 Research background.....	54
4.2 Experimental	56
4.2.1 Synthesis of Fe ₂ O ₃ /TiO ₂ nanowire membranes (FeTi-NWM).....	56
4.2.2 Membrane Characterization.....	58
4.2.3 Humic acid removal under different light conditions.....	59
4.2.4 Long-term test of anti-fouling capability	61
4.3 Results and discussion.....	62
4.3.1 Morphological, structural and optical properties of the nanowire membranes.....	62

4.3.2 Humic acid removal under different experimental conditions	65
4.3.3 Long-term anti-fouling test results.....	69
4.3.4 Proposed mechanism of enhanced HA removal by FeTi-NWM	72
4.4 Conclusions	75
Chapter 5 Summary Of Research Work.....	77
5.1 Summary of Research Work.....	77
Chapter 6 Instrumental Analysis	80
Reference.....	84
Curriculum Vitae	92

LIST OF FIGURES

Figure 1.1 2013 Greenhouse Gas Emissions in US by Gas [2]	2
Figure 1.2 World CO ₂ emission from fuel combustion[3].....	2
Figure 1.3 Predicted water scarcity and stress in 2025 [1]	4
Figure 1.4 Crystal structure of TiO ₂ (a. Rutile; b. Anatase; c. Brookite) [32]	8
Figure 1.5 Mechanism of photocatalytic reaction by TiO ₂	9
Figure 1.6 Surface band bending of anatase (a) and rutile (b) [29]	9
Figure 1.7 TiO ₂ nanostructure (a) nanoparticles, (b) nanowires, (c) nanotubes and (d) nanorods	11
Figure 1.8 Band position of different semiconductors.....	13
Figure 2.1 Experimental setup for CO ₂ photoreduction. 1: mass flow controller; 2: water bubbler; 3: photoreactor with a quartz window; 4: two-way valve; 5: long-pass filter; 6: gas chromatograph (GC/TCD-FID); 7: catalyst samples dispersed on glass fiber filter; 8: Xe lamp; 9: sampling port.....	22
Figure 2.2 XRD patterns of I-doped TiO ₂ at different calcination temperatures (a) and I- doped TiO ₂ at different iodine doping level (b) (A: anatase; B: brookite; R: rutile)	24
Figure 2.3 Electron microscopy of 5% I-TiO ₂ -375C sample: (a) TEM image and SAED, (b) HRTEM image with labeled examples of anatase (A) and brookite (B) nanocrystals, and (c) HRTEM lattice spacings and dominant surface facets for A (120) and B (111).....	26
Figure 2.4 UV-Vis diffuse reflectance spectra of TiO ₂ with different iodine doping levels (a) and plots of the square root of the Kubelka-Munk function versus the photon energy (b).....	28

Figure 2.5 Concentration of CO produced from CO ₂ photoreduction under visible light (a) and under UV-vis irradiation (b) using different I-doped TiO ₂ samples.....	30
Figure 2.6 Spectra of the Xe lamp used in this study, with and without the 400 nm long- pass filter, in comparison to the AM 1.5G standard solar spectrum.....	32
Figure 2.7 Time dependence on the ration of O ₂ /(O ₂ +N ₂) during photocatalytic reaction with 5% I-TiO ₂ 375C as photocatalyst	34
Figure 3.1 XRD patterns of TiO ₂ (a), 10I-TiO ₂ (b), 1Cu-TiO ₂ (c), and 1Cu-10I-TiO ₂ (d) samples. (A=anatase; B=brookite).....	41
Figure 3.2 EDX analysis and SEM image of 1Cu-10I-TiO ₂ sample	43
Figure 3.3 UV-vis diffuse reflectance spectra of the Cu/I-TiO ₂ samples displayed in absorbance.....	44
Figure 3.4 CO yield under visible light irradiation (a) and UV/vis irradiation (b).....	45
Figure 3.5 Mechanism of Cu/Iodine co-doped TiO ₂ for CO ₂ reduction	50
Figure 4.1 Procedure of synthesizing Ti-NWM and FeTi-NWM.	57
Figure 4.2 Humic acid removal under solar irradiation by FeTi-NWM with different Fe ₂ O ₃ /TiO ₂ mass ratios.....	57
Figure 4.3 SEM image of the 0.2 μm polystyrene microsphere.	58
Figure 4.4 Humic acid removal using the FeTi-NWM under different flow rates	60
Figure 4.5 Schematic of the water filtration system for HA removal using nanowire membranes under simulated sunlight.....	61
Figure 4.6 SEM images showing the morphology of (a) Ti-NWM, (b) calcined Fe ₂ O ₃ nanowires, (c) FeTi-NWM, (d) cross-section of Ti-NWM, and (e) cross-section of FeTi-NWM. The insets of (a) and (c) show photos of 75 mm diameter Ti-NWM and	

FeTi–NWM, respectively.	63
Figure 4.7 XRD patterns for (a) Ti–NWM, (b) Fe ₂ O ₃ nanowires, and (c) FeTi–NWM, all after 400°C calcination.	64
Figure 4.8 UV-vis spectra for Fe ₂ O ₃ -NW, Ti–NWM and FeTi–NWM.....	65
Figure 4.9 Humic acid removal in the dark, under visible light and solar light conditions using Ti–NWM and FeTi–NWM (a commercial PVDF membrane was also tested as a control).	66
Figure 4.10 Humic acid removal and TOC removal by FeTi-NWM under solar irradiation	68
Figure 4.11 Long-term test for HA removal using FeTi–NWM and Ti–NWM (4 cycles and 3 h in each cycle with fresh 200 mg/L HA introduced at the beginning of each cycle).....	70
Figure 4.12 Photos of two FeTi–NWMs after the long-term test of HA removal, one with solar irradiation and the other without.	71
Figure 4.13 Transmembrane pressure across Ti–NWM and FeTi–NWM during the 10 h test in the dark or under solar irradiation.	72
Figure 4.14 Proposed mechanism for the photocatalytic degradation of humic acid (HA) on FeTi–NWM under UV light (a) and visible light (b), respectively.	75

LIST OF TABLES

Table 1.1 Membrane characterizations by pore size and target species [8].....	5
Table 2.1 Phase content and average crystal size of I-TiO ₂	25
Table 3.1 Phase content and average size of Cu-I-TiO ₂ samples obtained from X-ray diffraction, band gap from optical spectroscopy, and specific surface area from BET analysis (A:anatase; B:brookite).....	42
Table 3.2 Amount of CO ₂ photoreduction products measured at 210 min under visible and UV-vis light irradiation.....	49

LIST OF ABBREVIATIONS

UV	Ultraviolet
DFT	Density functional theory
TTIP	Titanium isopropoxide
BET	Brunauer–Emmett–Teller
XRD	X-ray diffraction
HRTEM	High resolution transmission electron microscopy
SAED	Selected area electron diffraction
XPS	X-ray photoelectron spectroscopy
BE	Binding energy
GC	Gas chromatograph
TCD	Thermal conductivity detector
FID	Flame ionization detector
PDF	Powder diffraction file
SSA	Specific surface areas
NT/Cu	Cu nanoparticles
EDX	Energy-dispersive X-ray spectroscopy
FTIR	Fourier transform infrared spectroscopy
Ti-NWM	Titanium dioxide (TiO ₂) nanowire membrane
FeTi-NWM	Titanium dioxide/iron oxide nanowire membrane
NTA	Nitrilotriacetic acid
PS	Polystyrene microsphere
DRS	UV-vis diffused reflectance spectroscopy

TRPAS	Time-resolved photoacoustic spectroscopy
EPR	Electron paramagnetic resonance

ACKNOWLEDGEMENTS

I would like to express my deep appreciation and gratitude to my advisor, Dr. Ying Li, for the patient guidance and mentorship he provided to me, all the way from when I was first considering applying to the PhD program in the Mechanical Engineering Department, through to completion of this degree. Dr. Li's guidance and support are essential and have made my PhD study a thoughtful and rewarding journey. And this journey will benefit my whole life. I am truly fortunate to have had the opportunity to work with him.

I would also like to thank my committee members, Drs. Junhong Chen, Jin Li, Ben Church and John Reisel for their friendly guidance, thought-provoking suggestions, and the general collegiality that each of them offered to me over the years.

I would like to give my special thanks to Mr. Donald Robertson for his assistance in TEM and HRTEM analyses and Dr. H. A. Owen for technical support with SEM analyses.

I am also grateful to my colleagues and friends. Particularly, I thank Dr. Cunyu Zhao, and Dr. Guiying Rao for their friendship and support over the years.

Finally, I want to express my greatest appreciation for my mom and my families, they are the engine-power for me to pursue my PhD degree.

Chapter 1 Introduction And Research Objectives

1.1 Research background

1.1.1 Impact of greenhouse gas and CO₂ emission control

Due to the demand of energy and the growth of population, the generation of greenhouse gas has tremendously increased. They have seriously threatened the health of environment and sustainable development of human society.

The major greenhouse gases directly emitted by human activities include CO₂, CH₄, N₂O, and several other fluorine-containing halogenated substance. Those greenhouse gases trap heat and make the planet warmer, which will result in severe weather condition and ecosystem collapse. Based on the report of intergovernmental panel on climate change (IPCC)[1], just in 2005, the record number of tropical storms and hurricanes caused more than 1000 deaths and more than US\$ 100 billion in damage along Atlantic and gulf coasts of United States. The unique systems of Arctic region and warm water coral reefs are also undergoing rapid changes in response to observed warming in ways that are potentially irreversible[1].

Figure 1.1 illustrates the relative contribution of the direct greenhouse gases to total U.S. emissions in 2013. The primary greenhouse gas emitted by human activities in the United States was CO₂, representing approximately 82.44 percent of total greenhouse gas emissions. The largest source of CO₂, and of overall greenhouse gas emissions, was fossil fuel combustion[2]. World wide, CO₂ emission from fuel combustion has been increasing at an average rate of 2% a year to a 1997 annual global output of around 23 billion tons of CO₂ (**Figure 1.2**). Roughly half of these emissions remain in the atmosphere [3].

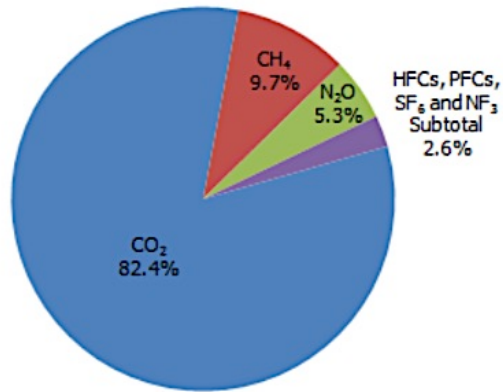


Figure 1.1 2013 Greenhouse Gas Emissions in US by Gas [2]

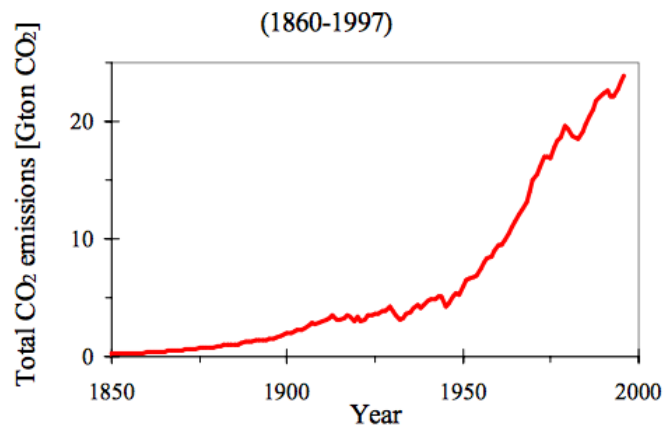


Figure 1.2 World CO₂ emission from fuel combustion[3]

In order to reduce the emissions of CO₂, one popular approach is using more efficient energy conversion and utilization technologies. However, those technologies alone may not be able to help the atmosphere to achieve CO₂ stabilization. Therefore, efforts are also assigned to the capture and sequestration of CO₂ that comes out of fossil fuel combustion process. There are three main capture methods for CO₂: Pre-combustion methods (fuel decarbonization); Combustion in O₂/CO₂ atmospheres (oxygen-fuel firing); Post-combustion capture methods [3].

1) **Fuel decarbonization:** Prior to combustion, CO₂ was removed from gas stream rather than after combustion, this is because the higher concentration, lower volumetric flow rate and higher pressure before combustion make this process easier. However, this method requires a syngas manufacturing plant and a CO₂ removal plant, which will significantly increase the capital cost of application.

2) **Oxygen-fuel firing:** Replacing air with pure or enriched oxygen during the combustion process. A separate CO₂ removal process is avoided/or minimized with this approach, the produced CO₂ is ready for sequestration directly. Oxygen-fuel firing can produce 75% less fuel gas than air-fueled combustion process. The drawback for this technology is that producing pure oxygen will consume large amounts of energy.

3) **Post combustion process:** Several different methods to remove CO₂ from a gas stream exist, including absorption by use of amines, different adsorption techniques, use of membranes, etc. These CO₂ capture processes have significant energy requirements, which reduce the power generation plant's efficiency by up to 40% (relative), and net power output up to 40%[3].

As mentioned above, all current CO₂ capture technologies are energy consuming and non-economy. Therefore, more energy friendly and cheap CO₂ capture methods are desired for the future.

1.1.2 Water treatment with membrane separation technology

Same as the situation of greenhouse gases, drinking water shortage is becoming a global problem due to the rapid industrialization and exploding population. One-third of

the world's population currently live in countries with insufficient freshwater supply (**Figure 1.3**) and two-thirds of the world population will face water scarcity by 2025 [4, 5].



Figure 1.3 Predicted water scarcity and stress in 2025 [1]

The growing global demand of clean water forces scientists to explore new technologies for drinking water production [6]. Among all types of technologies, membrane filtration is one of the most effective approaches to provide high quality and quantity drinking water. The global demand for membrane modules was estimated at approximately 15.6 billion USD in 2012 and the market is expected to grow around 8% annually [7]. Membrane filtration is favored over other technologies for water treatment, such as disinfection, distillation, or media filtration because, in principle, they require no chemical additives, thermal inputs, or require regeneration of spent media [8]. Among all kinds of different membranes, pressure-driven membrane processes remain the most widely used membrane technologies for water treatment applications.

Pressure-driven membranes are classified according to characteristic pore size or their intended application (**Table 1.1**) [8-11]. Currently, membrane technology is commercially available for suspended solids, protozoa, and bacteria removal (microfiltration, MF), for virus and colloid removal (ultrafiltration, UF), for hardness, heavy metals, and dissolved organic matter removal (nanofiltration, NF), and for desalination, water reuse, and ultrapure water production (reverse osmosis, RO)[8]. However, membrane fouling caused by deposition of contaminants on the membrane surface has been recognized as one of the major obstacles inhibiting the application of membrane technologies [12, 13]. Membrane fouling may dramatically shorten the lifetime of membrane module, deteriorate the quality of water produced and increase the operation cost.

Table 1.1 Membrane characterizations by pore size and target species [8]

Pore type (size range/nm)	Membrane type (pore size/nm)	Species ^c	Dimensions ^c /nm
Macropores (>50)	Microfiltration ^a (50–500)	Yeasts & fungi	1000–10 000
		Bacteria	300–10 000
		Oil emulsions	100–10 000
Mesopores (2–50)	Ultrafiltration ^a (2–50)	Colloidal solids	100–1000
		Viruses	30–300
		Proteins/polysaccharides	3–10
		Humics/nucleic acids	<3
		Common antibiotics	0.6–1.2
Micropores (0.2–2)	Nanofiltration ^a (≤2)	Organic antibiotics	0.3–0.8
	Reverse osmosis ^b (0.3–0.6)	Inorganic ions	0.2–0.4
	Forward osmosis ^b (0.3–0.6)	Water	0.2

1.2 Literature review about TiO₂ properties and its environmental application

Researchers all over the world have been working on various approaches to try to solve the problem of greenhouse gases and drinking water shortage. Photocatalytic reaction with semiconductor is a promising way to address this problem, which catches a lot of attention. Extensive studies about photoinduced reaction have been carried out.

Among all those semiconductors that have been studied, Titanium dioxide (TiO_2) is considered to be as an ideal material for photocatalytic reaction due to its low cost, strong redox ability and environment friendly.

In 1964, Kota et al.[14] used TiO_2 suspension to treat tetralin, which was followed by McIntock et al.[15] who oxidized ethylene and propylene by TiO_2 . However, in 1972, Fujishima and Honda et al.[16] discovered the photocatalytic water splitting process with TiO_2 electrodes for first time. This discovery opens a new era for photocatalysis research. This well-known chemical phenomenon involves the photoirradiation of a TiO_2 single crystal electrode immersed in an aqueous electrolyte solution induced the evolution of oxygen from the TiO_2 electrode and the evolution of hydrogen from a platinum counter electrode when an anodic bias was applied to the TiO_2 working electrode. Following on the steps of Fujishima and Honda, the photocatalytic properties of TiO_2 have been further studied to convert solar energy into chemical energy to obtain useful chemicals such as hydrogen[17] and hydrocarbons[18, 19], and to remove pollutants and bacteria on wall surfaces[20] or in the water and air [21-24].

TiO_2 belongs to the family of transition metal oxides along with ZnO, ZrO. There are three TiO_2 crystals that commonly exist in nature: anatase[25, 26] (tetragonal), brookite (orthorhombic), and rutile (tetragonal)[27, 28]. Besides these polymorphs, there are two more high pressure forms that have been found from the rutile phase. They are TiO_2 (II) with a PbO_2 structure and TiO_2 (H) with a hollandite structure[29]. Here, this study will focus on the three major crystal phases of TiO_2 :

The Rutile Crystal phase of TiO_2 : Rutile TiO_2 has a tetragonal structure (**Figure 1.4 (a)**) and contains 6 atoms per unit cell. The TiO_6 octahedron is noticed slightly

distorted[29]. The rutile phase is stable at most temperatures and pressures up to 60 kbar. With increasing the size of anatase and brookite crystal, the crystal phase transfer process to rutile will happen, because the rutile phase is more stable than anatase for particle sizes greater than 14 nm. Once the rutile phase forms, it grows much faster than the anatase[29]. For the photocatalyst activity, the rutile phase is generally very poor.

The anatase crystal phase of TiO_2 : Same as the rutile phase, anatase has a tetragonal structure. But compared with the rutile, the distortion of the TiO_6 octahedron is slightly larger in anatase (**Figure 1.4(b)**). Muscat et al.[30] found that the anatase phase is more stable than the rutile at 0 K, but the energy difference between these two phases is small (~2 to 10 kJ/mol). The anatase structure is preferred over other polymorphs for solar cell application due to its higher electro mobility[31]. The higher photoreactivity of anatase is brought by the slightly higher Fermi level, lower capacity to adsorb oxygen and higher degree of hydroxylation[29]. The reactivity of (001) face is greater than that of (101) face in the anatase crystal structure based on the work of Wang et al[26].

The brookite crystal phase of TiO_2 : Brookite of TiO_2 has a different structure compared with the former two crystal phases (anatase and rutile). Brookite belongs to the orthorhombic crystal system (**Figure 1.4(c)**). Its unit cell is composed of 8 formula units of TiO_2 and is formed by edge sharing TiO_6 octahedra. Brookite is more complicated and has a larger cell volume. The properties of brookite were still barely investigated.

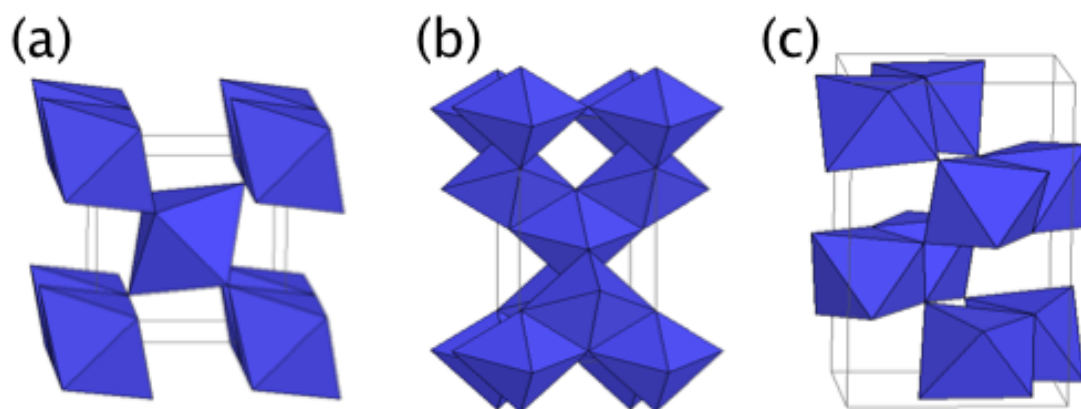


Figure 1.4 Crystal structure of TiO_2 (a. Rutile; b. Anatase; c. Brookite) [32]

TiO_2 is a large band semiconductor, with band gaps of 3.2, 3.02 and 2.96 eV for anatase, rutile and brookite, respectively[29]. The 2p orbitals of oxygen and 3d orbitals of titanium compose the valence band of TiO_2 ; meanwhile, the conduction band is only the 3d orbitals of titanium. When TiO_2 is under UV irradiation, electrons in the valence band are excited to the conduction band leaving behind holes (h^+), as shown in **Figure 1.5**. The excited electrons (e^-) in the conduction band are now in a purely 3d state and because of dissimilar parity, the transition probability of e^- to the valence band decreases, leading to a reduction in the probability of e^-/h^+ recombination. As mentioned earlier, the anatase TiO_2 is considered the active photocatalytic compound compared with all other crystal phases of TiO_2 . Anatase has spontaneous band bending (**Figure 1.6**) [29] in a deeper region with a steeper potential compared with the rutile, thus surface hole trapping dominates because spatial charge separation is achieved by the transfer of photogenerated holes towards the surface of the particle via the strong upward band bending. However, in the rutile phase, the bulk recombination of electrons and holes occurs, so only holes very close to the surface are trapped and transferred to the surface[29].

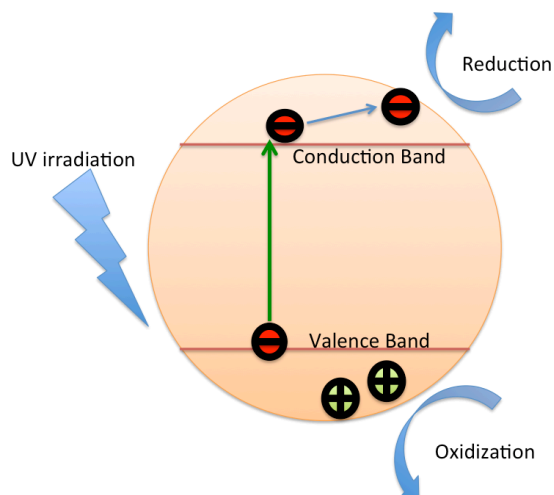


Figure 1.5 Mechanism of photocatalytic reaction by TiO_2

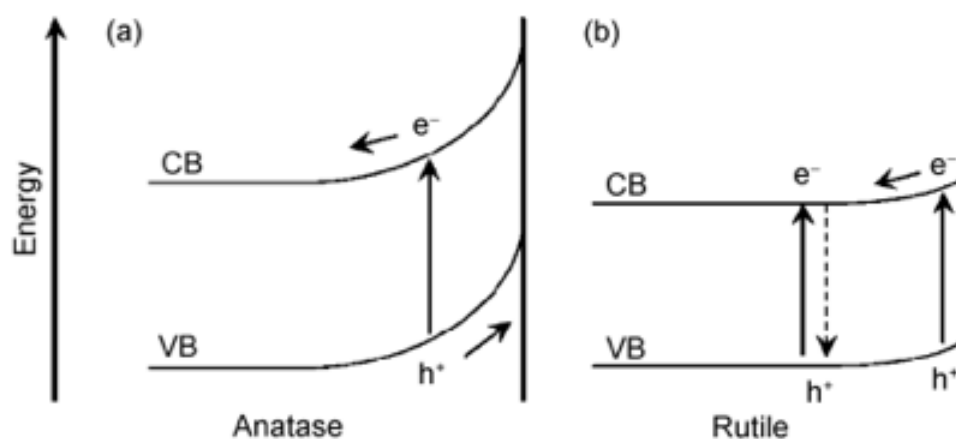


Figure 1.6 Surface band bending of anatase (a) and rutile (b) [29]

1.3 TiO_2 based nanomaterials

Due to the large surface area of nano-structure, nano-size TiO_2 usually is much more efficient for photoinduced reaction than bulk TiO_2 . When the crystal size of a semiconductor is below around 10 nm, the quantum mechanics will significantly affect the properties of materials. Many researches reported when the material reached the nano scale, the absorption edge blue shifts happened which caused the redox potentials

increase for semiconductors[28, 33, 34]. In other words, the photoactivity of nano-size semiconductors would be improved. There are two common commercialized TiO₂ nano-materials for sale right now, the P25 and the P20. The P20 is the 100% anatase. The difference between P20 and P25 is the TiO₂ nanoparticles with 80% anatase and 20% rutile in P25.

Except the TiO₂ nanoparticles, many other morphologies of nano scale TiO₂ were also synthesized in the lab (**Figure 1.7**) such as nanotubes[35-37], nanosphere[38, 39], and nanowires[6, 40, 41]. Liquid phase associated reaction is one of the most popular and convenient methods to synthesize nano-scale TiO₂ materials. This method provides the possibility to control the stoichiometry and form complex shapes. Guo et al.[42] reported using a simple and reliable hydrothermal method to prepare super hydrophobic TiO₂ surface on fluorine-doped tin oxide (FTO) coated glass substrates. The surface shows a novel cactus-like cluster structure composed of TiO₂ rods. After being modified with stearic acid, the as-prepared surface shows a remarkable super hydrophobicity with a water contact angle as high as 160° and a sliding angle smaller than 5°. Meanwhile, with the help of the hydrothermal method, Hu et al.[43] was able to synthesize the highly entangled TiO₂ nanowire on Ti substrates at 180 °C with utilizing various organic solvents to oxidize Ti. The freestanding TiO₂ nanowire membranes with millimeter level thickness can be cleaved from Ti substrates or directly prepared from thin Ti foils.

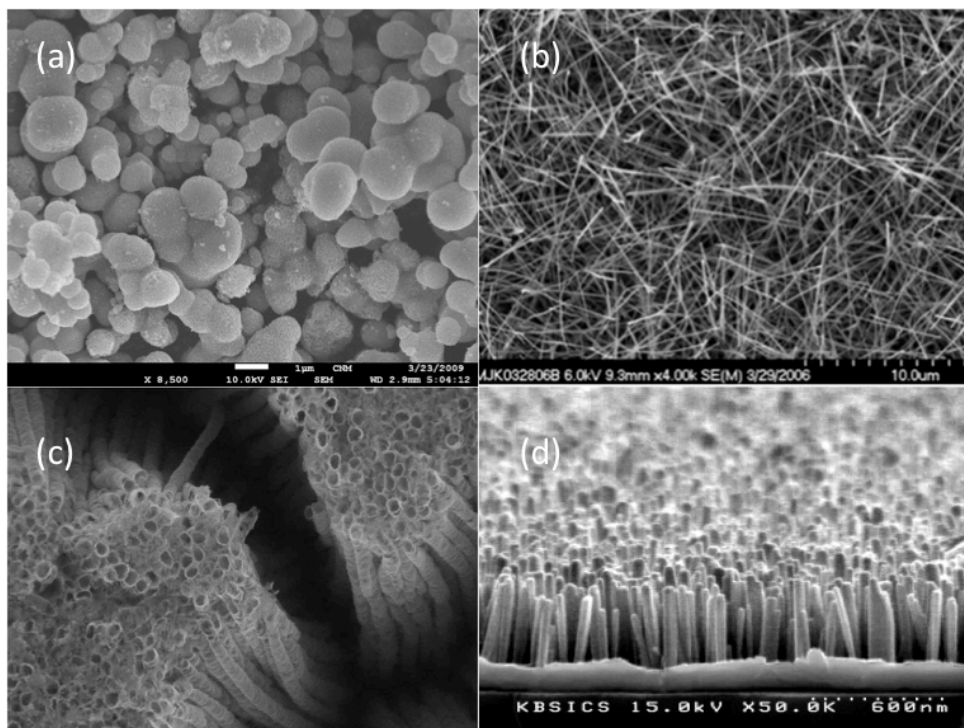


Figure 1.7 TiO₂ nanostructure (a) nanoparticles[44], (b) nanowires, (c) nanotubes[45] and (d) nanorods[46]

1.4 Comparison between TiO₂ and other semiconductor materials as photocatalyst

The redox potential is the primary criteria for an efficient semiconductor. The energy level at the bottom of the conduction band determines the reducing ability of photoelectrons, meanwhile the energy level at the top of the valence band determines the oxidize ability of semiconductors.

The summary of lower edge of the conduction band, the upper edge of the valence band and the band gap of some semiconductors was plot in **Figure 1.8**. The internal energy was represented by ordinate. The internal energy (band gap) is usually larger than the free energy of an electron and hole pair because the e^-/h^+ pairs will have a huge entropy arising due to a large number of translational states accessible to the charge carriers in the conduction and valence bands[29]. In order to induce the photocatalytic

reaction, besides the suitable band gap energy for the reaction, the ideal semiconductor should also be cheap, easily be produced and used, high efficient, harmless for the environment and human health. Most of the reported photocatalyst shows many drawbacks. For example, the ZnO is unstable in aqueous environment because it will continuously dissolved in water to yield Zn(OH)_2 on the surface of ZnO, which will inactivate the catalyst over time[47, 48]. GaAs[49] is not stable in the liquid media too and does not even mention the toxicity of it. Among those semiconductors, TiO_2 is the most promising semiconductor for photocatalyst. As mentioned earlier, TiO_2 is low-cost, easy to be produced, with high chemical and physical stability and nontoxic, and high redox ability. Due to these reasons, many novel applications and photocatalytic reactions have been investigated by researchers. For example, Fakeeha et al.[50] and Arenas et al.[51] reported to use TiO_2 to reform CH_4 . But TiO_2 still has some drawbacks, which significantly limit its wide application. First, TiO_2 has large bandgap around 3.2 eV for anatase. This means pure TiO_2 can be only activated under UV irradiation. If the TiO_2 is used for solar application, that means there is only 5% of total energy that can be used in sunlight[7]; Second, the fast recombination process of photoinduced e^- and h^+ brings very low efficiency for TiO_2 in some application. To overcome those problems, several approaches including dye sensitization, ion doping or coating have been studied extensively. The following chapters will cover some of those approaches that be investigated in this study aimed at improving the performance of TiO_2 .

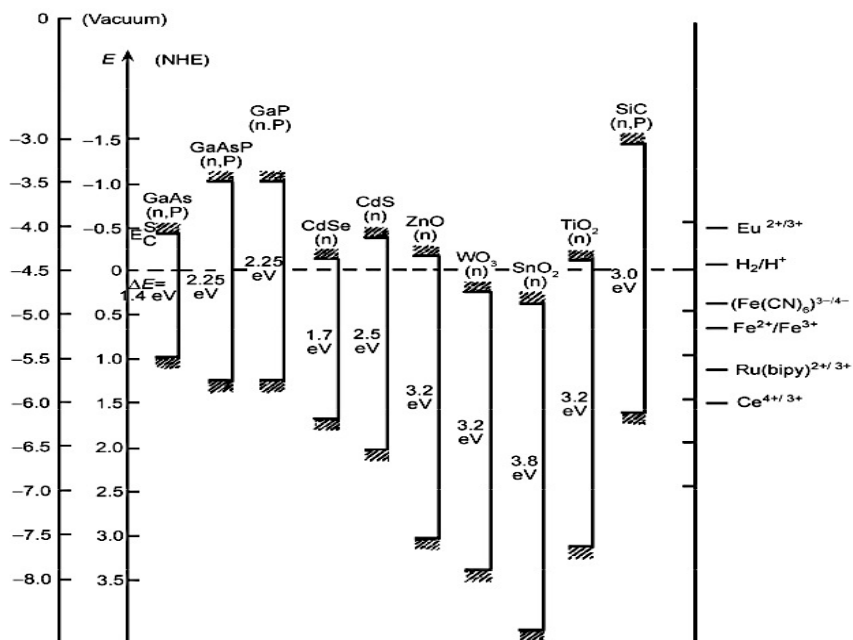


Figure 1.8 Band position of different semiconductors [29]

1.5 Research of Objectives of Outline of the Dissertation

The overall objective of this research is to synthesize and modify TiO_2 nanostructure, in order to improve TiO_2 performance on photoreduction and photooxidation for environmental application. To achieve the research objective, the work is divided into three major tasks, which are summarized below.

Task 1. Visible light responsive iodine-doped TiO_2 for photocatalytic reduction of CO_2 to fuels (Chapter 2)

The objective of this task is to investigate the modification of TiO_2 by non-metal ion doping. The CO_2 photoreduction efficiency under visible light irradiation with iodine doped TiO_2 was tested. Five subtasks were carried out:

- ❖ TiO₂ nanoparticle with iodine doping was synthesized by the hydrothermal method.
- ❖ Three different calcination temperatures (375, 450 and 550 ° C) were used to treat TiO₂ samples; meanwhile three different iodine loading levels were also applied.
- ❖ The resulting TiO₂ nanoparticles were characterized by using various techniques, such as X-ray diffraction spectrum (XRD), X-ray photoelectron spectroscopy (XPS), scanning electron microscopy (SEM), Brunauer-Emmett-Teller (BET) surface area analysis, UV-vis diffuse reflectance spectra, transmission electron microscopy (TEM), and high-resolution transmission electron microscopy (HRTEM).
- ❖ CO₂ photoreduction test was carried out in a sealed stainless-steel reactor. The reduction production CO was tested by gas chromatography equipped with thermal conductivity detector (TCD) and flame ionization detector (FID).
- ❖ Effects of calcination temperature and iodine doping level on TiO₂ crystal structure and CO₂ photoreduction efficiency were carefully analyzed.

Task 2. Copper and iodine co-modified TiO₂ nanoparticles for improved activity of CO₂ photoreduction with water vapor (Chapter 3)

The objective of this task is to investigate the effect of metal-nonmetal co-modification on TiO₂. Cu-Iodine co-modified TiO₂ was synthesized and tested for its CO₂ photoreduction efficiency. Four subtasks were carried out:

- ❖ Cu-Iodine co-modified TiO_2 nanoparticle was fabricated by the hydrothermal method followed with the wet impregnation method.
- ❖ All the samples were characterized by using various technologies, such as X-ray diffraction spectrum (XRD), X-ray photoelectron spectroscopy (XPS), scanning electron microscopy (SEM) equipped with energy dispersive X-ray (EDX) spectroscopy, Brunauer-Emmett-Teller (BET) surface area analysis, and UV-vis diffuse reflectance spectra.
- ❖ Three different Cu precursors (CuCl_2 , $\text{Cu}(\text{NO}_3)_2$, and $\text{Cu}(\text{NO}_3)_2+\text{KCl}$) were used in order to investigate the effect of Cu valence on TiO_2 surface modification. TiO_2 samples that with different Cu loading levels and initial 10% iodine doping were tested under both visible and UV-vis irradiation for CO_2 photoreduction.
- ❖ The possible mechanism for TiO_2 efficiency promoting by Cu-Iodine co-modification was discussed.

Task 3. Novel $\text{Fe}_2\text{O}_3/\text{TiO}_2$ hybrid nanowire membrane for concurrent filtration and removal of multi-pollutants in water with anti-fouling feature (Chapter 4)

The objective of this task is to fabricate and characterize novel $\text{Fe}_2\text{O}_3/\text{TiO}_2$ nanowire membrane, which is used for multiple pollutants degradation in water. Four subtasks were carried out:

- ❖ Novel $\text{Fe}_2\text{O}_3/\text{TiO}_2$ hybrid nanowire membrane was fabricated with the vacuum filtration method.

- ❖ Various technologies were used to characterize the hybrid nanowire membrane, such as X-ray diffraction spectrum (XRD), scanning electron microscopy (SEM) and UV-vis diffuse reflectance spectra.
- ❖ Humic acid was chosen as model pollutants, which represents one of the major causes for membrane fouling. The filtration efficiency, degradation efficiency and long term anti-fouling ability with hybrid nanowire membrane were carefully investigated.
- ❖ The effect of different composite ratios of Fe_2O_3 to TiO_2 on degradation efficiency of nanowire membrane was discussed at the same time.

Chapter 2 Visible Light Responsive Iodine-Doped TiO₂ For Photocatalytic Reduction Of CO₂ To Fuels

2.1 Research Background

Due to the urgency of the CO₂ emission control, recently using photoreduction feature of photocatalyst to convert CO₂ into fuels by sunlight catches extensive attentions. Not only this technology mitigates the CO₂ emissions but also produce energy-bearing compounds such as CO, methane, and methanol[31, 52, 53] that can be subsequently converted to liquid transportation fuels. Compared with other materials that have been reported for CO₂ photoreduction applications include ZrO₂[54], MgO[55], NiO/InTaO₄[56], Ga₂O₃, photosensitized complexes[57], TiO₂ based catalysts[6, 54, 58] are promising candidates because of TiO₂ has strong redox ability, low cost, stability, and environmental friendly. However, as we mentioned in chapter 1, one challenge for the application of TiO₂ is the fast recombination of photo-induced holes (h⁺) and electrons (e⁻). Another challenge is the requirement of ultraviolet (UV) light excitation due to the wide band gap of TiO₂ (3.2 eV for anatase and 3.0 eV for rutile). As a result, the efficiency of CO₂ conversion to fuels is generally low. Modification of TiO₂ with metal (e.g. Pt, Pd, Ag, and Cu) particles or clusters has been reported to inhibit charge recombination possibly because the metals serve as electron traps[59, 60]. Thus, the increased CO₂ photoreduction efficiency was observed for metal modified TiO₂. Tseng et al.[61] synthesized Cu/TiO₂ catalysts by a sol-gel method and found the rate of CO₂ photoreduction to methanol was much higher than those without copper loading. Li et

al.[62] reported markedly increased CO₂ photo-conversion efficiency by Cu/TiO₂ catalyst dispersed on mesoporous silica and selective CH₄ production due to Cu loading. However, too high a concentration of metal dopant may form recombination centers that lead to a reduced photocatalytic efficiency. Optimal metal concentrations have been reported for modified TiO₂ (e.g. with Ag or Cu) for both photooxidation and photoreduction applications. While metal modifications on TiO₂ have apparent enhancement in charge separation, they have limited contribution to extend the photo-response to visible light region. Sasirekha et al.[63] observed that Ru doped TiO₂ has almost the same absorption spectra as the undoped TiO₂. Dholam and Patel[64] reported that Cr and Fe doped TiO₂ prepared by a sol-gel method had a very limited effect on inducing a red-shift in TiO₂ absorption spectra compared to those prepared by a magnetron sputtering method.

On the other hand, it has been widely reported that doping TiO₂ with nonmetals (e.g. C, N, S, F, etc.) has resulted in more significant band gap narrowing compared to metal doping, leading to high photocatalytic efficiency under visible light irradiation. Wu et al.[65] reported that the band gaps of N doped and N-B co-doped TiO₂ were 2.16 eV and 2.13 eV, respectively, much smaller than that of pure TiO₂ (3.18 eV for anatase). Pelaez et al.[66] synthesized N-F co-doped TiO₂ that exhibited high surface area, low degree of agglomeration and high activity in degradation of microcystin under visible light. Recently, less studied iodine has been doped into TiO₂, and improved visible light activity towards the decomposition of organic compounds has been reported. The structural and electronic properties of I-doped TiO₂ were investigated based on density

functional theory (DFT) calculations, and the results indicated that substitutional iodine contributes to a much more efficient and stable photocatalyst than pristine TiO₂. In comparison to other non-metal dopants (N[51], C, B[56], S[67]), iodine doping may result in superior photocatalytic activity due to the following reasons. First, unlike other nonmetal dopants that substitute lattice oxygen, iodine was reported to be able to replace lattice titanium due to the close ionic radii of I⁵⁺ and Ti⁴⁺. The substitution of Ti⁴⁺ with I⁵⁺ causes charge imbalance and results in the generation of Ti³⁺ surface states that may trap the photoinduced electrons and forestall charge recombination. In addition, first principle calculations suggest that iodine atoms prefer to be doped near the TiO₂ surface due to the strong I–O repulsion[68], and thus, the surface doped I⁵⁺ will not only trap electrons but also facilitate electron transfer to the surface adsorbed species. Finally, it is suggested that the continuous states consisting of 5p and/or 5s orbitals of I⁵⁺ and O 2p orbitals of the valence band are favorable for efficient trapping of holes at the I-induced states in the TiO₂ particle (not on the surface), which causes a decrease in the oxidation power. For CO₂ photoreduction, one of the challenges is the reoxidation of the CO₂ reduction products by h⁺ or OH[•] radicals. Hence, the impaired oxidation power of I-doped TiO₂ may result in an increased CO₂ photoreduction rate.

In this study, I-doped TiO₂ photocatalysts were synthesized via a hydrothermal method and were evaluated for the first time for CO₂ reduction under UV and visible light irradiation. The effects of iodine doping levels and calcination temperature on the catalytic activity were also investigated, a topic that has been scarcely discussed in the literature for I-doped TiO₂. The structural and compositional properties of the I-TiO₂

nanomaterials were analyzed and correlated with their photocatalytic reduction performance. This is the first time photocatalytic CO₂ reduction by nonmetal doped TiO₂ without any other co-catalysts have been reported. Therefore, the findings are an important step toward the discovery of cost-effective catalysts for CO₂ reduction to solar fuels.

2.2 Experimental

The method for synthesis of I-doped TiO₂ was modified from that reported by Tojo et al.[69]. The preparation started by dissolving 3 ml of titanium isopropoxide (TTIP) (Acros Organic, >98%) in 3 ml of anhydrous isopropanol (Acros Organic, >99.5%). The mixture was then added dropwise into a solution of iodic acid (HIO₃) (Alfa Aesar, >99.5%) with continuous stirring for 2 h. After the reaction, the resultant white mixture was transferred to a Teflon-lined vessel for hydrothermal treatment at 100 °C for 12 h. The resultant yellow particles were filtrated and washed with copious amount of de-ionized water until pH 7 followed by drying in an oven at 80 °C for 1 h. The samples were finally calcined in air for 2 h at different temperatures (375, 450, or 550 °C). Different iodine doping levels were prepared by varying the quantity of HIO₃ added (0.06–0.18 g). The samples are denoted in the way of “x% I-TiO₂-yC”, where x is the nominal weight percentage of iodine in the sample (calculated from the bulk solution) and y is the calcination temperature. For example, 5% I-TiO₂-375C represents 5 wt.% (nominal) I-doped TiO₂ calcined at 375 ° C. For comparison, undoped TiO₂ was prepared following the same procedure without adding HIO₃. All samples were grinded and sieved by a 45 μm stainless steel sieve before characterization and photoreduction experiments.

Brunauer–Emmett–Teller (BET) surface area analysis by N₂ adsorption was performed using a Quantachrome NOVA 1200 gas sorption analyzer (Boynton Beach, FL). The crystal structures of the prepared catalysts were identified by X-ray diffraction (XRD) (Scin-tag XDS 2000) using Cu K α irradiation at 45 kV and a diffracted beam monochromator operated at 40 mA in the 2 θ range from 20° to 70° at a scan rate of 1°/min. The crystal size of different crystal phases was calculated by the Scherrer equation.

The lattice structure of individual nanocrystals was visualized by phase-contrast high resolution transmission electron microscopy (HRTEM) carried out with 300 keV electrons in a Hitachi H9000NAR instrument with 0.18 nm point and 0.11 nm lattice resolution. Two-dimensional Fourier transforms were calculated and used to measure lattice spacing and interplanar angles. Amplitude contrast TEM images were used to obtain direct information about the nanocrystal sizes. Selected area electron diffraction (SAED) provided information that is analogous to XRD, but from nanocrystals supported on an electron-transparent amorphous carbon film and selected within a ~450 nm diameter aperture. The UV-vis diffuse reflectance spectra were obtained by a UV-vis spectrometer (Ocean Optics) using BaSO₄ as the background.

X-ray photoelectron spectroscopy (XPS) analysis was carried out on a Perkin-Elmer PHI 5100 ESCA system with an Al K α X-ray source ($h\nu = 1253.6$ eV) and pass energy of 35.75 eV operating at a pressure of 8×10^{-10} Torr. The observed spectra were corrected with the C1s binding energy (BE) value of 284.6 eV.

The schematic of the photocatalytic reaction system is illustrated in **Figure 2.1**. Compressed CO₂ (99.99%, Praxair) regulated by a mass flow controller was passed

through a water bubbler to generate CO₂ and H₂O vapor mixture (H₂O, v/v% ≈ 2.3%). The gas mixture was then purged through a cylindrical photoreactor (V=58 cm³) with stainless steel walls and a quartz window. A fixed amount of powder catalyst (200 mg) was dispersed on a glass-fiber filter and placed at the bottom of the reactor. After purging for 1.5 h, the gas valves on both sides of the reactor were closed to seal the reactor. A 450 W Xe lamp (Oriel) was used as the light source and a long-pass filter was applied to cut off the short wavelengths that are less than 400 nm if only visible light is needed. A spectroradiometer (International Light Technologies ILT950) was used to obtain the spectral intensity of the Xe lamp with and without the filter. During the illumination period, the gaseous samples in the reactor were taken by a gastight syringe (Hamilton, #1750, 500 μl) every 30 min and manually injected to a gas chromatograph (GC, Agilent 7890A) equipped with both a thermal conductivity detector (TCD) and flame ionization detector (FID).

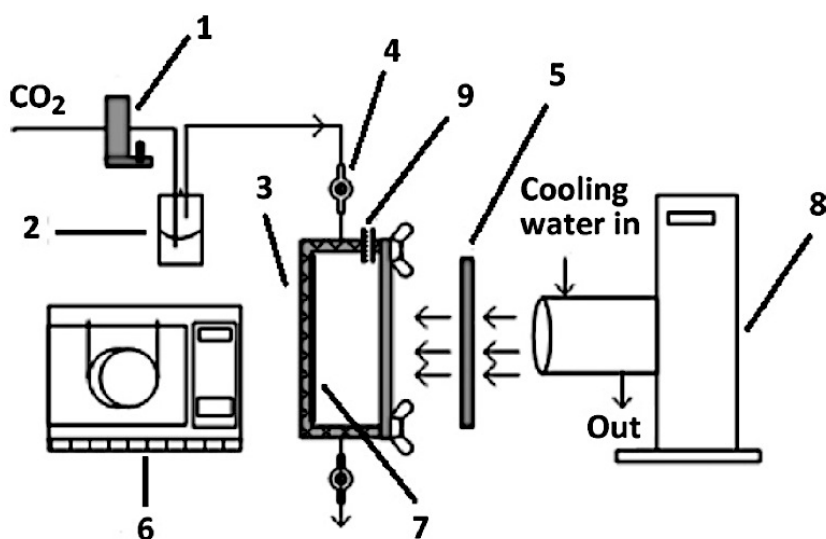


Figure 2.1 Experimental setup for CO₂ photoreduction. 1: mass flow controller; 2: water bubbler; 3: photoreactor with a quartz window; 4: two-way valve; 5: long-pass filter; 6: gas chromatograph (GC/TCD-FID); 7: catalyst samples dispersed on glass fiber filter; 8: Xe lamp; 9: sampling port.

2.3 Results and Discussion

2.3.1 Average nanocrystal structure from XRD analysis

Figure 2.2 shows the XRD patterns of TiO_2 samples doped with different concentrations of iodine calcined at 375°C and 5% I- TiO_2 calcined at different temperatures. The calculated values of phase content and crystal size are listed in **Table 2.1**. The undoped and I-doped TiO_2 mainly consist of two phases, anatase and brookite. As the calcination temperature increased from 375 to 450°C , the anatase phase content increased and the brookite phase decreased; when the calcination temperature increased to 550°C , the brookite content further decreased with the appearance of a small percentage of rutile. The phase transition between metastable anatase and brookite is not well studied in the literature; however, the result in this study seems to be in agreement with some of the literature that upon calcination brookite transforms to rutile via anatase. In other words, brookite first transforms to anatase and then anatase transforms to rutile. In contrast to undoped nanocrystal TiO_2 whose anatase-to-rutile transformation temperature is around 700°C , the lower temperature (450 – 550°C) of transformation to rutile in this study was possibly due to the dopant-induced instability of TiO_2 caused by lattice distortion and bond weakening, even at a low dopant concentration (for 5% I- TiO_2). When the calcination temperature was kept the same at 375°C , increasing the iodine concentration only slightly decreased the brookite content by a few percent.

In terms of crystal size, it is clear from **Table 2.1** that with increasing calcination temperature the average crystal size increases for both anatase and brookite crystals (by a factor of $\sim 2.45 \pm 0.10$ at 550°C compared with 375°C). At the same calcination

temperature of 375°C, the undoped TiO₂ has the largest crystal size for anatase (8.8 nm), and the crystal size decreases (to 7.5, 5.5, and 5.8 nm) as the nominal iodine doping level

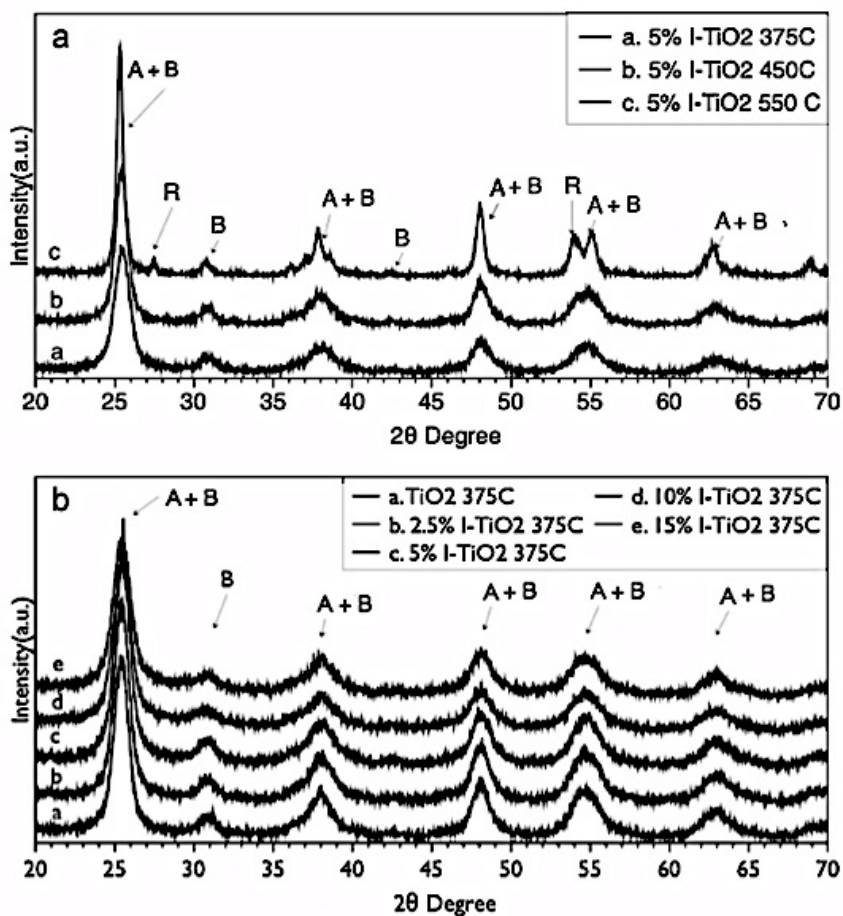


Figure 2.2 XRD patterns of I-doped TiO₂ at different calcination temperatures (a) and I-doped TiO₂ at different iodine doping level (b) (A: anatase; B: brookite; R: rutile)

increases in increments of 5% (from 0% to 15%). This result agrees with the literature that dopants can favor the formation of smaller particles. For example, Zhou et al.[70] reported the particle sizes of N doped and N-I co-doped TiO₂ are smaller than pure TiO₂. Su et al.[71] found that I-doped TiO₂ has much smaller crystallite size (7.7 nm, anatase) than undoped TiO₂ (23.7 nm, anatase) and suggested that the repulsion among adsorbed

iodine species inhibits crystal growth. An interesting finding in our study is that the brookite crystallite size of I-doped TiO₂ is slightly larger than that of undoped one (**Table 2.1**), indicating that iodine has opposite effect on the growth rate of anatase and brookite nanocrystals under otherwise identical hydrothermal conditions. The lack of literature on doping of brookite TiO₂ warrants further investigation in this interesting phenomenon.

Table 2.1 Phase content and average crystal size of I-TiO₂

Sample	Phase Content (%)			Crystal Size (nm)		Band Gap (eV)	BET (m ² /g)
	A	B	R	A	B		
TiO ₂ -375C	66	34	0	8.8	4.7	3.13	122.9
5% I-TiO ₂ -375C	66	34	0	7.5	5.4	3.05	137.4
5% I-TiO ₂ -450C	71	29	0	8.4	10.1	-	99.4
5% I-TiO ₂ -550C	76	19	5	19.1	12.7	-	43.1
10% I-TiO ₂ -375C	70	30	0	5.5	6.3	3.00	137.6
15% I-TiO ₂ -375C	72	28	0	5.8	5.5	3.02	137.6

2.3.2 Individual nanocrystal structure and morphology from TEM analysis

Figure 2.3 shows amplitude-contrast transmission electron microscopy (TEM in (a)) and phase-contrast high-resolution TEM images (HRTEM in (b) and (c)) of the 5% I-TiO₂-375C sample. Both types of images show agglomerates of TiO₂ nanocrystals. The crystallite size is in the range of 6 – 9 nm, which is in good agreement with the average size calculated from the Scherrer equation. Similarly, selected area electron diffraction experiments (SAED inset in (a)) recorded from agglomerates within a selecting aperture of 450 nm confirm the phase determination of XRD and demonstrates that the anatase and brookite phases of I-TiO₂ occur in close proximity. The HRTEM images show lattice fringes within individual nanocrystals. Analysis of the lattice spacings and interplanar angles finds that each nanocrystal has a well-defined phase and the lattice appears cleanly and bulk-terminated at the surface. The nanocrystal morphology is defined by low-energy

facets that are conjoined by curved surfaces composed of closely spaced terraces and steps. For example, the HRTEM image in **Fig. 2.3(c)** shows clear one-dimensional lattice

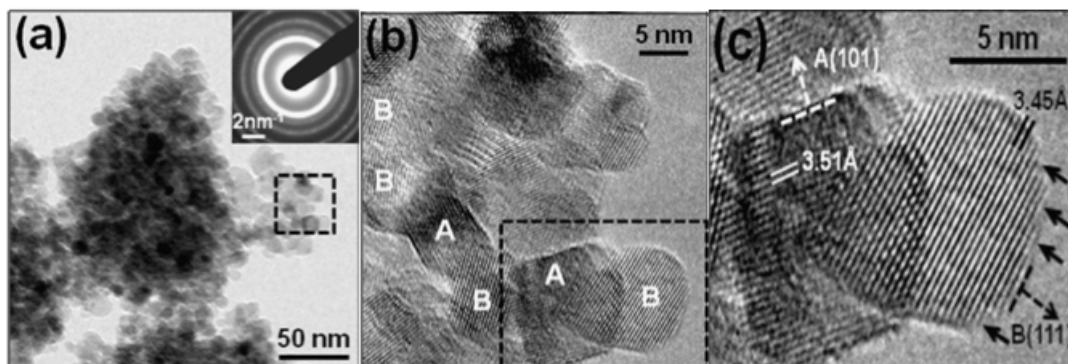


Figure 2.3 Electron microscopy of 5% I-TiO₂-375C sample: (a) TEM image and SAED, (b) HRTEM image with labeled examples of anatase (A) and brookite (B) nanocrystals, and (c) HRTEM lattice spacings and dominant surface facets for A (120) and B (111)

fringes of TiO₂ (lattice spacing = 0.345 nm) which is very close to the brookite TiO₂ (111) bulk lattice spacing of 0.346 nm, according to powder diffraction file (PDF) No. 29-1360. Since all of the anatase spacings overlap with brookite very closely, it is only possible to uniquely determine the termination facets of the brookite nanocrystals. These consistently yield the (111) type of crystal plane as dominant facet for the brookite TiO₂ nanocrystals. The second type of termination plane occurs for interplanar distance of ~0.351 nm [56] which is the (101) plane of anatase or the (120) plane of brookite. It is unlikely that brookite nanocrystals would have two very different dominant facets under the same growth and calcination condition. Hence, it is possible to conclude, by elimination, that the second type of facets belong to anatase (101) type planes. These morphology changes are the subject of on-going work and are beyond the scope of this initial work to evaluate the efficacy of I-doped TiO₂ as an effective material for CO₂ photoreduction.

2.3.3 UV-vis diffuse reflectance spectroscopy and BET specific surface area analysis

The UV–vis diffuse reflectance spectra of undoped TiO₂ and I-doped TiO₂ samples are shown in **Figure 2.4 (a)**. The absorption edge of undoped TiO₂ is around 400 nm and is extended to the visible light region for I-doped TiO₂ with an iodine concentration from 2.5 to 15%, which matches the yellow color of the I-doped TiO₂. **Figure 2.4(b)** illustrates the plots for obtaining the band gap values that are also listed in Table 1. The undoped TiO₂ has a band gap of 3.13 eV, while the band gaps of I-TiO₂ slightly decrease with iodine doping and level off at around 3.00 eV when the nominal iodine concentration is greater than 10%.

The BET specific surface areas (SSA) of the various I-TiO₂ catalysts are listed in **Table 2.1**. The SSA for undoped TiO₂ is 122.9 m²/g, which is much higher than that of commercially available P25 (~50 m²/g). With iodine doping in TiO₂, the SSA slightly increases as the crystal size slightly decreases in average, and all the I-TiO₂ samples calcined at the same temperature (375°C) have similar SSA (~137 m²/g) since their average crystal sizes are very close to each other, as seen in **Table 2.1**. Increasing the calcination temperature of 5% I-TiO₂ to 450 and 550°C dramatically reduces the SSA to 99.4 and 43.1 m²/g respectively, which corresponds well to the increase in crystal size.

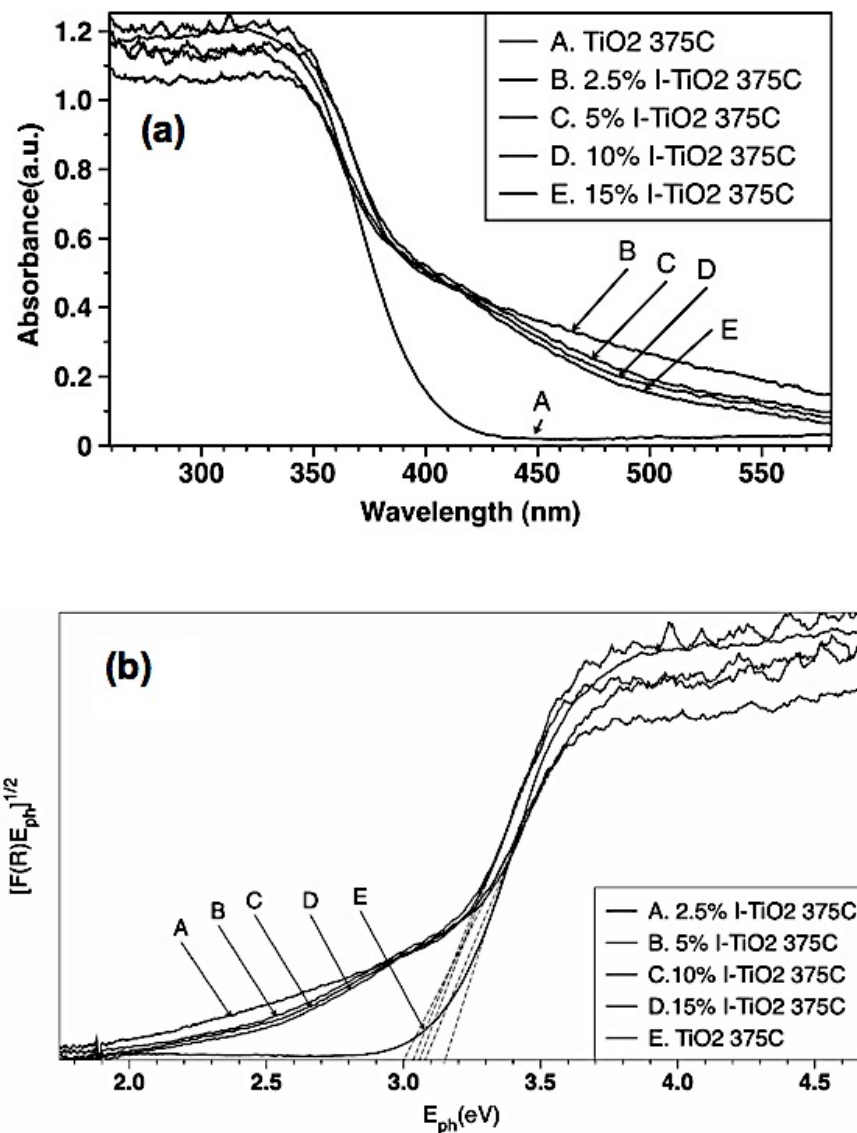


Figure 2.4 UV-Vis diffuse reflectance spectra of TiO₂ with different iodine doping levels (a) and plots of the square root of the Kubelka-Munk function versus the photon energy (b).

2.3.4 Photocatalytic activity for CO₂ reduction

CO was identified as the main CO₂ reduction product using undoped and I-doped TiO₂, while our previous study showed that CH₄ was produced in addition to CO when the TiO₂ surface was loaded with Cu species. The following reactions may express the pathways of CO₂ photoreduction to CO and water oxidation to O₂:

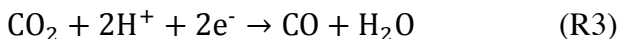
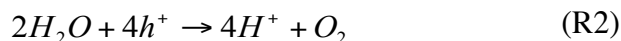


Figure 2.5 shows the concentration of CO produced in the reactor (in ppm) as a function of illumination time under visible ($\lambda > 400$ nm) and UV-vis irradiation ($\lambda > 250$ nm), respectively. Undoped TiO_2 had no activity under visible light (results not shown in **Figure 2.5 a**). All I-doped TiO_2 showed visible light activity for CO_2 photoreduction to CO and the concentration of CO increased almost linearly with illumination time (**Figure 2.5 a**). With the same iodine concentration (5%), I- TiO_2 calcined at 375°C had the highest activity; increased calcination temperatures (450°C and 550°C) lowered the CO_2 photoreduction rate. This is likely due to the significant increase of the crystal size and decrease in surface area with increasing calcination temperature (**Table 2.1**). For I- TiO_2 with the same calcination temperature (375°C), activity of CO_2 photoreduction follows the order of $10\% > 15\% > 5\%$ in terms of iodine doping concentration (**Figure 2.5 a**). The band gap analysis (**Table 2.1**) show that 10% and 15% I- TiO_2 samples have very close band gap energies (3.00 eV and 3.02 eV, respectively) and surface iodine concentrations (2.3 at.% and 2.5 at.%, respectively), suggesting that the 15% I- TiO_2 sample may not be superior to 10% I- TiO_2 . Furthermore, too high a dopant concentration may form charge recombination centers and/or shield the surface of TiO_2 from light irradiation, both of which reduce the photocatalytic activity. These may explain why 10% corresponds to the optimal iodine concentration under visible light irradiation. Similar

findings on the optimal dopant concentration have been reported for metal-doped TiO_2 , while optimal doping concentrations of nonmetals have been much less discussed possibly because they are more difficult to control. This is the first study that has reported an optimal doping level for I-doped TiO_2 .

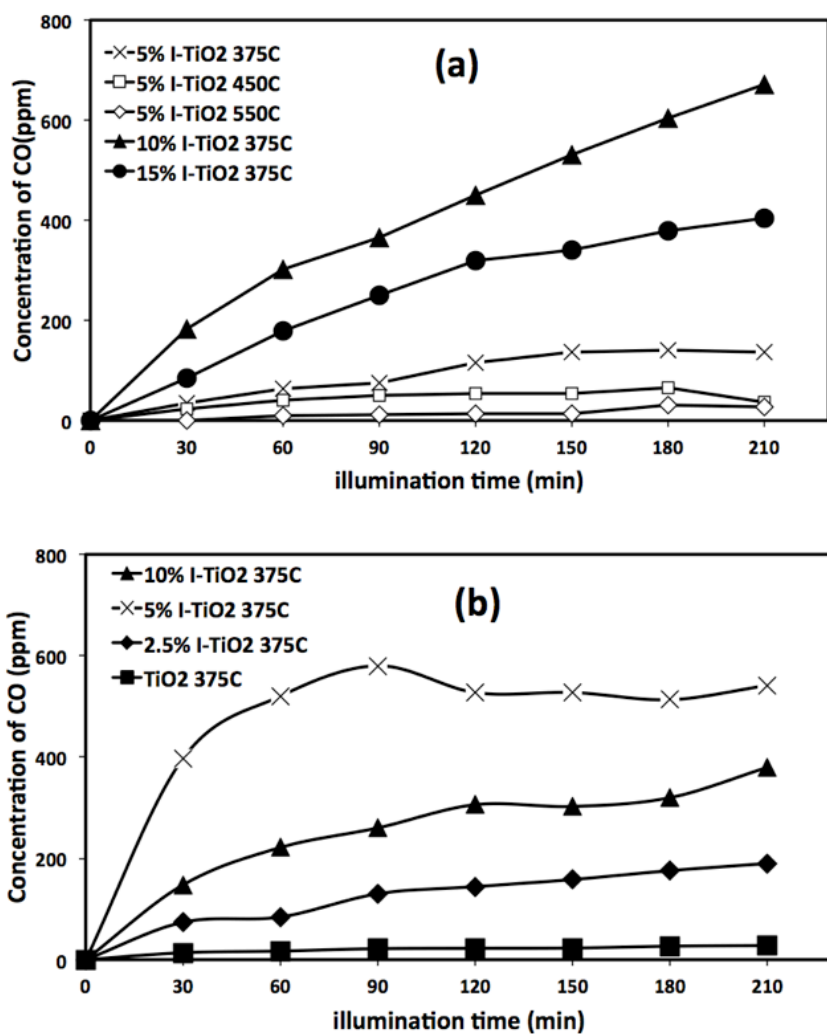


Figure 2.5 Concentration of CO produced from CO_2 photoreduction under visible light (a) and under UV-vis irradiation (b) using different I-doped TiO_2 samples.

The concentration of CO reached 670 ppm at 210 min for the sample of 10% I- TiO_2 -375C under visible light (**Figure 2.5 a**), resulting in a product yield equivalent to 2.4

$\mu\text{mol g}^{-1}\text{h}^{-1}$. There have been very few studies on the CO_2 photoreduction under visible light irradiation. This research, for the first time in the literature, reports photocatalytic CO_2 reduction by nonmetal-doped TiO_2 without any other co-catalysts. Grimes and his co-workers[72] synthesized N-doped TiO_2 nanotube arrays sputtered with Cu nanoparticles (NT/Cu) for CO_2 photoreduction under sunlight and they reported that the activity in visible light region is only 3% of that under the whole solar spectrum (the rates of CO , CH_4 , and other HCs production are equivalent to 0.11, 0.13, and $0.05 \mu\text{mol g}^{-1}\text{h}^{-1}$, respectively; the total production rate is about $0.3 \mu\text{mol g}^{-1}\text{h}^{-1}$ under visible light irradiation of the solar spectrum with an intensity of 78.5 mW/cm^2). Ozcan et al.[73] studied dye-sensitized and Pt modified TiO_2 for CO_2 photoreduction and reported a CH_4 production rate of $0.2 \mu\text{mol g}^{-1}\text{h}^{-1}$ using a 75 W daylight lamp as the visible light source. **Figure 2.6** shows the spectra of the 450 W Xe lamp used in this work, with or without the 400 nm long-pass filter, in comparison with the AM 1.5 G standard solar spectrum. The integrated light intensity of the Xe lamp was 428 mW/cm^2 (full spectrum) and 233 mW/cm^2 for the visible region (400–750 nm). While the visible light intensity in our study was approximately four times higher than those used by Grimes and co-workers and Ozcan et al.[72, 73], our CO_2 photoreduction rate under visible light ($2.4 \mu\text{mol g}^{-1}\text{h}^{-1}$) is approximately eight times higher than that reported by Grimes and co-workers and twelve times higher than that reported by Ozcan et al. Although the photoactivity may not be a linear function of light intensity, and the product selectivities were different in the three studies, the I- TiO_2 photocatalyst developed in this work is a very attractive and promising candidate for larger scale CO_2 photoreduction under sunlight. This catalyst is

highly responsive to visible light and its synthesis requires only low-cost materials and simple manufacturing process steps.

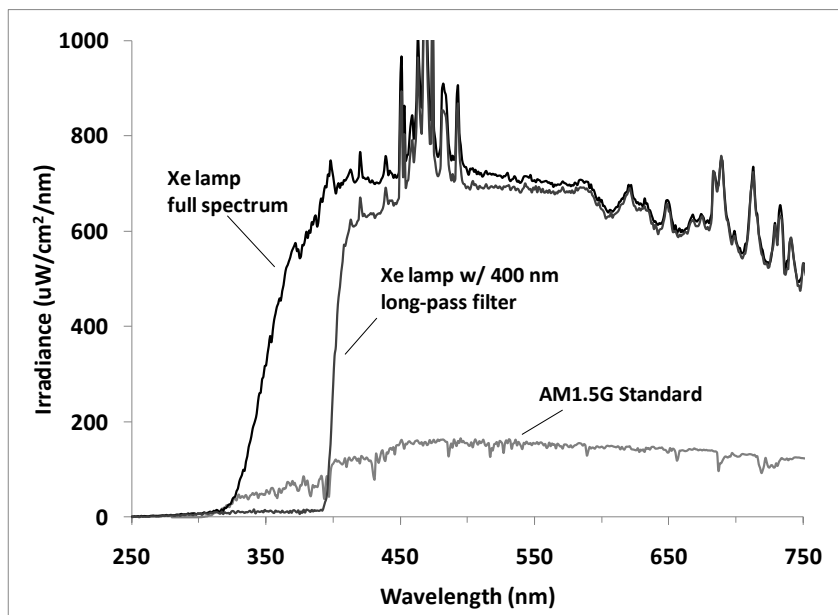


Figure 2.6 Spectra of the Xe lamp used in this study, with and without the 400 nm long-pass filter, in comparison to the AM 1.5 G standard solar spectrum.

Figure 2.5 (b) shows the CO₂ photoreduction activity of the catalysts under UV-vis irradiation. CO₂ photoreduction to CO was observed for undoped TiO₂ calcined at 375°C, confirming that undoped TiO₂ can only be activated by UV irradiation. However, the CO production rate is very low for the pure TiO₂, especially when compared with the I-doped TiO₂ calcined at the same temperature. The enhanced activity of I-doped TiO₂ under UV-vis irradiation is likely due to the combinational effects of slightly increased surface area, increased visible light absorption, and improved charge separation due to the iodine doping. Among the three I-doped TiO₂ (2.5%, 5%, and 10%), 5% I-TiO₂ exhibited the highest activity followed by 10% I-TiO₂, and the CO production for 5% I-TiO₂ reached

nearly 600 ppm in 90 min and leveled off thereafter. The 15% I-TiO₂ was not tested under UV-vis irradiation as its activity was inferior to 10% I-TiO₂ under visible light irradiation.

It is interesting to find that the optimal iodine concentrations in TiO₂ are different under visible light (10%) and UV-vis (5%) irradiations, respectively. Furthermore, the highest CO production rate under visible light irradiation (670 ppm at 210 min for 10% I-TiO₂-375C) is even higher than that under UV-vis irradiation (600 ppm at 90 min for 5% I-TiO₂-375C). In addition, the activity of 10% I-TiO₂-375C under visible light irradiation is higher than that under UV-vis irradiation, but the trend is opposite for 5% I-TiO₂-375C. These results indicate that materials designed for high activity under visible light may not be necessarily optimized for UV applications. Similar findings have been reported that N- or S-doped TiO₂ has superior photooxidation activity to that of undoped TiO₂ under visible light irradiation but has similar or even lower photocatalytic activity in the UV region.

To verify the half reaction of O₂ production from H₂O oxidation, the concentration of O₂ was monitored in a separate test using 5% I-TiO₂-375C as the catalyst under UV-vis irradiation. There were background O₂ and N₂ (a few hundred ppm) detected in the reactor, possibly because the reactor was not vacuumed before purging it with the CO₂-H₂O mixture. In addition, the GC peaks for O₂ and N₂ were close to each other and overlapped to a certain degree. Hence, the change of volumetric ratio of O₂/(O₂+N₂) in the batch reactor would be a better indicator for O₂ production during the photocatalytic

reaction. As shown in **Figure 2.7**, the $O_2/(O_2+N_2)$ ratio slightly decreased in the first 30 min and then increased with the irradiation time at an almost linear rate, implying O_2 production from H_2O dissociation according to R2. The increasing CO concentration under light irradiation (**Figure 2.5**) together with the increasing $O_2/(O_2+N_2)$ ratio (**Figure 2.7**) provide sound evidence of photocatalytic reaction of CO_2 with H_2O to form CO and O_2 .

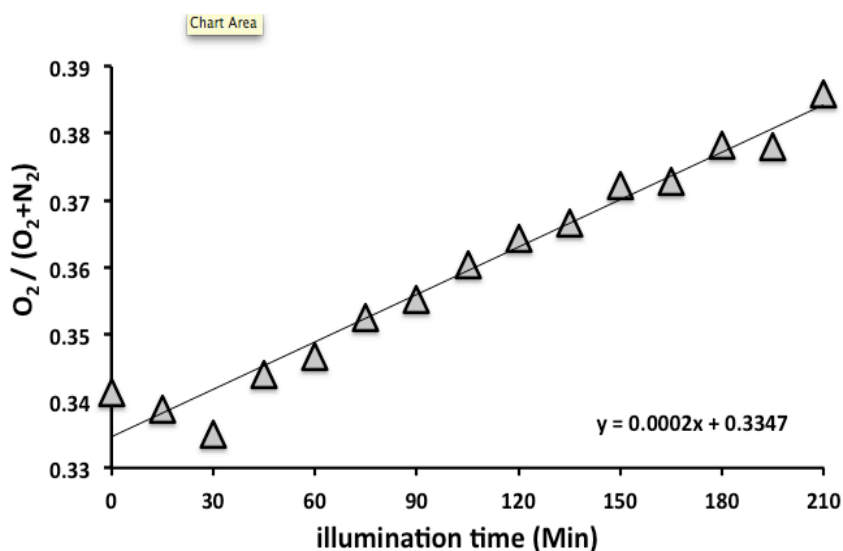


Figure 2.7 Time dependence on the ration of $O_2/(O_2+N_2)$ during photocatalytic reaction with 5% I-TiO₂ 375C as photocatalyst

The possibility of H_2 production due to photocatalytic H_2O reduction was also tested by switching the GC carrier gas from helium to nitrogen to enhance the sensitivity for H_2 . However, under identical experimental conditions using the 5% I-TiO₂-375C, no H_2 was detected during a three hour UV-vis illumination. H_2O reduction to produce H_2 , which competes with CO_2 reduction for electrons, is feasible based on the thermochemical data but experimental results from this study and from the literature suggest that the yield of

H₂ is trace, if any, as compared with those of the CO₂ reduction products, and is prominent only in the presence of noble metals (e.g. Ru, Pt).

2.4 Summary and Conclusion

I-doped TiO₂ photocatalysts with different iodine doping levels and calcination temperatures were prepared and were tested for the activity of photocatalytic CO₂ reduction with H₂O. The iodine dopant extended the absorption spectra of TiO₂ to the visible light region and facilitated charge separation. Significant enhancement of CO₂ photoreduction to CO was observed for I-doped TiO₂ compared with undoped TiO₂ under both visible and UV-vis irradiations. The high activity of CO₂ reduction under visible light compared to the literature data makes I-doped TiO₂ a potentially cost-effective photocatalyst. Lower calcination temperature (375 C°) resulted in smaller particle size and higher catalytic activity. 10% I-doping level demonstrated the highest CO₂ photoreduction rate under visible light, while 5% I-doping level performed best under UV-vis irradiation. Too high an iodine doping level may result in recombination centers and thus lower the photocatalytic activity. Further work is needed to determine if the nanocrystal morphology changes as a function of doping level and annealing conditions, especially for the preparations that show superior photocatalytic activity.

Chapter 3 Copper And Iodine Co-Modified TiO₂ Nanoparticles For Improved Activity Of CO₂ Photoreduction With Water Vapor

3.1 Research Background

Among many different TiO₂ surface modification approaches, the metal doping have been approved can be used to increase the activity of TiO₂. Loading metal nanoparticles onto TiO₂ leads to a redistribution of charges and formation of a Schottky barrier. Electrons migrate from the TiO₂ to the metal, and charge recombination can be suppressed[18]. The incorporation of transition metal ions (e.g., Cu²⁺, Cu⁺, Fe³⁺, etc.) can also lead to the formation of electron trapping sites and promote charge transfer from TiO₂ to metal ions, thus resulting in the enhanced photoreaction of surface adsorbed species. For example, Xu et al.[74] suggested that the Cu (identified as Cu⁺) species that were deposited on TiO₂, forming Ti–O–Cu surface bonds, served as acceptors of electrons that were transferred from the TiO₂ conduction band. While metal modifications of TiO₂ lead to apparent enhancements in charge separation, their effects in altering the optical properties of TiO₂ are limited for most catalysts that are prepared using wet-chemistry methods [58, 59, 62]. An ion implantation method results in more effective doping of metal ions in the TiO₂ lattice, and hence extends the TiO₂ absorption spectrum to the visible light range[75]. However, excess doping of metal ions into the TiO₂ lattice can result in the formation of electron–hole recombination centers[52, 76].

Also as being introduced in Chapter 2. Doping of nonmetal ions (e.g., N, S, C, F, etc.) into the TiO₂ lattice has also been widely reported to modify the nanostructure and

optical properties. These dopants create intra-band-gap states close to the conduction or valence band edges that induce visible light absorption. Unlike metal ions, nonmetal ions are less likely to form recombination centers, and thus are more effective in enhancing visible light activity[76]. The less studied iodine-doped TiO_2 has been explored, and some advantages of the iodine dopant over other nonmetal dopants have been reported[28, 69, 71]. First, substitution of a titanium atom with iodine leads to generation of Ti^{3+} that may trap photoinduced electrons and inhibit charge recombination[7]. Second, iodine atoms prefer to be doped near the TiO_2 surface due to the strong I-O repulsion, and act as surface trapping centers for electrons[41, 68]. Hence, iodine doping not only leads to a red-shift in the TiO_2 light absorption spectrum, but also enhances charge separation[77].

In last chapter, our previous research[77] tested the activity of iodine-doped TiO_2 for CO_2 photoreduction. I- TiO_2 demonstrated significant enhancements in CO_2 photoreduction to CO as compared to undoped TiO_2 under both visible light and UV-vis illumination. Interestingly, for iodine doping higher than a certain level (i.e., nominal 10 wt%), the activity of I- TiO_2 under UV-vis illumination was not superior to that seen under visible light. The formation of recombination centers at high doping levels may account for this phenomenon, but further investigation is needed to better understand the mechanism. On the other hand, one of our previous studies also showed high CO_2 photoreduction activity using a Cu/ TiO_2 catalyst dispersed on a mesoporous silica support[62]. Given that either metal modification or nonmetal doping can improve the photocatalytic activity of TiO_2 , a new composite catalyst was fabricated in this work by

incorporating both Cu and I species into TiO₂. Our hypothesis was that co-modification of TiO₂ with Cu and I would maintain the charge balance and avoid formation of recombination centers, and thus the catalyst could perform more effectively under UV-vis illumination while maintaining a high activity under visible light.

There have been literature reports that suggest that co-doping of metal and nonmetal species on TiO₂ leads to enhanced photocatalytic activity as compared with single ion-doped TiO₂[78]. Examples include co-doping of Cu and S on TiO₂ for improved methyl orange degradation under visible light [78], Fe and N co-doped TiO₂ for narrowed band gap and enhanced photoactivity toward degradation of diphenylamine [79], and Zr and I co-doped TiO₂ for enhanced methyl orange degradation as compared to I/TiO₂ because of a smaller crystal size and higher surface area[80]. Unfortunately, most of those literature publications focused on the applications of photocatalytic oxidation of organic compounds; metal and nonmetal co-modified TiO₂ for photocatalytic CO₂ reduction has been reported only once in the literature. Varghese et al.[81] synthesized N-doped TiO₂ nanotube arrays sputtered with Pt or Cu nanoparticles as a co-catalyst and tested the catalytic activity for CO₂ reduction with water under sunlight. The product yields under visible light irradiation contributed to only 3% of that under the entire solar spectrum, implying a limited rate for visible light utilization[81]. The raw materials used in the work of Varghese et al.[81] were expensive and the fabrication process was relatively complicated. In this work, we used a much simpler method and cheaper raw materials to synthesize Cu and I co-modified TiO₂ nanoparticles. The catalytic activities for the photocatalytic reduction of CO₂ with water vapor under visible and UV-visible

illumination are compared, and new insights regarding the reaction mechanism are proposed in this study.

3.2 Experimental

Copper chloride dehydrate ($\text{CuCl}_2 \cdot 2\text{H}_2\text{O}$, >99%, Acros Organics), iodic acid (HIO_3 , >99.5%, Alfa Aesar), and titanium isopropoxide (TTIP, >99.5%, Acros Organics) were used as the precursors for Cu, I, and TiO_2 , respectively. A two-step process modified from the literature [62] was used to prepare Cu and I co-modified TiO_2 (Cu-I- TiO_2). The first step was to synthesize I-doped TiO_2 through a hydrothermal method reported in our previous study [62, 82]. Briefly, a mixture of TTIP and isopropanol was first added dropwise into a HIO_3 solution under continuous stirring for 2 h, and the resultant mixture was transferred to a Teflon-lined vessel for hydrothermal treatment at 100°C for 12 h. After that, the particles were filtered and washed with copious amounts of deionized water until pH 7. Finally, the I- TiO_2 powders were obtained by drying at 80°C for 1 h and calcination in air for 2 h at 375°C . The nominal iodine concentration and calcination temperature were kept at 10 wt% and 375°C , respectively, because these parameters corresponded to an optimum activity under visible light, as reported in our previous work [77]. The second step in the synthesis process was to incorporate Cu into I- TiO_2 through an incipient wet impregnation process. Typically, 500 mg of the I- TiO_2 sample was mixed in a 20 ml CuCl_2 solution for 1 h, and then the mixture was dried in a vacuum oven at 80°C for 12 h and calcined at 300°C for 1 h. The nominal Cu concentration varied from 0.1 to 1 wt%, a range that corresponded to optimum catalytic activities reported in many studies for Cu-loaded TiO_2 [62, 83]. The samples are denoted

by “ $x\text{Cu}-y\text{I}-\text{TiO}_2$ ”, where x and y are the nominal weight percentages of Cu and I, respectively. For comparison, pure TiO_2 , $\text{Cu}-\text{TiO}_2$, and $\text{I}-\text{TiO}_2$ were also prepared using the same procedure. In addition, to investigate the potential effect of the Cu precursor (i.e., to compare with CuCl_2), additional samples using different Cu precursor solutions (1) $\text{Cu}(\text{NO}_3)_2$ and (2) $\text{Cu}(\text{NO}_3)_2 + \text{KCl}$ with ($\text{Cu}:\text{Cl} = 1:2$) were also prepared using the same procedure. All of the samples were grinded to powders and sieved by a $45\ \mu\text{m}$ stainless steel sieve before the characterization and photoactivity tests.

The characterization part is as same as Chapter 2. Various technology have been used, such as X-ray diffraction (XRD), Brunauer-Emmett-Teller (BET) surface area analyses, scanning electron microscope (SEM) system equipped with energy-dispersive X-ray (EDX) spectroscopy, and UV-vis reflectance spectra. The CO_2 photoreduction activity test also followed with the same procedure as Chapter 2.

3.3 Results and Discussion

3.3.1 Characteristics of Cu-I-TiO₂ catalysts

Figure 3.1 shows the X-ray diffraction (XRD) patterns of pure TiO_2 , $10\text{I}-\text{TiO}_2$, $1\text{Cu}-\text{TiO}_2$, and $1\text{Cu}-10\text{I}-\text{TiO}_2$. For all samples, the characteristic peaks at $2\theta=25.2^\circ$ and $2\theta=30.8^\circ$ indicate the (101) plane of anatase (JCPDS 21-1272) and (121) plane of brookite (JCPDS 29-1360) TiO_2 . No characteristic peak of the rutile phase ($2\theta=27.4^\circ$) was detected. The XRD pattern did not show any copper or iodine phase. Calculated values of the crystal phase contents and crystal sizes appear in Table 3.1. The pure TiO_2 consisted of 70% anatase and 30% brookite, with a crystal size of 8.9 nm for anatase and 4.8 nm for brookite. The BET surface area of TiO_2 was relatively high ($117.3\ \text{m}^2/\text{g}$) as compared

to commercial P25 TiO₂ (~50 m²/g), likely due to its smaller primary particle size (less than 10 nm) as compared to that of P25 (~20 nm). Doping (10I-TiO₂) did not appear to change the phase content, but significantly reduced the crystal size of anatase to 5.6 nm. The smaller crystal size due to lattice doping that was detected in this work agrees with those reported in the literature[71, 77, 84]. Accordingly, the surface area of 10I-TiO₂ (128.2 m²/g) was higher than that of pure TiO₂. The incorporation of Cu (i.e., 1Cu-TiO₂) slightly reduced the anatase content and increased the anatase crystal size, and, consequently, its surface area decreased to 95.3 m²/g. This trend agrees with the result reported by Slamet et al.[85] that Cu-loaded TiO₂ had a smaller surface area as compared to bare TiO₂. This also implies that through the wet impregnation process, Cu species are deposited on the surface of TiO₂ rather than in the lattice. The combination of both Cu and I modification

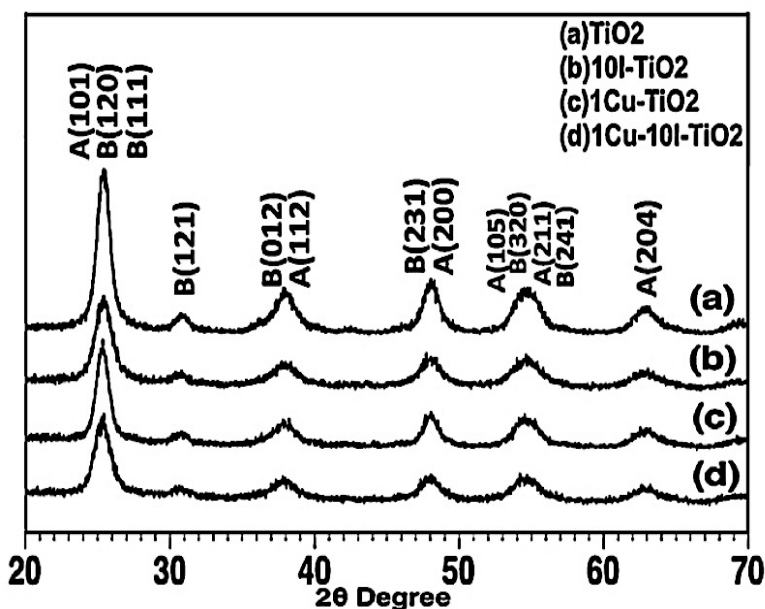


Figure 3.1 XRD patterns of TiO₂ (a), 10I-TiO₂ (b), 1Cu-TiO₂ (c), and 1Cu-10I-TiO₂ (d) samples. (A=anatase; B=brookite)

(i.e., 1Cu–10I–TiO₂) resulted in a sample with the expected characteristics, i.e., similar phase content as 1Cu–TiO₂ (since iodine does not affect the phase content) and an anatase crystal size that was in between that of 1Cu–TiO₂ and 10I–TiO₂ (Cu increased while I reduced the TiO₂ crystal size). Interestingly, the surface area of 1Cu–10I–TiO₂ was the highest (146.4 m²/g) among all the measured samples, which may relate to its smallest brookite crystal size, as shown in **Table 3.1**. Unlike anatase, the crystal size of brookite does not apparently relate to the catalyst composition. Brookite TiO₂ is much less studied in the literature and the lack of understanding of doped brookite warrants further investigation.

Table 3.1 Phase content and average size of Cu-I-TiO₂ samples obtained from X-ray diffraction, band gap from optical spectroscopy, and specific surface area from BET analysis (A:anatase; B:brookite).

	Phase content (%)		Crystal size (nm)		BET (m ² /g)
	A	B	A	B	
TiO ₂	70	30	8.9	4.8	117.3
10I–TiO ₂	67	33	5.6	5.3	128.2
1Cu–TiO ₂	54	46	9.6	4.1	95.3
1Cu–10I–TiO ₂	58	42	6.9	3.7	146.4

Figure 3.2 shows the results of SEM/EDX analyses of the 1Cu–10I–TiO₂ sample. Agglomerates of TiO₂ nanoparticles were observed in the SEM image. No textural difference was found in the SEM images between pure TiO₂, single ion-modified, and co-modified TiO₂ samples. The EDX analyses confirm the presence of Cu and I in the TiO₂ sample. In addition, the element of Cl was also identified (at 2.6 keV), since CuCl₂ was used as the Cu precursor in the wet-impregnation process.

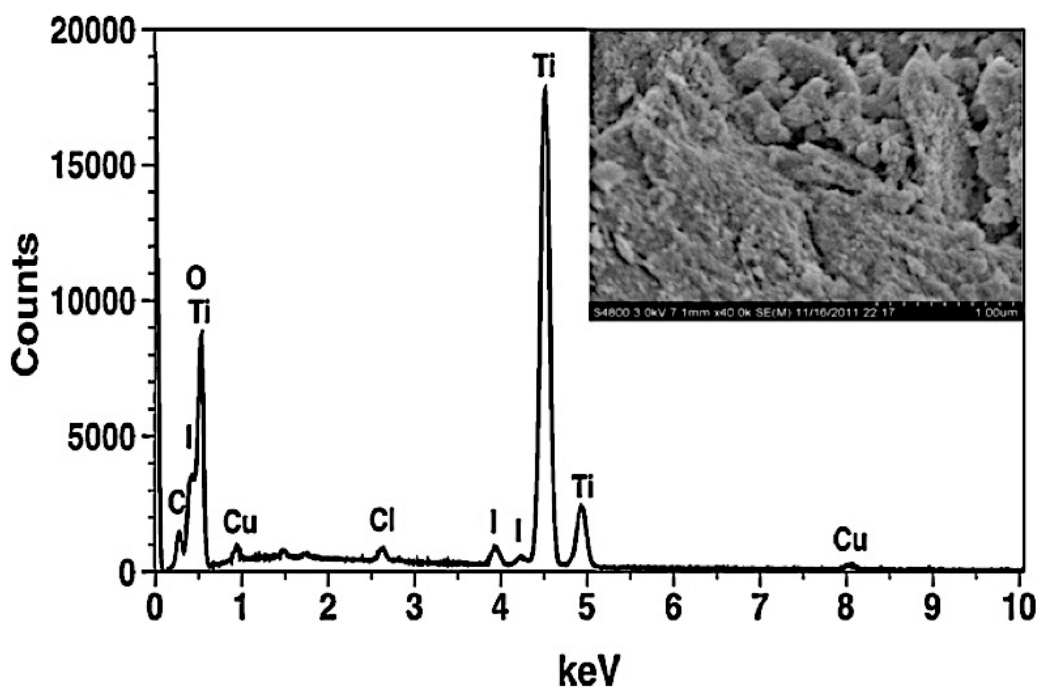


Figure 3.2 EDX analysis and SEM image of 1Cu-10I-TiO₂ sample

The UV-vis diffuse reflectance spectra (converted to absorbance) of pure TiO₂, 1Cu-TiO₂, 10I-TiO₂ and Cu-10I-TiO₂ samples with different Cu concentrations are shown in **Figure 3.3**. The absorption edge of pure TiO₂ is around 400 nm. For the 1Cu-TiO₂ sample, the absorption edge is only slightly shifted as compared to pure TiO₂. This result is in agreement with our previous research that suggested that impregnation of Cu on TiO₂ did not have a prominent effect on the optical property[62]. For all I-doped TiO₂, with or without Cu, the absorption edge shifted to the visible region, in agreement with the yellow color of the I-doped TiO₂ samples. The Cu concentration on the Cu-10I-TiO₂ samples (at a constant I doping level) did not significantly affect the light absorption. These optical properties support the conclusions that Cu that is deposited on the surface does not change the TiO₂ band structures, and iodine that is doped in the lattice may generate intra-band-gap states in TiO₂.

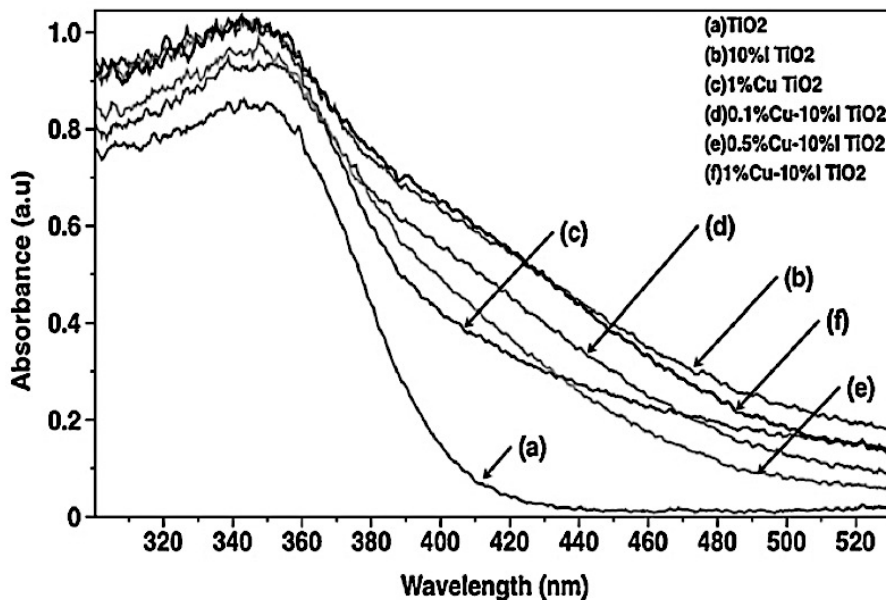


Figure 3.3 UV-vis diffuse reflectance spectra of the Cu/I-TiO₂ samples displayed in absorbance

3.3.2 Photocatalytic ability of Cu-I-TiO₂ catalysts

A series of background tests were first conducted to prove that any carbon-containing compounds in the effluent gas measured by the GC indeed originated from CO₂ through photocatalytic reactions. First, tests were conducted using CO₂ and H₂O vapor as the purging and reaction gases for the cases of (1) empty reactor and (2) blank glass-fiber filter in the reactor. No carbon-containing compounds were produced under either UV or visible irradiation in each of the two cases. This demonstrates that the reactor and the glass-fiber filter were clean and that the CO₂ conversion could not proceed without the photocatalyst. Second, pure helium (instead of CO₂) and water vapor were used as the purging and reaction gases, and the system was tested with the catalyst loaded in the reactor. Again, no carbon-containing compounds were produced by the catalyst under either UV or visible irradiation. This verified that the catalyst was clean (i.e., no interference from organic residues) and that any C-containing gases that were produced

were derived from CO_2 in the reaction gases.

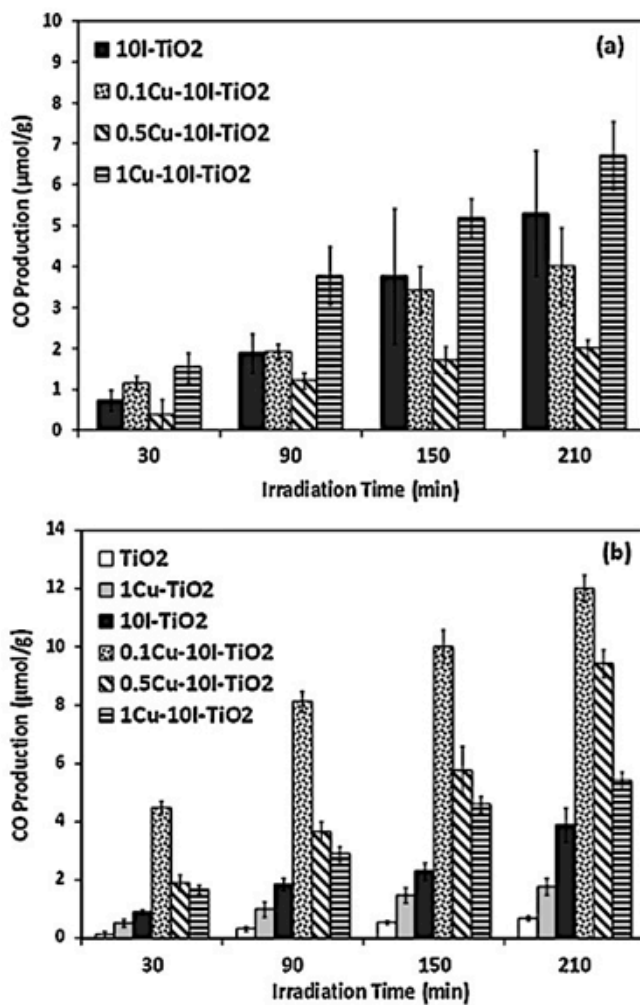


Figure 3.4 CO yield under visible light irradiation (a) and UV/vis irradiation (b)

purging and reaction gases, and the system was tested with the catalyst loaded in the reactor.

CO_2 photoreduction with water vapor over TiO_2 -based catalysts was studied in a batch mode for a period of 210 min for each test. Figure 3.4 shows the yield of CO from CO_2 reduction as a function of illumination time for the various catalysts under visible light ($\lambda > 400$ nm) and UV-vis irradiation ($\lambda > 250$ nm). Each sample was tested twice and the

average yields and error bars are shown in Figure 3.4. Under visible light, no activity of CO_2 reduction was observed for either pure TiO_2 or 1Cu-TiO_2 . Thus, zero activities are not shown in Figure 3.4 a. This result is consistent with the inability of TiO_2 or 1Cu-TiO_2 to absorb visible light, as shown in Figure 3.3. All I-doped TiO_2 samples exhibited visible light activities for CO_2 photoreduction to CO , and the production was almost linear with illumination time (**Figure 3.4 a**). Among the three Cu-10I-TiO_2 samples with different Cu concentrations (0.1, 0.5, and 1%), 1%Cu appeared to be the optimum material, having a CO production of $6.7 \mu\text{mol g}^{-1}$ at 210 min. However, only the 1Cu-10I-TiO_2 sample demonstrated a higher activity than the 10I-TiO_2 sample ($5.3 \mu\text{mol g}^{-1}$ at 210 min) while the other two co-modified samples 0.1Cu-10I-TiO_2 and 0.5Cu-10I-TiO_2 were inferior to 10I-TiO_2 . Very few studies have reported CO_2 photoreduction with water under visible light. Varghese et al.[81] used an N-doped TiO_2 nanotube array sputtered with Cu for CO_2 photoreduction with water vapor under sunlight and reported a production rate of $0.3 \mu\text{mol g}^{-1} \text{h}^{-1}$ ascribed to the visible light portion (or 3% of the total photocatalytic activity under sunlight). Our production rate under visible light (e.g., $1.9 \mu\text{mol g}^{-1} \text{h}^{-1}$ for 1Cu-10I-TiO_2) is much higher than that reported by Varghese et al.[81], while our raw materials are cheaper and our synthesis method is simpler, although the intensity of visible light in our work was approximately four times as much as that of sunlight.

Under UV-vis irradiation (**Figure 3.4 b**), very different activity results were observed from those under visible light. Pure TiO_2 had the lowest activity, while single ion-modified TiO_2 samples (1Cu-TiO_2 and 10I-TiO_2) exhibited enhanced, yet small

activities. Cu and I co-modified TiO₂ samples had remarkably higher activities, while the 0.1%Cu sample appeared to be the best among the three Cu–10I–TiO₂ samples. While the deposited Cu species may act as hole scavengers and thus enhance the CO₂ reduction rate, the anion species (e.g., Cl⁻) present on the catalyst and the dispersion of Cu species were found to have significant effects on the reaction rate and product selectivity.

Another significant result shown in **Figure 3.4** is that the 1Cu–10I–TiO₂ sample led to a higher level of CO production under visible light (6.7 μmol g⁻¹ CO production) as compared to that under UV–vis irradiation (5.4 μmol g⁻¹ CO production), while the opposite trend was observed for the 0.5Cu–10I–TiO₂ and 0.1Cu–10I–TiO₂ samples. Similarly, in our previous research[77], the 10I–TiO₂ sample had a higher activity for CO₂ photoreduction to CO under visible light than under UV–vis light irradiation, while the sample with lower iodine concentration, 5I–TiO₂, had an opposite trend. In addition, in this work all three Cu–I–TiO₂ samples exhibited higher activities than the I–TiO₂ sample under UV–vis light but two out of three Cu–I–TiO₂ samples with lower Cu concentrations had lower activities than the I–TiO₂ sample under visible light. All these results suggest that the presence and concentrations of the modifiers (Cu and I) have an important role in catalytic activity with different excitation sources. A general observation is that to achieve an optimum activity, a higher modifier concentration is needed under visible light (e.g., 10I–TiO₂ rather than 5I–TiO₂[77]; 1Cu–10I–TiO₂ rather than 0.5Cu–10I–TiO₂ and 0.1Cu–10I–TiO₂) but a lower modifier concentration is needed under UV–vis light. A possible reason is that very high modifier concentrations may lead to the formation of recombination centers, particularly when there is a larger population

of photo-induced electron-hole pairs (i.e., under UV-vis light).

3.3.3 Product selectivity and reaction mechanism

Besides the formation of CO as a major product, two minor products, methyl chloride or chloromethane (CH_3Cl) and methane (CH_4) were also observed using certain catalysts under certain excitation sources. The existence of CH_3Cl was identified through a GC/MS measurement and calibrated by a standard (2000 $\mu\text{g}/\text{ml}$ CH_3Cl in methanol, Restek). The measured amounts of photoreduction products under all of the experimental conditions are summarized in **Table 3.2**. The production of CH_4 was only observable under UV-vis light irradiation and was only prominent for the Cu-TiO₂ sample. The production of CH_3Cl was observable only when Cu was incorporated into the catalyst, apparently due to the use of CuCl_2 as the Cu precursor. The existence of Cl species was confirmed by the EDX analyses, as previously described. The yield of CH_3Cl for the Cu-I-TiO₂ samples increased with the concentration of Cu (and Cl) on the catalyst. In an additional experiment using $\text{Cu}(\text{NO}_3)_2$ as the Cu precursor for the catalyst (i.e., 1CuNO₃-10I-TiO₂), no formation of CH_3Cl was observed, while adding KCl together with $\text{Cu}(\text{NO}_3)_2$ (i.e., 1CuNO₃+KCl-10I-TiO₂) in the catalyst precursor resulted in the formation of CH_3Cl (see **Table 3.2**). These results again confirmed that the source of Cl in CH_3Cl was from the precursor solution.

Table 3.2 Amount of CO₂ photoreduction products measured at 210 min under visible and UV-vis light irradiation.Amounts of CO₂ photoreduction products measured at 210 min under visible and UV-vis light irradiation.

Sample	Visible light irradiation			UV/vis light irradiation		
	CO μmol g ⁻¹	CH ₃ Cl μmol g ⁻¹	CH ₄ μmol g ⁻¹	CO μmol g ⁻¹	CH ₃ Cl μmol g ⁻¹	CH ₄ μmol g ⁻¹
TiO ₂	0	0	0	0.7	0	0
10I-TiO ₂	5.3	0	0	3.9	0	0
1Cu-TiO ₂ ^a	0	0	0	1.8	0.49	0.38
0.1Cu-10I-TiO ₂ ^a	4.0	0.08	0	12.0	0	0
0.5Cu-10I-TiO ₂ ^a	2.0	0.24	0	9.4	0.12	0.04
1Cu-10I-TiO ₂ ^a	6.7	0.38	0	5.4	0.15	0.04
1Cu ^{NO₃} -10I-TiO ₂ ^b	n/m	n/m	n/m	1.5	0	0.09
1Cu ^{NO₃+KCl}} -10I-TiO ₂ ^c	1.5	0.26	0	n/m	n/m	n/m

n/m: not measured.

^a CuCl₂ was used as the Cu precursor.^b Cu(NO₃)₂ was used as the Cu precursor.^c Cu(NO₃)₂ and KCl were used as the precursor with Cu:Cl = 1:2.

This research is the first time to report the formation of CH₃Cl as a result of CO₂ photoreduction on Cu-loaded TiO₂ when a chlorinated precursor was used. The formation of a Cl⁻ labeled final product (CH₃Cl) may provide unique insights into the reaction mechanism of CO₂ reduction that has not previously been articulated in the literature. The path to CH₃Cl formation is likely through the reaction of a methyl radical (CH₃•) and a chlorine radical (Cl•). The generation of Cl• is a result of the oxidation of chloride ions with photo-induced holes. CH₃• was reported to be one of the reaction intermediates for CO₂ photoreduction to CH₄ on TiO₂, and was confirmed by electron paramagnetic resonance (EPR) spectroscopy. The possible reaction pathways during the CO₂ reduction process in this work are listed as follows, and the reaction mechanism is illustrated in **Figure 3.5**.

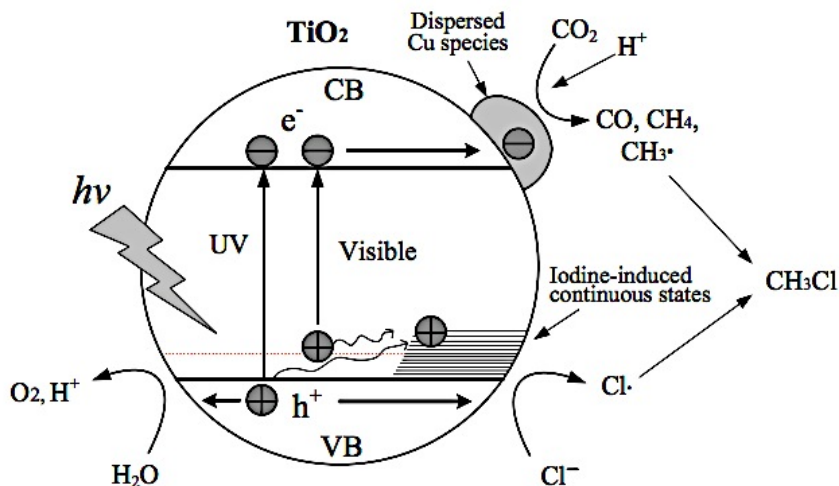
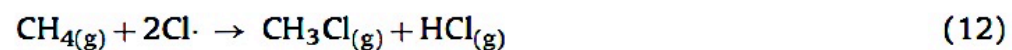
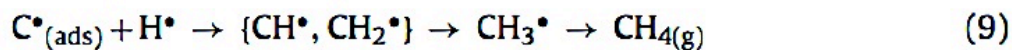
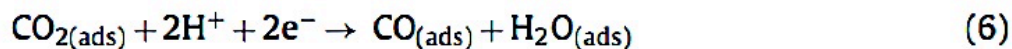


Figure 3.5 Mechanism of Cu/Iodine co-doped TiO₂ for CO₂ reduction



Reactions (1)–(8) suggest that CO₂ is first reduced to CO through a two-electron and two-proton reaction, which can be further reduced to surface adsorbed C species. These adsorbed C species are intermediates for the generation of CH₄ and CH₃Cl present in the

final products (reactions (9)–(11)). The produced amounts of CH_4 and CH_3Cl are far less than that of CO since CO is possibly the precursor. The produced amount of CH_3Cl is generally higher than that of CH_4 (**Table 3.2**). This result may be because of two reasons: (1) Cl^\bullet reacts with CH_3^\bullet at a higher rate than H^\bullet does and/or the abundance of Cl^\bullet is larger than H^\bullet , and (2) CH_4 reacts with Cl^\bullet to yield CH_3Cl as shown in reaction (12). Nevertheless, the formation mechanism of CH_3Cl should be analogous to that of CH_4 . The detection of CH_3Cl in this work verifies the EPR results in the literature that indicates that CH_3^\bullet is an intermediate species in the CO_2 photoreduction process. An additional important finding in our experiments is that the color of the catalyst turned darker during the process of CO_2 photoreduction with H_2O , and it would gradually restore to (or close to) its original color if the used catalyst was exposed to air at room temperature. The darkening in catalyst color may be an indication of the formation of intermediate C species adsorbed onto the surface. Since these species are unstable, they are difficult to measure under the experimental settings that were used. This intriguing phenomenon and the identification of reaction intermediates will be investigated in full detail in our future research by using in situ Fourier transform infrared (FTIR) spectroscopy.

To further investigate the effects of Cl species on CO_2 photoreduction, the activities of three catalysts were compared: 1Cu–10I–TiO (*CuCl as the precursor*), 1CuNO₃–10I–TiO₂ (*Cu(NO₃)₂ as the precursor*), and 1CuNO₃–10I–TiO₂ (*Cu(NO₃)₂ + KCl as the precursor*), and the results are as listed in Table 3.2. The 1CuNO₃–10I–TiO₂ catalyst had a CO production ($1.5 \mu\text{mol g}^{-1}$) that was less than one third of the CO production that

was observed using 1Cu–10I–TiO₂ (5.4 μmol g⁻¹) under UV–vis irradiation, although the yield of CH₄ was comparable. The 1CuNO₃+KCl–10I–TiO₂ catalyst also had a much lower CO production (1.5 μmol g⁻¹) than 1Cu–10I–TiO₂ (6.7 μmol g⁻¹) under visible light irradiation, although the produced amounts of CH₃Cl were close to each other. These results indicate that CuCl₂ as the Cu precursor is more effective than Cu(NO₃)₂. A similar finding was reported by Tseng et al.[86] that the choice of a CuCl₂ precursor increased the Cu dispersion and thus resulted in a higher CO₂ photoreduction rate as compared to that obtained with a copper acetate precursor. In addition to the enhanced Cu dispersion due to CuCl₂, the surface Cl ions act as hole-scavengers (**reaction (10)**) and thus help to separate the electron–hole pairs and enable more electrons to react with CO₂. The result that a mixture of Cu(NO₃)₂ and KCl as the Cu precursor was less effective in producing valuable products as compared to CuCl₂ suggests that the additional ions (NO₃⁻, K⁺) may have a negative effect on Cu dispersion. On the other hand, using CuCl₂ as the precursor led to unwanted products (e.g., CH₃Cl) even though its CO production rate was about three times higher than that using Cu(NO₃)₂ as the precursor. Therefore, more attention should be paid by the research community to the choice of catalyst modifier precursors when undertaking CO₂ photoreduction studies.

3.4 Conclusion

In this study, Cu and I co-modified TiO₂ catalysts (Cu–I–TiO₂) were synthesized with iodine doped into the TiO₂ lattice and Cu deposited on the TiO₂ surface. The material properties and catalytic activities for CO₂ photoreduction with water were compared

using pure TiO_2 , single-ion modified TiO_2 (Cu-TiO_2 and I-TiO_2), and co-modified catalysts (Cu-I-TiO_2). Iodine doping was responsible for visible light activity of the catalyst while Cu species, mainly Cu(I), facilitated charge transfer and enhanced CO_2 reduction. However, the catalytic activity and the optimum catalyst composition under visible or UV-visible light irradiation were different. Under UV-vis irradiation, the activity of the Cu-I-TiO_2 sample was higher than that of Cu-TiO_2 or I-TiO_2 , whereas, under visible light, Cu-I-TiO_2 was not always superior to I-TiO_2 . To achieve an optimum activity, a lower modifier concentration is needed under UV-vis light than under visible light, possibly because a high modifier concentration may lead to the formation of recombination centers. This work identified the generation of CH_3Cl from CO_2 reduction. The Cl species was derived from CuCl_2 , a frequently used Cu precursor. The information of CH_3Cl suggests that surface adsorbed carbon species and methyl radicals may be reaction intermediates, which warrants follow-up investigation using in situ IR spectroscopy. While using CuCl_2 as the Cu precursor resulted in a much higher CO_2 photoreduction rate than using $\text{Cu(NO}_3)_2$, the undesirable CH_3Cl in the reaction products may be a concern.

Chapter 4 Novel Anti-Fouling Fe₂O₃/TiO₂ Nanowire Membranes For Humic Acid Removal From Water

4.1 Research background

Membrane fouling caused by deposition of contaminants on membrane surface has been recognized as one of the major obstacles inhibiting the application of membrane technologies [12, 13]. Membrane fouling may dramatically shorten the lifetime of membrane module, deteriorate the quality of water produced and increase the operation cost.

To address the membrane fouling issue, fabrication of unconventional membranes such as titanium dioxide (TiO₂) nanowire membranes (Ti-NWM) has been reported in the literature [87, 88]. Under ultraviolet (UV) light irradiation, electron-hole pairs are generated on TiO₂ nanowires resulting in the formation of strong oxidants like hydroxyl radicals [68, 89], which are effective in mineralizing organic contaminants on the membrane surface and thus mitigate membrane fouling. Compared with TiO₂ nanoparticles, the Ti-NWM design can circumvent the separation and recovery of TiO₂ nanoparticles after wastewater treatment [87, 90], and thus it is more convenient to be used with lower capital and operation costs. However the wide band gap of TiO₂ (3.2 eV for anatase and 3.0 eV for rutile) restricts the photo-response of the Ti-NWM to only UV light irradiation. Since UV light accounts for only 5% of total solar energy, the Ti-NWM shows low photocatalytic activity under solar irradiation, and visible light portion (~50% of solar energy) of the sunlight is not utilized [91]. Therefore, it is necessary to increase the visible light absorption of the Ti-NWM to improve its photoactivity under solar irradiation.

Nonmetal element (e.g., N, C, S, F, I, etc.) doped TiO₂ has been widely reported to induce visible light responsive photocatalytic activity, where nitrogen doping is the most extensively studied [92-96]. N-doped TiO₂ nanowires have also been synthesized through thermal reduction in ammonia environment and the nanowire morphology can be largely preserved when reduction temperature was lower than 600 °C [97, 98]. Unfortunately, although N-doped TiO₂ shows visible light activity, its activity under UV light is normally impaired, most likely due to the doping induced formation of recombination centers [97, 99]. Another method is to modify TiO₂ with other semiconductors with smaller band gap to form heterojunctions for improvement in visible light absorption and overall photocatalytic activity [95, 96]. Fe₂O₃ has been used as one of such modifiers to TiO₂ due to its small band gap (2.2 eV for α -Fe₂O₃), low cost and non-toxicity [45, 46, 100-102]. Cong et al. [45] fabricated α -Fe₂O₃/TiO₂ nanorod/nanotube composite by filling TiO₂ nanotubes with Fe₂O₃ and they showed higher phenol degradation efficiency and stronger photo-responsibility for visible light compared with TiO₂ nanotubes alone. Zhou et al. [102] showed that a mesoporous α -Fe₂O₃/TiO₂ bifunctional composite can take the advantages of enhanced arsenite adsorption by Fe₂O₃ and the photocatalytic oxidation of As (III) to As (V) by TiO₂.

Therefore, we hypothesize that combining the increased visible light photocatalytic response and higher adsorption of certain water contaminants onto Fe₂O₃ would make Fe₂O₃ modified Ti-NWM a more promising membrane than Ti-NWM in water treatment, where sunlight instead of UV light can be utilized without secondary contamination of TiO₂ nanoparticles. The overall objective of this study is to fabricate a novel interwoven Fe₂O₃/TiO₂ nanowire membrane (FeTi-NWM) and to test its

performances for humic acid removal from water under sunlight. The novelty of this work is four-fold: 1) interwoven $\text{Fe}_2\text{O}_3/\text{TiO}_2$ nanowire membranes have not been synthesized before; 2) such FeTi–NWM has not been tested under sunlight for organics removal from water; 3) the finding on anti-fouling ability of the FeTi–NWM under sunlight is original and not reported before; and 4) this paper elucidates a new mechanism of charge transfer between Fe_2O_3 and TiO_2 that may have led to the anti-fouling feature.

4.2 Experimental

4.2.1 Synthesis of $\text{Fe}_2\text{O}_3/\text{TiO}_2$ nanowire membranes (FeTi–NWM)

The TiO_2 nanowires were fabricated by a method modified from a previous report [103]. Briefly, 1.0 g of TiO_2 nanopowder (P25, Degussa) was mixed with 65 mL of 10 M NaOH and 65 mL ethanol successively and transferred to a Teflon-lined autoclave. After hydrothermal reaction at 160 °C for 16 h, a white pulp suspension containing TiO_2 nanowires was collected and washed with 0.1 M hydrochloric acid and deionized water alternately until pH equals near 7. The TiO_2 nanowires were then suspended in deionized water for further use. The synthesis of the Fe_2O_3 nanowires followed the method reported by Guo et al. [42]. 0.15 M FeCl_3 solution was mixed with isopropanol, to which 3 mM nitrilotriacetic acid (NTA) was added. After thorough stirring, the mixture was transferred into a Teflon-lined autoclave and hydrothermally treated at 180 °C for 24 h. The resultant floccules were collected and washed with deionized water and ethanol, and then vacuum-dried at 60 °C for 1 h.

The as-prepared TiO_2 and Fe_2O_3 nanowires were used to fabricate FeTi–NWM by a vacuum filtration and hot pressing method, as shown in **Figure 4.2**. Water solution containing well mixed Fe_2O_3 and TiO_2 nanowires was filtered through a glass-fiber filter

paper (P4 grade, Fisher brand) by vacuum. After drying, the filter paper together with the Fe_2O_3 and TiO_2 nanowire layer was hot-pressed for 10 min. The nanowire layer was then peeled off and finally calcined at $400\text{ }^\circ\text{C}$ for 2 h to form FeTi-NWM. The weight ratio of $\text{Fe}_2\text{O}_3/\text{TiO}_2$ in the FeTi-NWM has been varied in this study, and a 1:1 ratio was found to be the optimum (see **Figure 4.1**). Hence, in this paper, the $\text{Fe}_2\text{O}_3/\text{TiO}_2$ ratio of 1:1 was used for FeTi-NWM unless specified. For comparison, Ti-NWM has also been fabricated using the same procedure by using only TiO_2 nanowires.

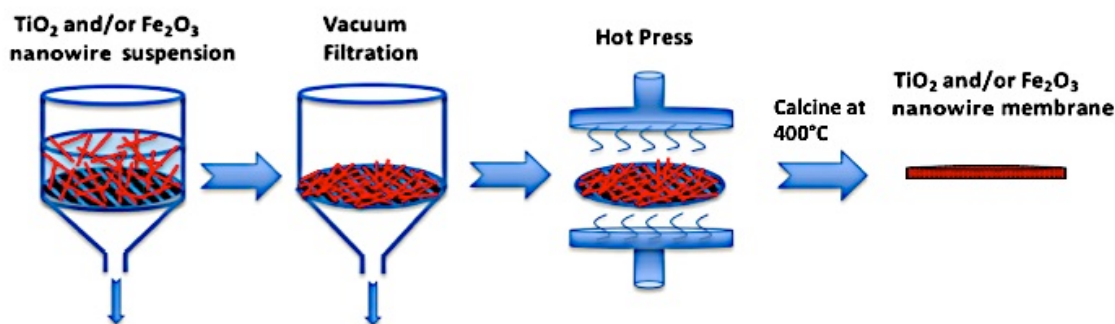


Figure 4.1 Procedure of synthesizing Ti-NWM and FeTi-NWM.

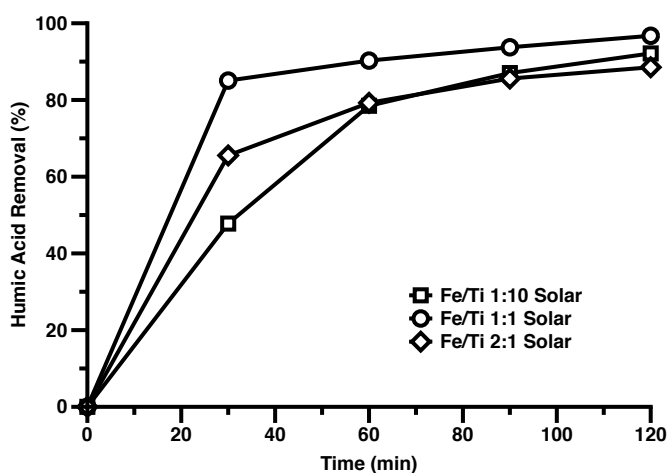


Figure 4.2 Humic acid removal under solar irradiation by FeTi-NWM with different $\text{Fe}_2\text{O}_3/\text{TiO}_2$ mass ratios.

4.2.2 Membrane Characterization

The microstructure of the Ti–NWM and FeTi–NWM were obtained by scanning electron microscopy (SEM) (Hitachi S570). The diameters of the TiO_2 and Fe_2O_3 nanowires and the membrane thickness were estimated based on the SEM images. The pore size of the membrane was estimated by evaluating the filtration efficiency of polystyrene microsphere (PS) (Alfa Aesar) solutions containing monodispersed microspheres with diameters of 0.05, 0.1, and 0.2 μm , respectively [6]. The monodispersity of the microspheres was verified by SEM analysis (see **Figure 4.3**). The estimated pore size of the membrane was determined by the diameter of the microspheres

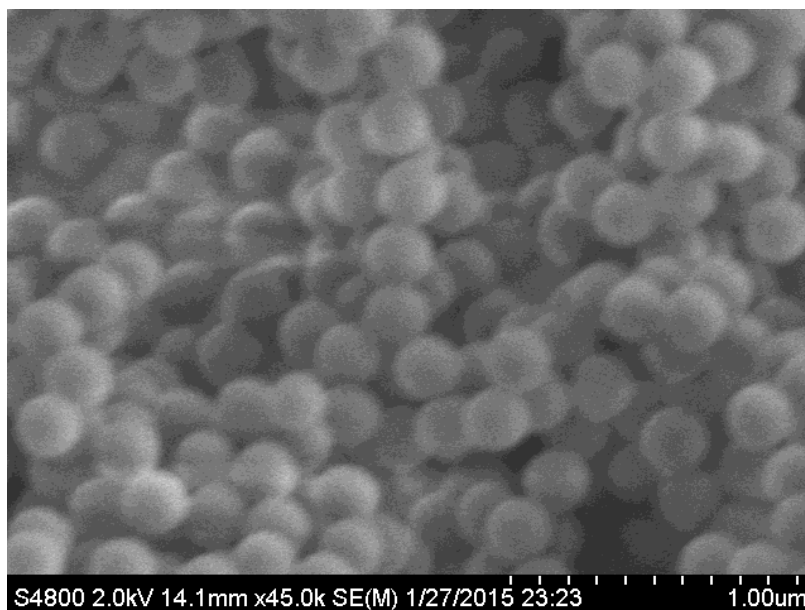


Figure 4.3 SEM image of the 0.2 μm polystyrene microsphere.

that have 90% filtration efficiency by the membrane [6]. The concentration of microspheres in the initial solution (C_0) was kept at 0.0033 wt.% for all tests with

different sizes. The concentration of microspheres in the permeate solution after filtration through the membrane was C_a . Both C_o and C_a were measured by a TOC analyzer (Shimadzu) via a calibration curve. The filtration efficiency of microspheres by the membrane was calculated by:

$$\text{Filtration efficiency} = \left(1 - \frac{C_a}{C_o}\right) \times 100\% \quad (1)$$

The crystal structures of nanowires in the membrane were identified by X-ray diffraction (XRD) (Scintag XDS 2000) with Cu K α radiation operated at 40 mA in the 2θ range from 20° to 70° at a scan rate of $1^\circ/\text{min}$. The UV–vis absorption spectrums of the Ti–NWM and the FeTi–NWM were recorded with a UV–vis spectrophotometer (Ocean Optics).

4.2.3 Humic acid removal under different light conditions

Humic acid (HA) has been identified as one of the major contaminants leading to membrane fouling in water treatment processes [104], thus its removal was investigated in the current study. A recirculating water filtration system with nanowire membranes placed inside a stainless steel reactor was used, which is shown in **Figure 4.5**. Pump I was used to load the HA solution into the reactor (while valve II was closed) till a water depth around 1.7 cm (corresponding to a water volume of 90 ml). Then the feed solution was stopped by switching valve I, and in the meantime valve II was switched to open and pump II was turned on to recirculate the 90 ml solution through the membrane reactor. The initial HA concentration in the solution was 200 mg/L, which is much higher than that in natural waters as we expected to augment the membrane fouling phenomenon and shorten the time to observe fouling. The recirculating flow rate was at 9 ml/min (or 120 L/h/m²). Hence, every 10 min the entire solution was expected to circulate through the

membrane once. Tests under other flow rates (2, 5, and 15 ml/min) were also conducted as comparisons (**Figure 4.4**) but 9 ml/min appeared to be an appropriate flow rate that was used for the majority of this work unless specified.

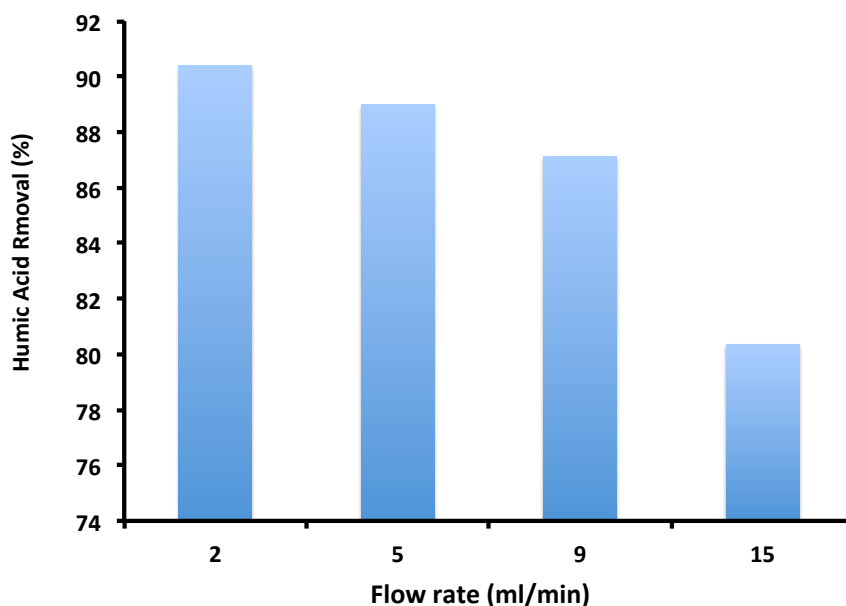


Figure 4.4 Humic acid removal using the FeTi-NWM under different flow rates

A 150 W solar simulator (Oriel[®] Sol1A, Newport) was used as the light source. Visible light irradiation was obtained by applying a 400 nm cut-off UV filter on the solar light beam. The measured light intensity for the solar simulator was around 8 and 29 mW/cm² in the UV (< 400 nm) and visible light (400 – 700 nm) regions, respectively. Each test was performed for 2 h and water permeation samples were collected at an interval of 30 min for HA concentration analysis. The UV-vis absorbance at 465 nm was measured to calculate the HA concentration using a standard curve prepared with known concentrations of HA solutions. HA removal at a recirculation time t was calculated by the following equation:

$$\text{Humic Acid Removal} = \left(1 - \frac{H_t}{H_0}\right) \times 100\% \quad (2)$$

where H_0 was the initial HA concentration, 200 mg/L, and H_t was the HA concentration collected at the sample port (effluent side of the reactor) at time t .

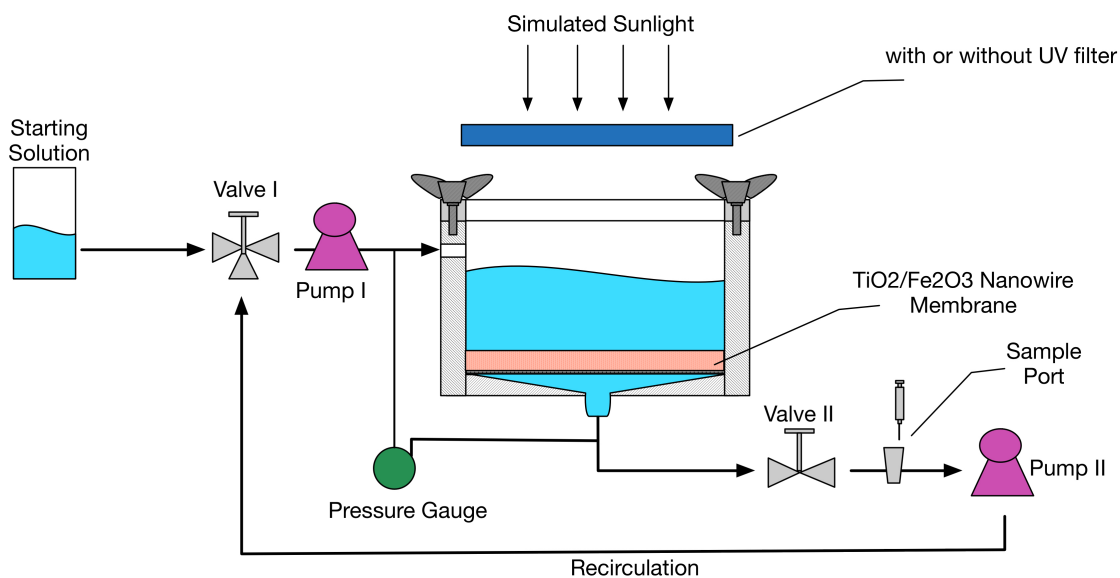


Figure 4.5 Schematic of the water filtration system for HA removal using nanowire membranes under simulated sunlight.

4.2.4 Long-term test of anti-fouling capability

To investigate the anti-fouling behavior of the FeTi–NWM, long-term tests with or without solar irradiation have been performed using the same system as described in **Figure 4.5**. The membrane was tested in 4 consecutive cycles and each cycle lasted for 3 h. Fresh 200 mg/L HA solution was used at the beginning of each cycle and the system was maintained a water flow rate of 9 ml/min (or 120 L/h/m²). In a separate experiment, transmembrane pressure, an important indicator for membrane fouling was measured by a digital pressure gauge (DPG409, Omegadyne) during a 10 h continuous flow test using 200 mg/L HA solution.

4.3 Results and discussion

4.3.1 Morphological, structural and optical properties of the nanowire membranes

The SEM images of the nanowires (all after calcinations) and the photos of resultant Ti–NWM and FeTi–NWM are shown in **Figure 4.6**. As can be seen from **Figure 4.6a**, the diameters of the randomly oriented TiO_2 nanowires are generally less than 100 nm, and the Ti–NWM displayed a white color (inset of **Figure 4.6a**). **Figure 4.6b** shows severe aggregation of the Fe_2O_3 nanowires and the diameters of the bundled Fe_2O_3 nanowires are in the range of few hundred nanometers. The difficulty of dispersing Fe_2O_3 nanowires alone in an aqueous solution is the reason why a Fe–NWM was not made in this study. **Figure 4.6c** shows overlapped or interwoven $\text{Fe}_2\text{O}_3/\text{TiO}_2$ nanowires where the wider ones are most likely Fe_2O_3 and narrower ones are TiO_2 , based on the diameter information obtained from **Figure 4.6a** and **Figure 4.6b**. The FeTi–NWM displayed a reddish color due to the presence of Fe_2O_3 nanowires (inset of **Figure 4.6c**). **Figure 4.6d** and **Figure 4.6e** show the cross-section SEM images of the Ti–NWM and FeTi–NWM, and one can observe the thicknesses of both nanowire membranes are comparable (ca. 200 μm). The filtration efficiency of 0.2, 0.1, and 0.05 μm microspheres by the FeTi–NWM were measured to be 96%, 95%, and 83%, respectively, thus the estimated pore size of the FeTi–NWM was somewhere between 0.05 and 0.1 μm according to the definition specified in Section 4.2. The filtration efficiency of 0.05 μm microspheres by Ti–NWM was also measured to be 88%, which is comparable and slightly greater than the filtration efficiency of the FeTi–NWM (83%). This indicates that the addition of Fe_2O_3 nanowires had a minimal effect on the pore structure of the membrane.

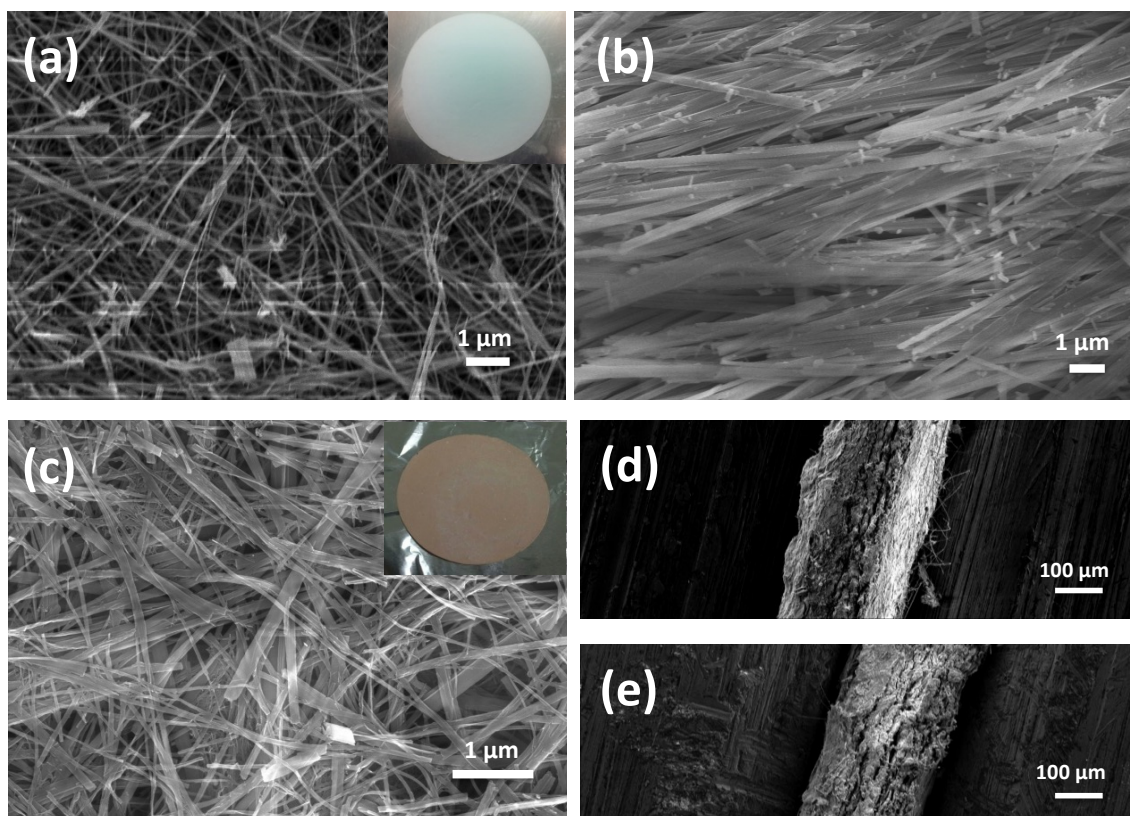


Figure 4.6 SEM images showing the morphology of (a) Ti-NWM, (b) calcined Fe_2O_3 nanowires, (c) FeTi-NWM, (d) cross-section of Ti-NWM, and (e) cross-section of FeTi-NWM. The insets of (a) and (c) show photos of 75 mm diameter Ti-NWM and FeTi-NWM, respectively.

Figure 4.7 gives the XRD patterns of the nanowire membranes after calcination. The Ti-NWM shows anatase TiO_2 (JCPDS 21-1272) crystals (**Figure 4.7 a**) while the Fe_2O_3 nanowires demonstrates $\alpha\text{-Fe}_2\text{O}_3$ (JCPDS 33-0664) crystal structure (**Figure 4.7 b**). The crystal structure FeTi-NWM was a simple assembly of anatase TiO_2 and $\alpha\text{-Fe}_2\text{O}_3$ (**Figure 4.7 c**). The XRD patterns in **Figure 4.7** are consistent with those reported in the literature regarding TiO_2 and Fe_2O_3 nanowires synthesized by similar methods [105]. The anatase structure of the TiO_2 nanowire is preferred to other crystal structures of TiO_2 (e.g., rutile, brookite) because of higher photocatalytic activity of anatase in general. [106, 107]

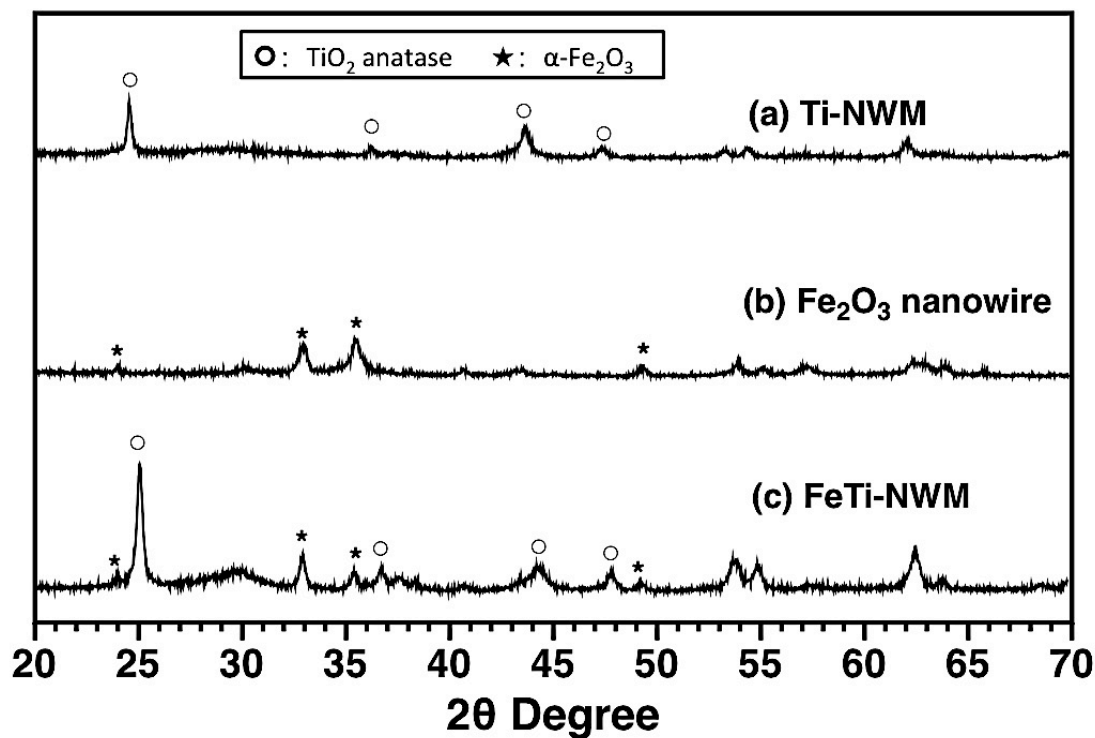


Figure 4.7 XRD patterns for (a) Ti-NWM, (b) Fe₂O₃ nanowires, and (c) FeTi-NWM, all after 400°C calcination.

Figure 4.8 gives the optical properties of the Ti-NWM and FeTi-NWM that were measured by UV-vis diffused reflectance spectroscopy (DRS). As can be seen, the Ti-NWM shows strong absorption of UV light with an absorption edge at about 385 nm, which matches the literature that anatase TiO₂ has a band gap around 3.2 eV [99]. The FeTi-NWM (with the addition of the Fe₂O₃ nanowire) exhibited adequate absorptions of both UV light and visible light, although the adsorption of UV light is a little weaker than that of the Ti-NWM. The absorption edge of FeTi-NWM is at about 610 nm, again in agreement with the reported band gap of α-Fe₂O₃ around 2.2 eV [100]. The higher absorption of visible light for the FeTi-NWM than the Ti-NWM agrees with those reported in the literature [101].

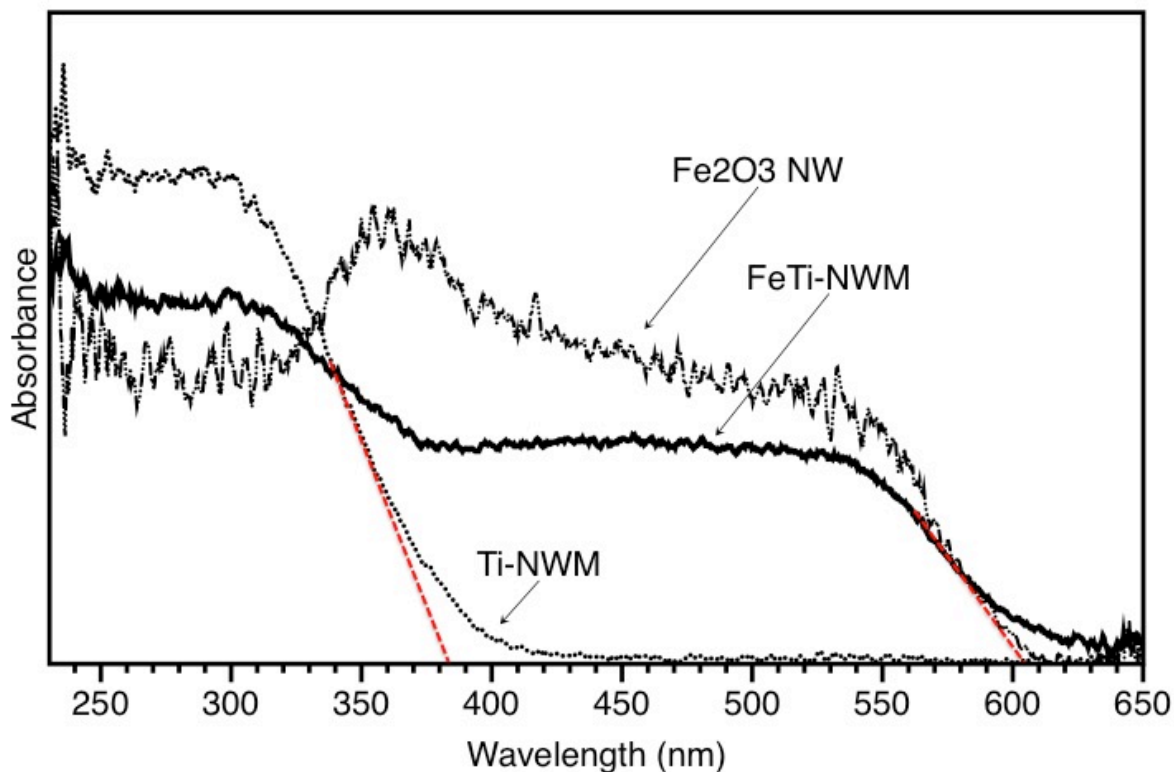


Figure 4.8 UV-vis spectra for Fe_2O_3 -NW, Ti-NWM and FeTi-NWM.

4.3.2 Humic acid removal under different experimental conditions

The optimum $\text{Fe}_2\text{O}_3/\text{TiO}_2$ mixing ratio in FeTi-NWM for HA removal was firstly investigated. The HA removal by the FeTi-NWMs with three $\text{Fe}_2\text{O}_3/\text{TiO}_2$ weight ratios (1:10, 1:1 and 2:1) were measured under solar irradiation in a 2 h test as described in Section 2.3. The FeTi-NWM with a $\text{Fe}_2\text{O}_3/\text{TiO}_2$ weight ratio of 1:1 was found to have the highest overall HA removal (~97%) and faster removal rate in the 30 min than the other two membranes (see **Figure 4.2**). Therefore, the FeTi-NWM with a $\text{Fe}_2\text{O}_3/\text{TiO}_2$ weight ratio of 1:1 was used in the following studies. In addition, experiments were conducted using the FeTi-NWM (1:1 Fe/Ti) under solar irradiation at four different recirculation flow rates (2, 5, 9, and 15 ml/min). The results for HA removal at 30 min are illustrated

in **Figure 4.4**. The results indicate that increasing the flow from 2 to 9 ml/min only decreased the HA removal from 91% to 87%, which is not a significant change. Further increasing the flow rate to 15 ml/min resulted in a larger drop in HA removal to 80%. Based on these results, the use of 9 ml/min for the majority of this work is reasonable considering a relatively larger flow rate and a higher removal are both desirable in practical applications.

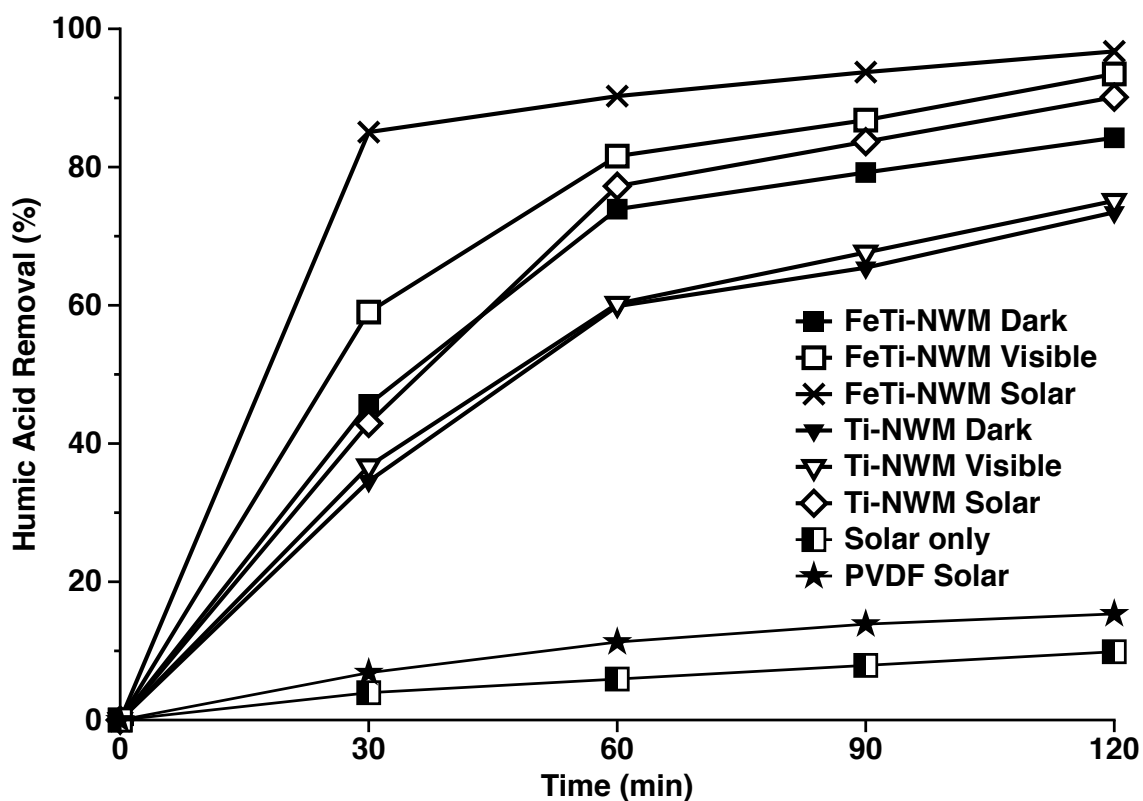


Figure 4.9 Humic acid removal in the dark, under visible light and solar light conditions using Ti-NWM and FeTi-NWM (a commercial PVDF membrane was also tested as a control).

Figure 4.9 gives the HA removal results under different light conditions using both Ti-NWM and FeTi-NWM. As can be seen, in the blank test (without nanowire membranes) only 10% of HA was removed under solar irradiation at the end of the 2 h

test. With the presence of nanowire membranes, the HA removal was significantly improved, due to both adsorption and photocatalytic degradation. Comparing the HA removal under dark conditions using both Ti–NWM and FeTi–NWM, it can be seen that near 84% of HA removal was achieved using the FeTi–NWM, while only 73% using the Ti–NWM. The improved HA removal by the FeTi–NWM under dark condition may be attributed to the enhanced adsorption of HA by the Fe₂O₃ nanowire, likely due to the electrostatic force between the Fe₂O₃ nanowire and the HA molecules [108, 109].

The improved adsorption of HA onto the surface of the FeTi–NWM may expedite membrane fouling if it is not chemically decomposed. Therefore, the capability of photocatalytic degradation of HA by the FeTi–NWM is preferred to prevent membrane fouling. As can be seen from **Figure 4.9**, 93% and 97% of HA removal was achieved by the FeTi–NWM under visible light and solar light conditions, respectively, after the 2 h test, while only 75% and 89%, respectively, for the Ti–NWM. The HA removal by Ti–NWM in the dark (73%) and under visible light (75%) was very close, indicating TiO₂ alone is not photocatalytically active under visible light, in agreement with its wide band gap (3.2 eV), and all the HA removal was due to adsorption. Under solar light, due to the UV portion that activated photocatalytic reactions, the HA removal by the Ti–NWM was increased to 89% compared with 75% under visible light only. For the FeTi–NWM, the HA removal under visible light (93%) was obviously higher than that in the dark (84%), suggesting a visible light activated HA degradation besides adsorption. The even higher HA removal under solar light (97%) by FeTi–NWM reveals that both UV light and visible light can contribute to the overall photocatalytic degradation of HA. Comparing the FeTi–NWM and Ti–NWM for HA removal under visible light only, the much higher

removal by FeTi–NWM (93%) than by Ti–NWM (75%) is mostly likely due to both enhanced adsorption of HA and promoted visible light photocatalytic activity induced by Fe₂O₃ addition to TiO₂.

We have also conducted TOC measurement of the effluent samples to correlate with the HA removal by FeTi–NWM under solar irradiation. As shown in **Figure 4.10**, the trend of TOC removal correlates well with that of HA removal but the TOC removal is in average about 20% lower than the HA removal. The TOC removal reached as high as 79% at the end of the 2 h testing. This result suggests that the majority of the HA was

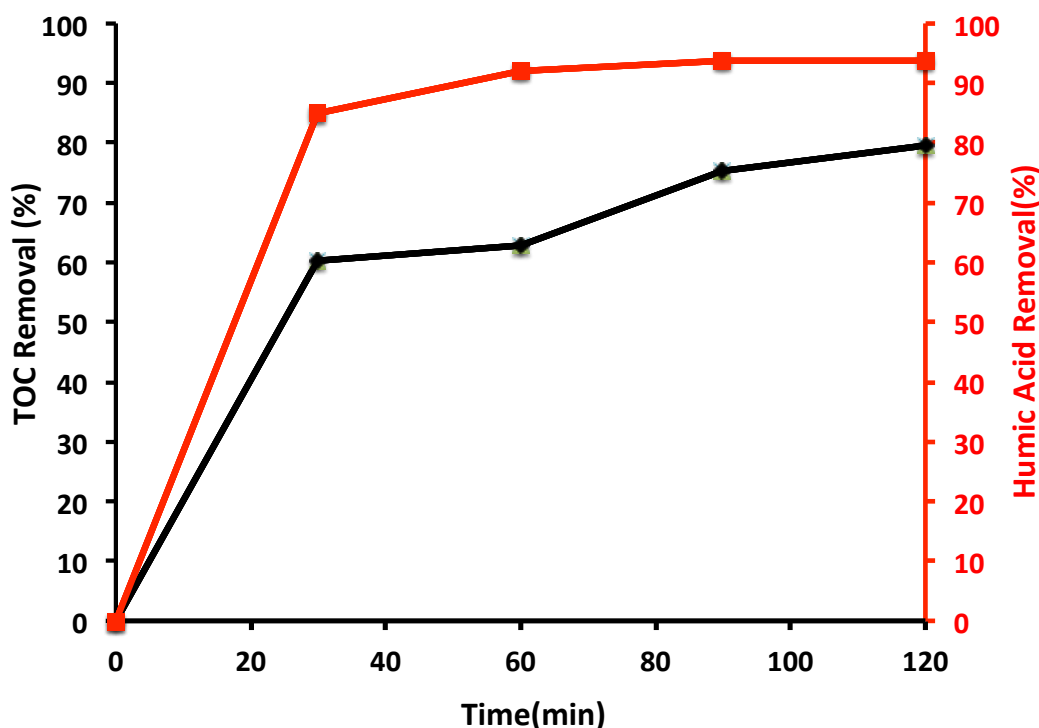


Figure 4.10 Humic acid removal and TOC removal by FeTi–NWM under solar irradiation

completely degraded to CO₂ and H₂O and a minor portion of it remained in the water as byproducts. This observed high HA removal (93%) is superior to that reported in the literature where only 60% HA removal was observed after 2 h under UV (356 nm)

irradiation at an initial HA concentration of 10 mg/L using TiO₂ nanoparticles [110]. The FeTi–NWM is also much more effective than a commercial polyvinylidene fluoride (PVDF) membrane (see **Figure 4.9**), which shows only 15% HA removal after 2 h under solar irradiation.

4.3.3 Long-term anti-fouling test results

A long-term test for HA removal using the FeTi–NWM and the Ti–NWM were conducted (4 cycles and 3 h in each cycle using fresh 200 mg/L HA) to further investigate the anti-fouling capability of the nanowire membranes. The results are given in **Figure 4.11**. As can be seen, 81% of HA was removed under dark condition using the Ti–NWM at the end of the 1st cycle, and the HA removal kept decreasing over cycles and reached 38% at the end of the 4th cycle (Columns A). Because a new batch of HA solution was used in each cycle but using the same membrane, the decreased HA removal with increasing number of cycles is likely because more membrane fouling has occurred, which decreased the adsorption of HA onto the nanowire surface. By contrast, the HA removal decreased only from 96% to 80% using the FeTi–NWM under dark condition (Columns C). The overall higher HA removal by FeTi–NWM than Ti–NWM in the dark is likely because of more and stronger adsorption sites available on Fe₂O₃ present on the nanowire membrane, which is in line with the results shown in **Figure 4.9**.

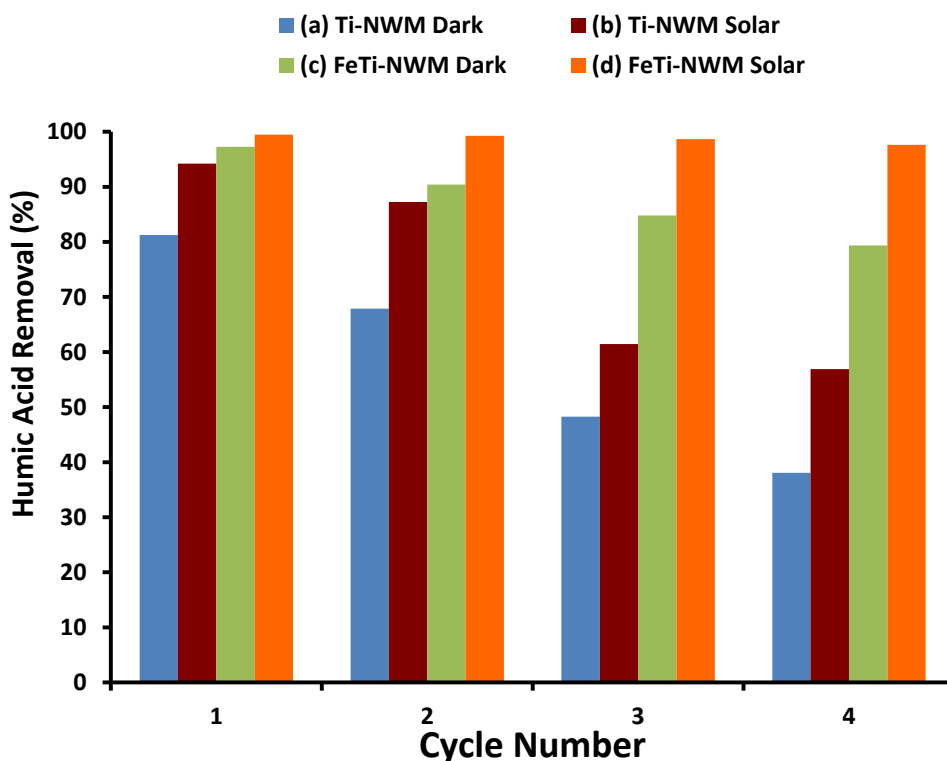


Figure 4.11 Long-term test for HA removal using FeTi-NWM and Ti-NWM (4 cycles and 3 h in each cycle with fresh 200 mg/L HA introduced at the beginning of each cycle).

Under solar irradiation, the HA removal by the Ti-NWM (Columns B) was higher than that in the dark condition for every cycle, but still it decreased significantly (from 93% to 58%) after 4 cycles. The result suggests that the rate of HA photodegradation on the Ti-NWM surface was slower than the rate of HA adsorption. The weak photoactivity of the Ti-NWM is likely because of the low intensity of UV light (5%) in the solar spectrum. The accumulated HA on the membrane surface may have also blocked the light penetration and reduce the photoactivity of the Ti-NWM. By contrast, the FeTi-NWM maintained a nearly stable and high HA removal (98%) even after tested four cycles (Columns D), suggesting the rate of HA photodegradation on the FeTi-NWM surface was able to keep pace with the rate of HA adsorption. In another word, minimal amount of HA is expect to accumulate on the FeTi-NWM and thus the blocking of sunlight by

deposited HA would not be an issue for FeTi–NWM. The enhanced photocatalytic activity under visible light induced by Fe_2O_3 may be the main reason. Overall, the FeTi–NWM showed much higher anti-fouling capability than the Ti–NWM during the long-term test. The photo of two FeTi–NWMs after the long-term test (one under solar irradiation and the other in the dark) is given in **Figure 4.12**. The two membranes were cut in half and put together for better contrast. The brown color on the left membrane indicates membrane fouling by HA in the dark. The clean membrane on the right indicates good anti-fouling ability under solar illumination.

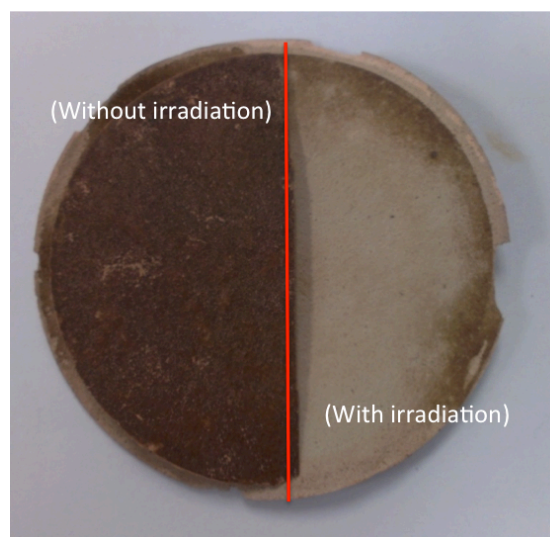


Figure 4.12 Photos of two FeTi–NWMs after the long-term test of HA removal, one with solar irradiation and the other without.

Transmembrane pressure of the Ti–NWM and FeTi–NWM during a separate 10 h continuous flow test under both dark and solar irradiation conditions was recorded, as shown in **Figure 4.13**. As can be seen, the transmembrane pressure was around 9 kPa for both Ti–NWM and FeTi–NWM at the beginning of the test. During the tests under dark conditions, the pressure increased almost linearly with time and reached 34 and 38 kPa

for Ti–NWM and FeTi–NWM, respectively, at the end of the 10 h test. The higher pressure change for FeTi–NWM than Ti–NWM suggests a larger amount of HA deposition. This is a clear indication of membrane fouling, and it agrees with the observation of severe HA deposition on the membrane in the dark illustrated in Figure 8. By contrast, under solar irradiation, the transmembrane pressure only increased to 14 and 12 kPa for Ti–NWM and FeTi–NWM, respectively, at the end of the test, only slightly higher than the initial transmembrane pressure 9 kPa. This lower pressure change is ascribed to the photocatalytic degradation of HA by both membranes. Given that FeTi–NWM has the highest pressure change in the dark but lowest pressure change under solar irradiation, it is a clear indication that FeTi–NWM is a superb anti-fouling membrane when operated under solar irradiation.

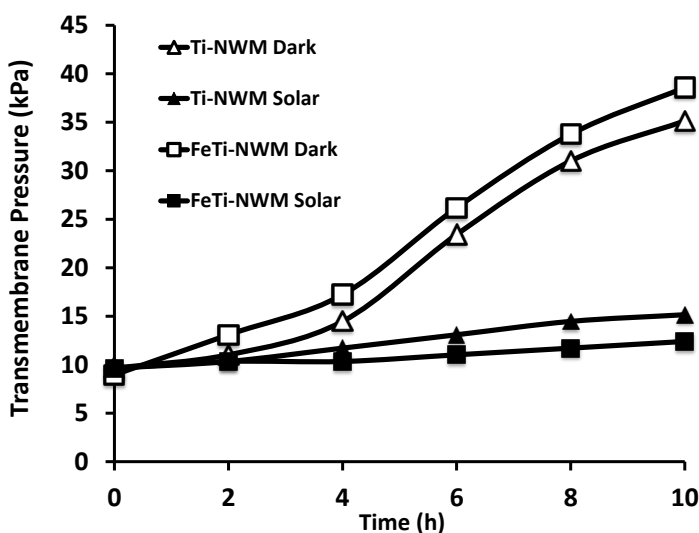


Figure 4.13 Transmembrane pressure across Ti–NWM and FeTi–NWM during the 10 h test in the dark or under solar irradiation.

4.3.4 Proposed mechanism of enhanced HA removal by FeTi-NWM

Figure 4.14 illustrate the possible mechanisms for HA adsorption and photocatalytic

degradation by FeTi–NWM under UV and visible light, respectively. Under UV irradiation (**Figure 4.14a**), electron-hole pairs can be generated on both Fe_2O_3 and TiO_2 [111]. The holes can oxidize water and produce hydroxyl radicals (OH^\bullet) to degrade HA molecules, while the electrons can be scavenged by oxygen to form superoxide anion radicals ($\text{O}_2^{\bullet-}$). The presence of Fe_2O_3 can enhance the adsorption of HA as well. Because the CB edge of Fe_2O_3 is lower than that of TiO_2 and the VB edge of Fe_2O_3 is higher than that of TiO_2 [112], electrons can transfer from TiO_2 CB to Fe_2O_3 CB and holes can transfer from TiO_2 VB to Fe_2O_3 VB. This would actually result in Fe_2O_3 acting as a recombination center and lower the photocatalytic activity, if the amount of TiO_2 in the composite is dominating. However, in this work, we found under solar irradiation (UV-vis) the HA removal was higher than that under visible light alone, indicating a positive contribution of photocatalytic activity from the UV region. It has been reported by Peng et al. [113] that the quantity of Fe_2O_3 coated on TiO_2 may affect transfer of photo-induced charges at the interface of Fe_2O_3 and TiO_2 and they identified a $\text{Fe}_2\text{O}_3/\text{TiO}_2$ mass ratio at 7:3 to be the optimum, at which level the heterojunction promotes charge separation and inhibits charge recombination. It agrees with our result that FeTi–NWM with a $\text{Fe}_2\text{O}_3/\text{TiO}_2$ mass ratio at 1:1 has better performance than those with 1:10 and 2:1 ratios, i.e. too high a TiO_2 concentration may result in Fe_2O_3 being a recombination center while too high a Fe_2O_3 concentration may lower the overall activity since Fe_2O_3 itself is not a good photocatalyst due to fast recombination within Fe_2O_3 [113].

Under visible light irradiation, as shown in **Figure 4.14b**, electron-hole pairs cannot be produced on TiO_2 and only Fe_2O_3 can be activated. A few literature reports suggested that excited CB electrons in Fe_2O_3 can transfer to TiO_2 CB under visible light, leading to

the observed visible light activity [100, 114]. This is doubtful since the CB edge of Fe_2O_3 is about 0.5 eV lower than that of TiO_2 [112]. Here we propose a new model that involves the transfer of Fe_2O_3 CB electrons to the electron trapping sites of anatase TiO_2 . Leytner et al. [115] used time-resolved photoacoustic spectroscopy (TRPAS) and identified the existence of electron trapping sites within anatase TiO_2 that is 0.8 eV below the CB edge of anatase. Gray and coworkers [116, 117] used electron paramagnetic resonance (EPR) spectroscopy to study the charge transfer between the mixed TiO_2 (anatase-rutile) interface, and they found that even though the CB edge of rutile is about 0.2 eV lower than the CB edge of anatase, the electrons can actually transfer from rutile CB to the electron trapping sites within anatase. This is possible considering that those trapping sites have energetics 0.8 eV lower than the anatase CB. Similarly, in this work it is feasible for excited electrons in Fe_2O_3 CB to transfer to the trapping sites of anatase TiO_2 as the Fe_2O_3 CB edge is about 0.3 eV higher than those trapping sites in TiO_2 . In this case, the photoexcited electron-hole pairs are separated; the oxidation occurs at the Fe_2O_3 site and the reduction occurs at the TiO_2 site, which explains the FeTi-NWM's excellent photocatalytic activity under visible light.

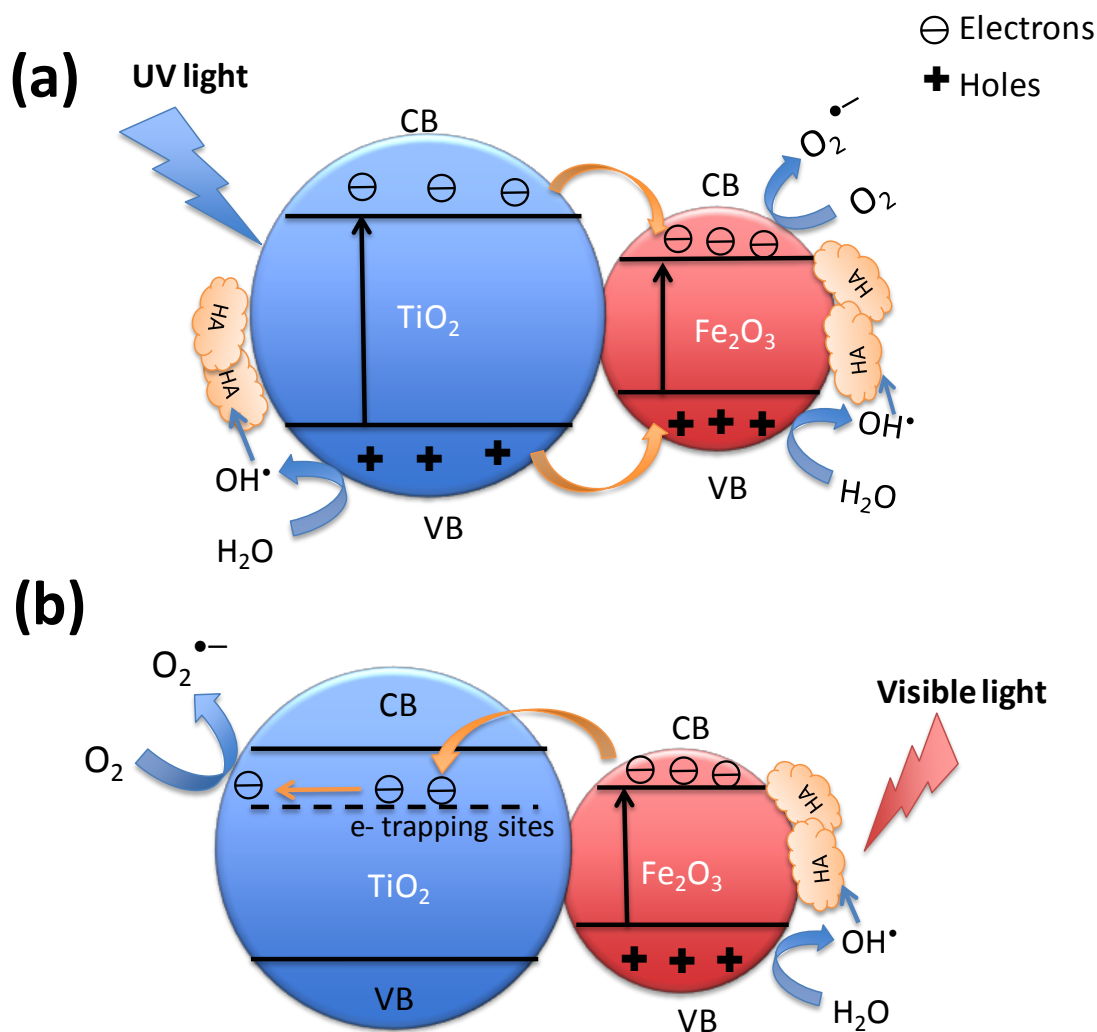


Figure 4.14 Proposed mechanism for the photocatalytic degradation of humic acid (HA) on FeTi-NWM under UV light (a) and visible light (b), respectively.

4.4 Conclusions

A hybrid Fe₂O₃/TiO₂ nanowire membrane (FeTi-NWM) was synthesized in this work, which demonstrated high HA removal and excellent anti-fouling capability. The FeTi-NWM showed higher HA removal under all conditions (in the dark, under visible light and solar light irradiation) compared with Ti-NWM without Fe₂O₃ nanowires. In the 2 h test, almost complete HA removal has been achieved using the FeTi-NWM under solar irradiation. In the longer-term test, the FeTi-NWM also showed 98% removal of HA for 12 h when an extremely high HA concentration was used, and there was

minimum transmembrane pressure increase. Both the strong HA adsorption capability and the high photocatalytic activity responsive to visible light by the Fe_2O_3 nanowires have contributed to the improved HA removal by the FeTi–NWM. The enhanced interfacial charge transfer between Fe_2O_3 and TiO_2 nanowires is believed to result in the observed superb photocatalytic activity.

While the FeTi–NWM is demonstrated promising for antifouling purpose in the bench-scale tests, future work will be conducted to establish the membrane performance under more realistic conditions. For the example, the testing of a complex water quality recipe and the investigation of the effects of solute interference such as turbidity and total dissolved solids in a crossflow membrane apparatus are necessary. Future work will also aim to treat other water sources with high concentrations of organics such as industrial wastewater effluent and produced water. The antibacterial capability of the membrane is another area to be examined in the future, which could be beneficial if it can be used to remove pathogens and prevent biofouling.

Chapter 5 Summary Of Research Work

5.1 Summary of Research Work

1. Visible light Responsive Iodine-doped TiO₂ for Photocatalytic Reduction of CO₂ to Fuels

Iodine-doped titanium oxide (I-TiO₂) nanoparticles that are photocatalytically responsive to visible light illumination have been synthesized by hydrothermal method. The structure and properties of I-TiO₂ nanocrystals prepared with different iodine doping levels and/or calcination temperatures were characterized by X-ray diffraction, transmission electron microscopy and diffraction, X-ray photoelectron spectroscopy, and UV–vis diffuse reflectance spectra. The three nominal iodine dopant levels (5, 10, 15 wt.%) and the two lower calcination temperatures (375, 450 °C) produced mixture of anatase and brookite nanocrystals, with small fraction of rutile found at 550 °C. The anatase phase of TiO₂ increased in volume fraction with increased calcination temperature and iodine levels. The photocatalytic activities of the I-TiO₂ powders were investigated by photocatalytic reduction of CO₂ with H₂O under visible light ($\lambda > 400$ nm) and also under UV–vis illumination. CO was found to be the major photoreduction product using both undoped and doped TiO₂. A high CO₂ reduction activity was observed for I-TiO₂ catalysts (highest CO yield equivalent to 2.4 $\mu\text{mol g}^{-1} \text{h}^{-1}$) under visible light, and they also had much higher CO₂ photoreduction efficiency than undoped TiO₂ under UV–vis irradiation. I-TiO₂ calcined at 375 °C has superior activity to those calcined at higher temperatures. Optimal doping levels of iodine were identified under visible and UV–vis irradiations, respectively. This is the first study that investigates nonmetal doped TiO₂ without other co-catalysts for CO₂ photoreduction

to fuels under visible light.

2. Copper and Iodine Co-modified TiO₂ Nanoparticles for Improved Activity of CO₂ Photoreduction with Water Vapor

Copper and iodine co-modified TiO₂ nanoparticles (Cu–I–TiO₂) were synthesized through a combined hydrothermal and wet-impregnation process. The structures and properties of the catalysts were characterized by XRD, BET, SEM/EDX, XPS, and UV–vis diffuse reflectance spectroscopy. Iodine ions were doped in the TiO₂ lattice by replacing Ti⁴⁺ and, consequently, Ti³⁺ was generated to balance the charge. Iodine doping reduced the TiO₂ crystal size and was responsible for visible light absorption. Cu species were found to deposit on the surface of TiO₂ and resulted in a slightly increased particle size. The activity of the Cu–I–TiO₂ catalyst was investigated by the photocatalytic reduction of CO₂ with water vapor, and CO was found to be the major reduction product with trace amounts of CH₄ generated. Under UV–vis irradiation, the activity of the co-modified catalyst (Cu–I–TiO₂) was higher than that of the single ion-modified catalysts (Cu–TiO₂ or I–TiO₂). Under visible light irradiation, the addition of Cu to I–TiO₂ did not lead to significant improvements in CO₂ reduction. Methyl chloride (CH₃Cl) was detected as a reaction product when CuCl₂ was used as the precursor in the synthesis, thus suggesting that methyl radicals are reaction intermediates. When CuCl₂ was used as the Cu precursor, a three-fold increase in CO₂ photoreduction activity was observed, as compared to when Cu(NO₃)₂ was used as the Cu precursor. These differences in activities were probably due to enhanced Cu dispersion and the hole-scavenging effects of the Cl ions. However, the formation of by-products (e.g., CH₃Cl) may be undesirable.

3. Novel anti-fouling Fe₂O₃/TiO₂ nanowire membranes for humic acid removal from water

Membrane fouling is one of the major obstacles inhibiting the wide application of membrane technologies for water treatment. Membranes with surface modification of titanium dioxide (TiO_2) nanoparticles or TiO_2 nanowire membranes (Ti-NWM) have demonstrated reduced membrane fouling due to the photocatalytic capability of TiO_2 in degrading foulants on the membrane surface. However, the wide band gap of TiO_2 makes it only absorb ultraviolet light, which limits its applications under solar irradiation. In this study, a novel membrane made of interwoven iron oxide (Fe_2O_3) nanowires and TiO_2 nanowires (FeTi-NWM) has demonstrated superior anti-fouling capability in removing humic acid (HA) from water. Results showed that under simulated solar irradiation the FeTi-NWM achieved nearly complete HA removal during a 2 h short-term test at an initial HA concentration of 200 mg/L, compared with 89% HA removal by Ti-NWM. During a 12 h long-term test, the FeTi-NWM maintained 98% HA removal, while the Ti-NWM showed only 55% removal at the end. Without solar irradiation, the FeTi-NWM was severely contaminated and by contrast, a clean surface was maintained under solar irradiation after the 12 h test and the transmembrane pressure change was minimal. The improved HA removal by FeTi-NWM compared with Ti-NWM and its excellent anti-fouling capability under solar irradiation can be attributed to (1) the enhanced HA absorption by Fe_2O_3 nanowires and (2) the formed $\text{Fe}_2\text{O}_3/\text{TiO}_2$ heterojunctions that increase photo-induced charge transfer and improve visible light activity.

Chapter 6 Instrumental Analysis

UV-vis reflectance spectra:

Ultraviolet-visible spectrophotometry (UV-Vis) refers to absorption spectroscopy or reflectance spectroscopy in the ultraviolet-visible spectral region. This means it uses light in the visible and adjacent (near-UV and near-infrared) ranges. The absorption or reflectance in the visible range directly affects the perceived color of the chemicals involved. In this region of the electromagnetic spectrum, molecules undergo electronic transitions.

The UV-vis reflectance spectra were recorded with a UV-vis spectrophotometer (Ocean Optics) using BaSO₄ as the background. The reflectance was converted to F(R) using the Kubelka-Munk (K-M) function $[F(R) = (1-R)^2/2R]$, and the band gap energy was obtained from the plot of $[F(R)E_{ph}]^{1/2}$ against the photon energy E_{ph} .

X-ray Diffraction:

X-ray diffraction is the primary method for determining the phase and the crystalline structure.

The crystal structures of the powder catalysts were identified by X-ray diffraction (XRD) (Scintag XDS 2000) using Cu K α irradiation at 45 kV and a diffracted beam monochromator operated at 40 mA in the setting 2θ range at a scan rate of 1°/min. The crystal size of different crystal phases for TiO₂ was calculated by the Scherrer equation. The fractional phase content, W_A , W_B , and W_R , for anatase, brookite, and rutile, respectively, are mathematically defined in Equations (1), (2) and (3)

$$W_A = \frac{0.886 \times A_A}{(0.886 \times A_A + A_R + 2.721 \times A_B)} \quad (1)$$

$$W_B = \frac{2.721 \times A_B}{(0.886 \times A_A + A_R + 2.721 \times A_B)} \quad (2)$$

$$W_R = \frac{A_R}{(0.886 \times A_A + A_R + 2.721 \times A_B)} \quad (3)$$

where A_A , A_B and A_R represent the integrated intensity of the anatase (1 0 1) peak ($2\theta=25.28^\circ$), the brookite (1 2 1) peak ($2\theta=30.81^\circ$), and the rutile (1 1 0) peak ($2\theta=27.45^\circ$), respectively. Because the brookite (1 2 0) ($2\theta=25.34^\circ$) and brookite (1 1 1) ($2\theta=25.69^\circ$) peaks overlap with the anatase (1 0 1) peak, A_A and A_B were calculated by the following method. Using the single isolated brookite (1 2 1) peak as a reference, the anatase (1 0 1), brookite (1 2 0) and brookite (1 1 1) overlapped peaks were deconvoluted by 0.9 and 0.8 intensity ratio for $I_{(\text{brookite})}^{(121)}/I_{(\text{brookite})}^{(120)}$ and $I_{(\text{brookite})}^{(111)}/I_{(\text{brookite})}^{(120)}$ respectively, with the same full width at half maximum (FWHM) of brookite (1 2 1).

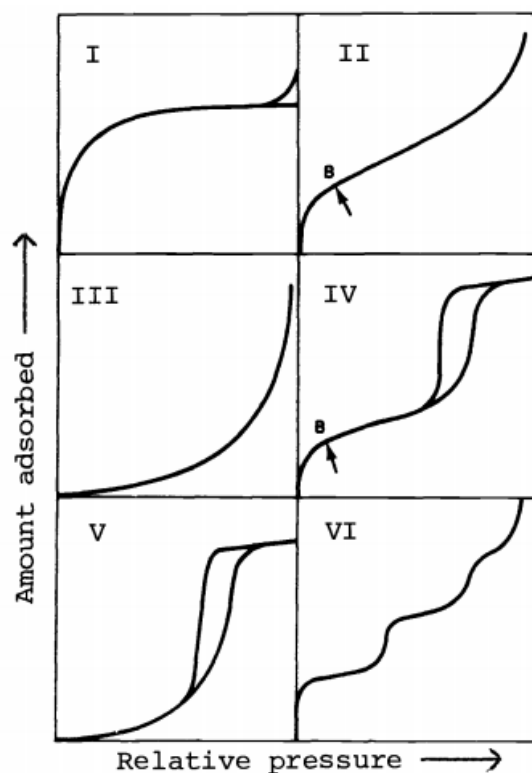
The crystallite size of anatase, brookite and rutile phase TiO_2 was calculated by Scherrer equation: $D = 0.9\lambda/\beta \cos \theta$, where D is the average of crystallite size, λ is the X-ray wavelength used, β is the angular line width of half maximum intensity, and θ is the Bragg's angle in degrees.

BET Analysis:

The Brunauer, Emmett and Teller (BET) technique is the most common method for determining the surface area of powders and porous materials. Nitrogen gas is generally employed as the probe molecule and is exposed to a solid under investigation at liquid nitrogen conditions (i.e. 77 K).

Most analysis of adsorption equilibrium begins with the classification of the isotherms. In 1985, the IUPAC developed a standard classification that consisted of size

general isotherm types shown in the figure as follows. These isotherms included five classical isotherm shapes, plus a sixth that involved steps.



Type I isotherms are given by microporous solids having relatively small external surfaces (e.g. activated carbons, molecular sieve zeolites and certain porous oxides), the limiting uptake being governed by the accessible micropore volume rather than by the internal surface area.

The Type II isotherm represents unrestricted monolayer-multilayer adsorption.

The Type III: isotherms of this type are not common; the best known examples are found with water vapor adsorption on pure non-porous carbons.

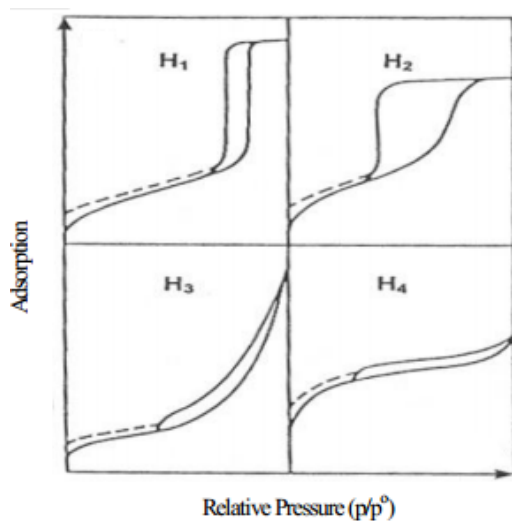
Characteristic features of the Type IV isotherm are its hysteresis loop, which is associated with capillary condensation taking place in mesopores, and the limiting uptake over a range of high P/P_0 . The initial part of the Type IV isotherm is attributed to

monolayer-multilayer adsorption since it follows the same path as the corresponding part of a Type II non-porous form. Type IV are given by many mesoporous industrial adsorbents.

The Type V isotherms is uncommon; it is related to the Type III isotherm in that adsorbent-adsorbate interaction is weak, but is obtained with certain porous adsorbents.

The Type VI isotherm represents stepwise multilayer adsorption on a uniform non-porous surface. The step-height now represents the monolayer capacity for each adsorbed layer and, in the simplest case, remains nearly constant for two or three adsorbed layers.

Very recently, these hysteresis loops have been classified in a way similar to the IUPAC adsorption isotherm schemes shown in the following figure.



The Brunauer-Emmett-Teller (BET) specific surface area and pore size of the catalysts were measured by nitrogen adsorption-desorption isotherms using a Micrometrics ASAP 2020 Surface Area and Porosity Analyzer.

Reference

- [1] Climate change 2014: Impacts, Adaptions, and Vulnerablility Intergovmental panel on climate change (IPCC), (2014).
- [2] US GHG inventory 2015 Executive Summary
- [3] M.N.y.N. Johan, CONTROLLING POWER PLANT CO2 EMISSIONS: A LONG RANGE VIEW, (2000).
- [4] S.P. Bindra, W. Abosh, Recent developments in water desalination, *Desalination* 136 (2001) 49-56.
- [5] N. Ghaffour, T.M. Missimer, G.L. Amy, Technical review and evaluation of the economics of water desalination: Current and future challenges for better water supply sustainability, *Desalination* 309 (2013) 197-207.
- [6] X. Zhang, A.J. Du, P. Lee, D.D. Sun, J.O. Leckie, TiO₂ nanowire membrane for concurrent filtration and photocatalytic oxidation of humic acid in water, *Journal of Membrane Science* 313 (2008) 44-51.
- [7] Q. Zhang, Y. Li, E.A. Ackerman, M. Gajdardziska-Josifovska, H. Li, Visible light responsive iodine-doped TiO₂ for photocatalytic reduction of CO₂ to fuels, *Applied Catalysis A: General* 400 (2011) 195-202.
- [8] M.M. Pendergast, E.M.V. Hoek, A review of water treatment membrane nanotechnologies, *Energ Environ Sci* 4 (2011) 1946-1971.
- [9] B. van der Bruggen, J.Q.J.C. Verberk, J. Verhack, Comparison of pressure-driven membrane processes and traditional processes for drinking water production in Europe based on specific impact criteria, *Water Sa* 30 (2004) 413-419.
- [10] B. Van der Bruggen, C. Vandecasteele, T. Van Gestel, W. Doyen, R. Leysen, A review of pressure-driven membrane processes in wastewater treatment and drinking water production, *Environ Prog* 22 (2003) 46-56.
- [11] M. Bodzek, K. Konieczny, A. Kwiecinska, Application of membrane processes in drinking water treatment-state of art, *Desalin Water Treat* 35 (2011) 164-184.
- [12] W. Gao, H. Liang, J. Ma, M. Han, Z.L. Chen, Z.S. Han, G.B. Li, Membrane fouling control in ultrafiltration technology for drinking water production: A review, *Desalination* 272 (2011) 1-8.
- [13] W.S. Guo, H.H. Ngo, J.X. Li, A mini-review on membrane fouling, *Bioresource Technol* 122 (2012) 27-34.
- [14] M.F. Kato S, Titanium dioxide-photocatalyzed oxidation. I. Tianium dioxide-photocatalyzed liquid phase oxidation of tetralin., *Kogyo Kagaku Zasshi* 67 (1964) 42-50.
- [15] R.M. McLintock S, Reactions on titanium dioxide; photo- adsorption and oxidation of ethylene and propylene, *Trans Faraday Soc* 61 (1965) 1007-1016.
- [16] H.K. Fujishima A, Electrochemical photolysis of water at a semiconductor electrode, *Nature* (1972) 37-38.
- [17] K. Teramura, H. Tsuneoka, T. Shishido, T. Tanaka, Effect of H-2 gas as a reductant on photoreduction of CO₂ over a Ga₂O₃ photocatalyst, *Chemical Physics Letters* 467 (2008) 191-194.
- [18] K. Koci, L. Obalova, L. Matejova, D. Placha, Z. Lacny, J. Jirkovsky, O. Solcova,

Effect of TiO₂ particle size on the photocatalytic reduction of CO₂, *Applied Catalysis B-Environmental* 89 (2009) 494-502.

[19] K. Kočí, K. Matějů, L. Obalová, S. Krejčíková, Z. Lacný, D. Plachá, L. Čapek, A. Hospodková, O. Šolcová, Effect of silver doping on the TiO₂ for photocatalytic reduction of CO₂, *Applied Catalysis B: Environmental* 96 (2010) 239-244.

[20] J. Ma, Z. Xiong, T. David Waite, W.J. Ng, X.S. Zhao, Enhanced inactivation of bacteria with silver-modified mesoporous TiO₂ under weak ultraviolet irradiation, *Microporous and Mesoporous Materials* 144 (2011) 97-104.

[21] D. Chatterjee, A. Mahata, Photoassisted detoxification of organic pollutants on the surface modified TiO₂ semiconductor particulate system, *Catalysis Communications* 2 (2001) 1-3.

[22] Y.-H. Hsien, C.-F. Chang, Y.-H. Chen, S. Cheng, Photodegradation of aromatic pollutants in water over TiO₂ supported on molecular sieves, *Applied Catalysis B: Environmental* 31 (2001) 241-249.

[23] P. Pichat, Some views about indoor air photocatalytic treatment using TiO₂: Conceptualization of humidity effects, active oxygen species, problem of CO, SO₂ carbonyl pollutants, *Applied Catalysis B: Environmental* 99 (2010) 428-434.

[24] Q. Wang, T. Jin, Z. Hu, L. Zhou, M. Zhou, TiO₂-NTs/SnO₂-Sb anode for efficient electrocatalytic degradation of organic pollutants: Effect of TiO₂-NTs architecture, *Separation and Purification Technology* 102 (2013) 180-186.

[25] Y. Hu, H.L. Tsai, C.L. Huang, Effect of brookite phase on the anatase, rutile transition in titania nanoparticles, *Journal of the European Ceramic Society* 23 (2003) 691-696.

[26] X. Wang, H. He, Y. Chen, J. Zhao, X. Zhang, Anatase TiO₂ hollow microspheres with exposed {100} facets: Facile synthesis and enhanced photocatalysis, *Applied Surface Science* 258 (2012) 5863-5868.

[27] W.Q. Wu, B.X. Lei, H.S. Rao, Y.F. Xu, Y.F. Wang, C.Y. Su, D.B. Kuang, Hydrothermal Fabrication of Hierarchically Anatase TiO₂ Nanowire arrays on FTO Glass for Dye-sensitized Solar Cells, *Sci Rep-Uk* 3 (2013).

[28] R. Long, Y. Dai, B. Huang, Structural and electronic properties of iodine-doped anatase and rutile TiO₂, *Computational Materials Science* 45 (2009) 223-228.

[29] S. Gupta, M. Tripathi, A review of TiO₂ nanoparticles, *Chin. Sci. Bull.* 56 (2011) 1639-1657.

[30] J. Muscat, V. Swamy, N.M. Harrison, First-principles calculations of the phase stability of TiO₂, *Phys Rev B* 65 (2002).

[31] N.L. Wu, M.S. Lee, Enhanced TiO₂ photocatalysis by Cu in hydrogen production from aqueous methanol solution, *International Journal of Hydrogen Energy* 29 (2004) 1601-1605.

[32] <http://ruby.colorado.edu/~smyth/min/tio2.html>.

[33] J. Ding, Y. Yuan, J. Xu, J. Deng, J. Guo, TiO₂ Nanopowder Co-Doped with Iodine and Boron to Enhance Visible-Light Photocatalytic Activity, *Journal of Biomedical Nanotechnology* 5 (2009) 521-527.

[34] S. Pavasupree, Y. Suzuki, S. Yoshikawa, R. Kawahata, Synthesis of titanate, TiO₂ (B), and anatase TiO₂ nanofibers from natural rutile sand, *Journal of Solid State Chemistry* 178 (2005) 3110-3116.

[35] L. Cui, K.N. Hui, K.S. Hui, S.K. Lee, W. Zhou, Z.P. Wan, C.-N.H. Thuc, Facile

- microwave-assisted hydrothermal synthesis of TiO₂ nanotubes, *Materials Letters* 75 (2012) 175-178.
- [36] A. Jitianu, T. Cacciaguerra, R. Benoit, S. Delpeux, F. B. Guin, S. Bonnamy, Synthesis and characterization of carbon nanotubes/TiO₂ nanocomposites, *Carbon* 42 (2004) 1147-1151.
- [37] Q. Wu, J. Ouyang, K. Xie, L. Sun, M. Wang, C. Lin, Ultrasound-assisted synthesis and visible-light-driven photocatalytic activity of Fe-incorporated TiO₂ nanotube array photocatalysts, *Journal of Hazardous Materials* 199, 200 (2012) 410-417.
- [38] H. Jiang, T. Wang, L. Wang, C. Sun, T. Jiang, G. Cheng, S. Wang, Development of an amorphous mesoporous TiO₂ nanosphere as a novel carrier for poorly water-soluble drugs: Effect of different crystal forms of TiO₂ carriers on drug loading and release behaviors, *Microporous and Mesoporous Materials* 153 (2012) 124-130.
- [39] Y. Wang, D. Yang, Y. Shi, Z. Jiang, Bio-inspired synthesis of TiO₂ hollow nanospheres in agarose gels, *Journal of Alloys and Compounds* 560 (2013) 42-48.
- [40] Y. Lin, Photocatalytic activity of TiO₂ nanowire arrays, *Materials Letters* 62 (2008) 1246-1248.
- [41] Y. Liu, H. Wang, H. Li, W. Zhao, C. Liang, H. Huang, Y. Deng, H. Shen, Length-controlled synthesis of oriented single-crystal rutile TiO₂ nanowire arrays, *Journal of Colloid and Interface Science* 363 (2011) 504-510.
- [42] F. Guo, X. Su, G. Hou, Z. Liu, Z. Mei, Fabrication of superhydrophobic TiO₂ surface with cactus-like structure by a facile hydrothermal approach, *Colloids and Surfaces A: Physicochemical and Engineering Aspects* 395 (2012) 70-74.
- [43] A. Hu, X. Zhang, K.D. Oakes, P. Peng, Y.N. Zhou, M.R. Servos, Hydrothermal growth of free standing TiO₂ nanowire membranes for photocatalytic degradation of pharmaceuticals, *Journal of Hazardous Materials* 189 (2011) 278-285.
- [44] Z. Li, Y. Fang, X. Zhan, S. Xu, Facile preparation of squarylium dye sensitized TiO₂ nanoparticles and their enhanced visible-light photocatalytic activity, *Journal of Alloys and Compounds* 564 (2013) 138-142.
- [45] Y.Q. Cong, Z. Li, Y. Zhang, Q. Wang, Q. Xu, Synthesis of alpha-Fe₂O₃/TiO₂ nanotube arrays for photoelectro-Fenton degradation of phenol, *Chem Eng J* 191 (2012) 356-363.
- [46] S.K. Mohapatra, S. Banerjee, M. Misra, Synthesis of Fe₂O₃/TiO₂ nanorod-nanotube arrays by filling TiO₂ nanotubes with Fe, *Nanotechnology* 19 (2008).
- [47] M.G. Nair, M. Nirmala, K. Rekha, A. Anukaliani, Structural, optical, photo catalytic and antibacterial activity of ZnO and Co doped ZnO nanoparticles, *Materials Letters* 65 (2011) 1797-1800.
- [48] Z. Wang, P. Xiao, L. Qiao, X. Meng, Y. Zhang, X. Li, F. Yang, Polypyrrole sensitized ZnO nanorod arrays for efficient photo-electrochemical splitting of water, *Physica B: Condensed Matter*.
- [49] C.-F. Yen, M.-K. Lee, Low equivalent oxide thickness of TiO₂/GaAs MOS capacitor, *Solid-State Electronics* 73 (2012) 56-59.
- [50] A.H. Fakeeha, A.S.A. Al-Fatesh, A.E. Abasaheed, Modification of alumina support with TiO₂-P25 in CO₂ reforming of CH₄, *Journal of Industrial and Engineering Chemistry* 18 (2012) 212-217.
- [51] J. Arenas-Alatorre, S. Rojas, R. Mariscal, J.L.G. Fierro, G. Diaz, SCR of NO by CH₄ on Pt/ZrO₂/TiO₂ sol-gel catalysts, *Catalysis Today* 107, 108 (2005) 149-

156.

- [52] Z.Y. Wang, H.C. Chou, J.C.S. Wu, D.P. Tsai, G. Mul, CO₂ photoreduction using NiO/InTaO₄ in optical-fiber reactor for renewable energy, *Applied Catalysis a-General* 380 (2010) 172-177.
- [53] J.C.S. Wu, H.M. Lin, C.L. Lai, Photo reduction of CO₂ to methanol using optical-fiber photoreactor, *Applied Catalysis a-General* 296 (2005) 194-200.
- [54] C.C. Lo, C.H. Hung, C.S. Yuan, J.F. Wu, Photoreduction of carbon dioxide with H₂ and H₂O over TiO₂ and ZrO₂ in a circulated photocatalytic reactor, *Solar Energy Materials and Solar Cells* 91 (2007) 1765-1774.
- [55] K. Teramura, T. Tanaka, H. Ishikawa, Y. Kohno, T. Funabiki, Photocatalytic reduction of CO₂ to CO in the presence of H₂ or CH₄ as a reductant over MgO, *Journal of Physical Chemistry B* 108 (2004) 346-354.
- [56] D.-L. Shieh, C.-H. Ho, J.-L. Lin, Study of preparation of mesoporous TiO₂-B nanofibers from mesoporous anatase TiO₂ and interaction between CH₃I and TiO₂-B, *Microporous and Mesoporous Materials* 109 (2008) 362-369.
- [57] T. Hirose, Y. Maeno, Y. Himeda, Photocatalytic carbon dioxide photoreduction by Co(bpy)(3)(2+) sensitized by Ru(bpy)(3)(2+) fixed to cation exchange polymer, *Journal of Molecular Catalysis a-Chemical* 193 (2003) 27-32.
- [58] B. Xin, P. Wang, D. Ding, J. Liu, Z. Ren, H. Fu, Effect of surface species on Cu-TiO₂ photocatalytic activity, *Applied Surface Science* 254 (2008) 2569-2574.
- [59] W. Simka, A. Iwaniak, G. Nawrat, A. Maciej, J. Michalska, K. Radwański, J. Gazdowicz, Modification of titanium oxide layer by calcium and phosphorus, *Electrochimica Acta* 54 (2009) 6983-6988.
- [60] K. Song, J. Zhou, J. Bao, Y. Feng, Photocatalytic Activity of (Copper, Nitrogen)-Codoped Titanium Dioxide Nanoparticles, *Journal of the American Ceramic Society* 91 (2008) 1369-1371.
- [61] I.H. Tseng, W.C. Chang, J.C.S. Wu, Photoreduction of CO₂ using sol-gel derived titania and titania-supported copper catalysts, *Applied Catalysis B: Environmental* 37 (2002) 37-48.
- [62] Y. Li, W.-N. Wang, Z. Zhan, M.-H. Woo, C.-Y. Wu, P. Biswas, Photocatalytic reduction of CO₂ with H₂O on mesoporous silica supported Cu/TiO₂ catalysts, *Applied Catalysis B: Environmental* 100 (2010) 386-392.
- [63] N. Sasirekha, S.J.S. Basha, K. Shanthi, Photocatalytic performance of Ru doped anatase mounted on silica for reduction of carbon dioxide, *Applied Catalysis B-Environmental* 62 (2006) 169-180.
- [64] R. Dholam, N. Patel, M. Adami, A. Miotello, Hydrogen production by photocatalytic water-splitting using Cr- or Fe-doped TiO₂ composite thin films photocatalyst, *International Journal of Hydrogen Energy* 34 (2009) 5337-5346.
- [65] G.S. Wu, J.L. Wen, J.P. Wang, D.F. Thomas, A.C. Chen, A facile approach to synthesize N and B co-doped TiO₂ nanomaterials with superior visible-light response, *Materials Letters* 64 (2010) 1728-1731.
- [66] M. Pelaez, A.A. de la Cruz, E. Stathatos, P. Falaras, D.D. Dionysiou, Visible light-activated N-F-codoped TiO₂ nanoparticles for the photocatalytic degradation of microcystin-LR in water, *Catalysis Today* 144 (2009) 19-25.
- [67] M. Hamadanian, A. Reisi-Vanani, A. Majedi, Preparation and characterization of S-doped TiO₂ nanoparticles, effect of calcination temperature and evaluation of

- photocatalytic activity, *Materials Chemistry and Physics* 116 (2009) 376-382.
- [68] G. Liu, C. Sun, X. Yan, L. Cheng, Z. Chen, X. Wang, L. Wang, S.C. Smith, G.Q. Lu, H.-M. Cheng, Iodine doped anatase TiO₂ photocatalyst with ultra-long visible light response: correlation between geometric/electronic structures and mechanisms, *Journal of Materials Chemistry* 19 (2009) 2822-2829.
- [69] S. Tojo, T. Tachikawa, M. Fujitsuka, T. Majima, Iodine-doped TiO₂ photocatalysts: Correlation between band structure and mechanism, *Journal of Physical Chemistry C* 112 (2008) 14948-14954.
- [70] L. Zhou, J. Deng, Y. Zhao, W. Liu, L. An, F. Chen, Preparation and characterization of N-I co-doped nanocrystal anatase TiO₂ with enhanced photocatalytic activity under visible-light irradiation, *Materials Chemistry and Physics* 117 (2009) 522-527.
- [71] W. Su, Y. Zhang, Z. Li, L. Wu, X. Wang, J. Li, X. Fu, Multivalency iodine doped TiO₂: Preparation, characterization, theoretical studies, and visible-light photocatalysis, *Langmuir* 24 (2008) 3422-3428.
- [72] T.J. LaTempa, S. Rani, N.Z. Bao, C.A. Grimes, Generation of fuel from CO₂ saturated liquids using a p-Si nanowire parallel to n-TiO₂ nanotube array photoelectrochemical cell, *Nanoscale* 4 (2012) 2245-2250.
- [73] O. Ozcan, F. Yukruk, E.U. Akkaya, D. Uner, Dye sensitized CO₂ reduction over pure and platinized TiO₂, *Top Catal* 44 (2007) 523-528.
- [74] Y.-h. Xu, D.-h. Liang, M.-l. Liu, D.-z. Liu, Preparation and characterization of Cu₂O, ÆTiO₂: Efficient photocatalytic degradation of methylene blue, *Materials Research Bulletin* 43 (2008) 3474-3482.
- [75] M. Anpo, H. Yamashita, K. Ikeue, Y. Fujii, S.G. Zhang, Y. Ichihashi, D.R. Park, Y. Suzuki, K. Koyano, T. Tatsumi, Photocatalytic reduction of CO₂ with H₂O on Ti-MCM-41 and Ti-MCM-48 mesoporous zeolite catalysts, *Catalysis Today* 44 (1998) 327-332.
- [76] X. Nie, S. Zhuo, G. Maeng, K. Sohlberg, Doping of TiO₂ Polymorphs for Altered Optical and Photocatalytic Properties, 2009.
- [77] Q. Zhang, Y. Li, E.A. Ackerman, M. Gajdardziska-Josifovska, H. Li, Visible light responsive iodine-doped TiO₂ for photocatalytic reduction of CO₂ to fuels, *Applied Catalysis A: General* 400 (2011) 195-202.
- [78] M. Hamadianian, A. Reisi-Vanani, A. Majedi, Synthesis, characterization and effect of calcination temperature on phase transformation and photocatalytic activity of Cu,S-codoped TiO₂ nanoparticles, *Applied Surface Science* 256 (2010) 1837-1844.
- [79] Y. Su, Y. Xiao, Y. Li, Y. Du, Y. Zhang, Preparation, photocatalytic performance and electronic structures of visible-light-driven Fe-N-codoped TiO₂ nanoparticles, *Materials Chemistry and Physics* 126 (2011) 761-768.
- [80] S. Song, F. Hong, Z. He, H. Wang, X. Xu, J. Chen, Influence of zirconium doping on the activities of zirconium and iodine co-doped titanium dioxide in the decolorization of methyl orange under visible light irradiation, *Applied Surface Science* 257 (2011) 10101-10108.
- [81] O.K. Varghese, M. Paulose, T.J. LaTempa, C.A. Grimes, High-Rate Solar Photocatalytic Conversion of CO₂ and Water Vapor to Hydrocarbon Fuels, *Nano Letters* 9 (2009) 731-737.
- [82] L. Li, H. Zhuang, D. Bu, Characterization and activity of visible-light-driven TiO(2) photocatalyst codoped with lanthanum and iodine, *Applied Surface Science* 257 (2011) 9221-9225.

- [83] K. Lalitha, G. Sadanandam, V.D. Kumari, M. Subrahmanyam, B. Sreedhar, N.Y. Hebalkar, Highly Stabilized and Finely Dispersed Cu₂O/TiO₂: A Promising Visible Sensitive Photocatalyst for Continuous Production of Hydrogen from Glycerol:Water Mixtures, *The Journal of Physical Chemistry C* 114 (2010) 22181-22189.
- [84] L. Zhou, J. Deng, Y. Zhao, W. Liu, L. An, F. Chen, Preparation and characterization of N-I co-doped nanocrystal anatase TiO₂ with enhanced photocatalytic activity under visible-light irradiation, *Materials Chemistry and Physics* 117 (2009) 522-527.
- [85] Slamet, H.W. Nasution, E. Purnama, S. Kosela, J. Gunlazuardi, Photocatalytic reduction of CO₂ on copper-doped Titania catalysts prepared by improved-impregnation method, *Catalysis Communications* 6 (2005) 313-319.
- [86] I.H. Tseng, W.C. Chang, J.C.S. Wu, Photoreduction of CO₂ using sol-gel derived titania and titania-supported copper catalysts, *Applied Catalysis B-Environmental* 37 (2002) 37-48.
- [87] A.M. Hu, X. Zhang, K.D. Oakes, P. Peng, Y.N. Zhou, M.R. Servos, Hydrothermal growth of free standing TiO₂ nanowire membranes for photocatalytic degradation of pharmaceuticals, *Journal of Hazardous Materials* 189 (2011) 278-285.
- [88] X.W. Zhang, A.J. Du, P.F. Lee, D.D. Sun, J.O. Leckie, TiO₂ nanowire membrane for concurrent filtration and photocatalytic oxidation of humic acid in water, *Journal of Membrane Science* 313 (2008) 44-51.
- [89] S. Rengaraj, X.Z. Li, Enhanced photocatalytic activity of TiO₂ by doping with Ag for degradation of 2,4,6-trichlorophenol in aqueous suspension, *Journal of Molecular Catalysis a-Chemical* 243 (2006) 60-67.
- [90] M.B. Kaynar, R. DelPercio, E. Yassitepe, S. Ozcan, S.I. Shah, Solvent free fabrication of nanoporous TiO₂ filters using organic-inorganic nanocomposites, *Powder Technology* 233 (2013) 331-334.
- [91] Y. Li, W. Wang, X. Qiu, L. Song, H.M. Meyer Iii, M.P. Paranthaman, G. Eres, Z. Zhang, B. Gu, Comparing Cr, and N only doping with (Cr, N)-codoping for enhancing visible light reactivity of TiO₂, *Applied Catalysis B: Environmental* 110 (2011) 148-153.
- [92] L.J. Liu, Y. Li, Understanding the Reaction Mechanism of Photocatalytic Reduction of CO₂ with H₂O on TiO₂-Based Photocatalysts: A Review, *Aerosol Air Qual. Res.* 14 (2014) 453-469.
- [93] L.G. Devi, R. Kavitha, Review on modified N-TiO₂ for green energy applications under UV/visible light: selected results and reaction mechanisms, *Rsc Adv* 4 (2014) 28265-28299.
- [94] Q.Y. Zhang, Y. Li, E.A. Ackerman, M. Gajdardziska-Josifovska, H.L. Li, Visible light responsive iodine-doped TiO₂ for photocatalytic reduction of CO₂ to fuels, *Applied Catalysis a-General* 400 (2011) 195-202.
- [95] W. Zhou, H.G. Fu, Mesoporous TiO₂: Preparation, Doping, and as a Composite for Photocatalysis, *ChemCatChem* 5 (2013) 885-894.
- [96] R. Dagher, P. Drogui, D. Robert, Modified TiO₂ For Environmental Photocatalytic Applications: A Review, *Ind. Eng. Chem. Res.* 52 (2013) 3581-3599.
- [97] J. Wang, D.N. Tafen, J.P. Lewis, Z.L. Hong, A. Manivannan, M.J. Zhi, M. Li, N.Q. Wu, Origin of Photocatalytic Activity of Nitrogen-Doped TiO₂ Nanobelts, *J Am Chem Soc* 131 (2009) 12290-12297.
- [98] A.M. Yu, G.J. Wu, F.X. Zhang, Y.L. Yang, N.J. Guan, Synthesis and Characterization of N-doped TiO₂ Nanowires with Visible Light Response, *Catalysis*

Letters 129 (2009) 507-512.

[99] A. Fujishima, X.T. Zhang, D.A. Tryk, TiO₂ photocatalysis and related surface phenomena, *Surf. Sci. Rep.* 63 (2008) 515-582.

[100] H. Liu, H.K. Shon, X.A. Sun, S. Vigneswaran, H. Nan, Preparation and characterization of visible light responsive Fe₂O₃-TiO₂ composites, *Applied Surface Science* 257 (2011) 5813-5819.

[101] B. Palanisamy, C.M. Babu, B. Sundaravel, S. Anandan, V. Murugesan, Sol-gel synthesis of mesoporous mixed Fe₂O₃/TiO₂ photocatalyst: Application for degradation of 4-chlorophenol, *Journal of Hazardous Materials* 252 (2013) 233-242.

[102] W. Zhou, H.G. Fu, K. Pan, C.G. Tian, Y. Qu, P.P. Lu, C.C. Sun, Mesoporous TiO₂/α-Fe₂O₃: Bifunctional Composites for Effective Elimination of Arsenite Contamination through Simultaneous Photocatalytic Oxidation and Adsorption, *Journal of Physical Chemistry C* 112 (2008) 19584-19589.

[103] Y.F. Zhu, R.G. Du, J. Li, H.Q. Qi, C.J. Lin, Photogenerated Cathodic Protection Properties of a TiO₂ Nanowire Film Prepared by a Hydrothermal Method, *Acta Physico-Chimica Sinica* 26 (2010) 2349-2353.

[104] W. Yuan, A.L. Zydney, Humic acid fouling during microfiltration, *Journal of Membrane Science* 157 (1999) 1-12.

[105] T.K. Ghorai, M. Chakraborty, P. Pramanik, Photocatalytic performance of nano-photocatalyst from TiO₂ and Fe₂O₃ by mechanochemical synthesis, *Journal of Alloys and Compounds* 509 (2011) 8158-8164.

[106] A. Di Paola, G. Cufalo, M. Addamo, M. Bellardita, R. Campostrini, M. Ischia, R. Ceccato, L. Palmisano, Photocatalytic activity of nanocrystalline TiO₂ (brookite, rutile and brookite-based) powders prepared by thermohydrolysis of TiCl₄ in aqueous chloride solutions, *Colloids and Surfaces A: Physicochemical and Engineering Aspects* 317 (2008) 366-376.

[107] M. Bellardita, A. Di Paola, L. Palmisano, F. Parrino, G. Buscarino, R. Amadelli, Preparation and photoactivity of samarium loaded anatase, brookite and rutile catalysts, *Applied Catalysis B: Environmental* 104 (2011) 291-299.

[108] E.K. Kim, H.W. Walker, Effect of cationic polymer additives on the adsorption of humic acid onto iron oxide particles, *Colloids and Surfaces A: Physicochemical and Engineering Aspects* 194 (2001) 123-131.

[109] A.W.P. Vermeer, W.H. van Riemsdijk, L.K. Koopal, Adsorption of humic acid to mineral particles. 1. Specific and electrostatic interactions, *Langmuir* 14 (1998) 2810-2819.

[110] J.-K. Yang, S.-M. Lee, Removal of Cr(VI) and humic acid by using TiO₂ photocatalysis, *Chemosphere* 63 (2006) 1677-1684.

[111] B. Palanisamy, C.M. Babu, B. Sundaravel, S. Anandan, V. Murugesan, Sol-gel synthesis of mesoporous mixed Fe₂O₃/TiO₂ photocatalyst: Application for degradation of 4-chlorophenol, *Journal of Hazardous Materials* 252-253 (2013) 233-242.

[112] M. Gratzel, Photoelectrochemical cells, *Nature* 414 (2001) 338-344.

[113] L.L. Peng, T.F. Xie, Y.C. Lu, H.M. Fan, D.J. Wang, Synthesis, photoelectric properties and photocatalytic activity of the Fe₂O₃/TiO₂ heterogeneous photocatalysts, *Phys Chem Chem Phys* 12 (2010) 8033-8041.

[114] Y.B. Xia, L.W. Yin, Core-shell structured α-Fe₂O₃@TiO₂ nanocomposites with improved photocatalytic activity in the visible light region, *Phys Chem Chem Phys*

15 (2013) 18627-18634.

[115] S. Leytner, J.T. Hupp, Evaluation of the energetics of electron trap states at the nanocrystalline titanium dioxide/aqueous solution interface via time-resolved photoacoustic spectroscopy, *Chemical Physics Letters* 330 (2000) 231-236.

[116] D.C. Hurum, A.G. Agrios, K.A. Gray, T. Rajh, M.C. Thurnauer, Explaining the enhanced photocatalytic activity of Degussa P25 mixed-phase TiO₂ using EPR, *Journal of Physical Chemistry B* 107 (2003) 4545-4549.

[117] D.C. Hurum, A.G. Agrios, S.E. Crist, K.A. Gray, T. Rajh, M.C. Thurnauer, Probing reaction mechanisms in mixed phase TiO₂ by EPR, *J. Electron Spectrosc. Relat. Phenom.* 150 (2006) 155-163.

Curriculum Vitae

Qianyi Zhang

Skills

- **Products research and development:** cooperate with industry to solve problems and develop new products.
 - **New material R&D:** Proficient in popular material synthesis methods such as co-precipitation, sol-gel, solid-state reaction, pyrolysis, and hydrothermal method.
 - **Material characterization and analysis:** XRD, XPS, EDX, FTIR, SEM, HRTEM, HPLC, GC, GC-MS, UV-vis spectrometer, Raman spectrum, BET surface area analysis, TGA analysis, TOC analysis.
 - **Computer skill:** Work, Powerpoint, Excel, Windows, MacOS, Matlab, SPSS, Java, Fortran, HTML5, CSS3
 - **Language:** English, Mandarin
-

Work Experience

2014.5-2014.9 Research and Material Scientist

A.O. Smith, Inc.

Internship

Developed and/or tested water treatment membrane products for varied markets. Engaged in raw material analysis, membrane material formulation, coating material innovation, and quality test development using design-of-experiment methodologies.

- Responsible for independent R&D project: New TiO₂ based material for disinfection.
- New product test and evaluate: Supported and tested new membrane module in reverse osmosis system for different markets (China, India, US) with regulation standards such as HJ/T 270, GB 5749, NSF/ANSI 53, NSF/ANSI 55 and NSF Protocol P231.

2012.9-2014.5 Research Scientist

NSF Water Equipment and Policy Center (WEP)

Pharmaceutical and BPA removal with novel material membrane

- As the leading researcher to design, synthesize and test new nanowire hybrid membrane in water treatment application. Membrane was characterized by multiple methods such as XRD, UV-vis, SEM, EDX. BPA and pharmaceutical degradation efficiency and byproducts were tested by GC/MS, HPLC.

- Responsible for experiment design, test, analysis and experiment report.
- Preparing material for patent application.

2012-2013 Research Assistant

Pentair Inc. & University of Wisconsin-Milwaukee

Anti-fouling TiO₂ nanowire membrane

- Sponsored by Pentair Inc. to develop potential anti-fouling membrane product.
- Cooperated with Pentair researchers to investigate the anti-fouling ability of TiO₂ nanowire membrane.
- Responsible for data collection, data analysis, and the final reports.

2010-2012 Research Assistant

Johnson-Control Inc. & University of Wisconsin-Milwaukee

New LiMn₂O₄ material with pyrolysis method as cathode for Li-ion battery

Novel material development for battery industry. Conducted cyclic voltammetry (CV) test, galvanostatic charge/discharge test, and Electrochemical impedance spectroscopy (EIS) test.

- Novel Li-ion battery material characterization with XPS, XRD, TGA, BET and SEM.
- Trained and cooperated with Johnson-Control battery lab to assemble batteries and test their electrochemical properties.

2009-present Project Assistant, teaching assistant

University of Wisconsin-Milwaukee

Novel material for new energy research

- Future fuel production technology with novel material: investigate CO₂ conversion to fuel with nanomaterial. The data was collected and analyzed with GC, GC-MS, XPS, XRD, UV-vis, SEM, and TEM.
- Research of novel battery materials: TiO₂ coated Fe₂O₃ nanowire as anode for Lithium-ion battery.
- Manage and train multiple instruments such as GC, GC-MS in the lab. As the major assistant to help lab supervisor to setup the brand new UWM nanotech and environmental tech research lab.

Education

Mechanical Engineering

University of Wisconsin, Milwaukee

Milwaukee, WI

- Candidate for Doctor of Engineering, December 2014
- Research & Project Assistant, Teaching Assistant

Biotechnology

Sichuan University

Sichuan, China

- Bachelor of Science in Biotechnology

Awards

Elsevier “Applied Catalyst: A” Top Citation Award (2011-2012)
University of Wisconsin-Milwaukee Annual Poster Competition 2nd Place.
University of Wisconsin-Milwaukee Chancellor Award (2014)
University of Wisconsin-Milwaukee Chancellor Award (2009)

Publication

- (1) Q. Zhang, G. Rao, J. Rogers, C. Zhao, L. Liu, Y. Li, Novel anti-fouling Fe₂O₃/TiO₂ nanowire membranes for humic acid removal from water, *Chemical Engineering Journal* 271 (2015) 180-187.
- (2) Q.Y. Zhang, T.T. Gao, J.M. Andino, Y. Li, Copper and iodine co-modified TiO₂ nanoparticles for improved activity of CO₂ photoreduction with water vapor, *Appl Catal B-Environ* 123 (2012) 257-264.
- (3) Q.Y. Zhang, Y. Li, E.A. Ackerman, M. Gajdardziska-Josifovska, H.L. Li, Visible light responsive iodine-doped TiO₂ for photocatalytic reduction of CO₂ to fuels, *Appl Catal a-Gen* 400 (2011) 195-202.
- (4) J. Guo, H.B. Gu, H.G. Wei, Q.Y. Zhang, N. Haldolaarachchige, Y. Li, D.P. Young, S.Y. Wei, Z.H. Guo, Magnetite-Polypyrrole Metacomposites: Dielectric Properties and Magnetoresistance Behavior, *J Phys Chem C* 117 (2013) 10191-10202.
- (5) L.J. Liu, C.Y. Zhao, H.L. Zhao, Q.Y. Zhang, Y. Li, ZnO-CoO Nanoparticles Encapsulated in 3D Porous Carbon Microspheres for High-performance Lithium-Ion Battery Anodes, *Electrochim Acta* 135 (2014) 224-231.
- (6) C. Zhao, L. Liu, Q. Zhang, J. Rogers, H. Zhao, Y. Li, Synthesis of Carbon-TiO₂ Nanocomposites with Enhanced Reversible Capacity and Cyclic Performance as Anodes for Lithium-Ion Batteries, *Electrochim Acta* 155 (2015) 288-296.
- (7) C.Y. Zhao, A. Kroll, H.L. Zhao, Q.Y. Zhang, Y. Li, Ultrasonic spray pyrolysis synthesis of Ag/TiO₂ nanocomposite photocatalysts for simultaneous H₂ production and CO₂ reduction, *Int J Hydrogen Energ* 37 (2012) 9967-9976.
- (8) C.Y. Zhao, L.J. Liu, Q.Y. Zhang, J. Wang, Y. Li, Photocatalytic conversion of CO₂ and H₂O to fuels by nanostructured Ce-TiO₂/SBA-15 composites, *Catal Sci Technol* 2 (2012) 2558-2568.